# SYNTHETIC BIOLOGY APPROACHES TO ENGINEER THERAPEUTIC IMMUNE CELLS FOR PRECISION MEDICINE

A Dissertation
by
NHUNG THI NGUYEN

Submitted to the Office of Graduate and Professional Studies of
Texas A&M University
in partial fulfillment of the requirements for the degree of

DOCTOR OF PHILOSOPHY

| | |
|---|---|
| Chair of Committee, | Yubin Zhou, |
| Committee Members, | David Reiner |
| | Margarita Martinez-Moczygemba |
| | Wenbo Li |
| Head of Department, | Carol Vargas |

December 2020

Major Subject: Medical Sciences

## ABSTRACT

Synthetic biology is an interdisciplinary field of science that involves the redesign and fabrication of biological components to synthesize a modified and advanced biological system to solve problems in medicine, agriculture, or bio-products. Expanding the repertoire of synthetic biology tools will enable us to remotely control gene expression and cellular behaviors in living organisms, which is useful for interrogating gene regulatory networks and controlling biological processes, as well as for engineering therapeutic immune cells for precision medicine. We describe herein the development of a set of optogenetic and chemogenetic devices, including a synthetic calcium ($Ca^{2+}$)-responsive transcriptional reprogramming device (CaRROT), a light-switchable chimeric antigen receptor (LiCAR), and designer receptors exclusively activated by designer drugs (DREADDs).

CaRROT is a chemical/light-inducible transcriptional reprogramming device composed of an optogenetically engineered, genetically-encoded $Ca^{2+}$ channel actuator and a calcium-responsive dCas9 fusion construct ($NFAT_{1-460}$-dCas9-VP64). In the presence of blue light or chemically-induced $Ca^{2+}$ depletion, CaRROT undergoes light-inducible nuclear translocation and turns on gene expression at endogenous genomic loci in the presence of small guide RNAs (sgRNAs). This reprogramming tool was created to avoid the off-target effects involved in the current platform of gene transcription reprogrammers made of CRISPR/Cas9 (dCas9) fused with repressive or activating effectors only.

In addition, our study includes a novel light-switchable chimeric antigen receptor (CAR) that can be remotely controlled through near infrared (NIR) light-converting

upconvension nanoplates for nano-optogenetic immunotherapy. LiCAR was designed by splitting the extracellular antigen-binding modules or the intracellular signal transduction modules from a conventional CAR. Each component was fused with one part of a pair of optical dimerizers, which undergo reversible light-dependent heterodimerization. Upon light stimulation, functional CARs will be reassembled to elicit T cell effector activity. LiCAR-expressing T-cells can selectively produce anti-tumor immune responses in the dual presence of tumor antigen and light in a spatiotemporally controlled manner, thus mitigating the side-effects and safety concerns associated with conventional CAR T-cells. Finally, the incorporation of DREADDs to T cells can either boost or suppress the strength and viability of engineered cells, thereby providing a chemogenetic tool for tunable activation or suppression of therapeutic immune cells. Together, we have created a toolbox that permits the precise control of the dose, location, and duration of immune responses to benefit future personalized immunomodulatory therapies.

## DEDICATION

This dissertation is dedicated to my parents, husband, brother, sister, nephews, and my little baby, who have been there for me always and constantly give me their compassion, affection and love.

To my mentor, Dr. Yubin Zhou, who has given me a great deal of time, enthusiastic support, continuous guidance and also care, protection and encouragement throughout my study.

To my committee members, Dr. Yubin Zhou, Dr. David Reiner, Dr. Margarita Martinez-Moczygemba, and Dr. Wenbo Li for their time, valuable suggestions, support and kindness.

To all of my wonderful lab mates and friends, who are willing to stand by my side when times get hard and have been a part of my Ph.D. journey and my life.

## ACKNOWLEDGEMENTS

PhD research is an arduous journey that requires not only self-motivation and efforts but also external support. In this regard, I would like to express my deepest appreciation to my advisor, Dr. Yubin Zhou, whose guidance, mentorship and source of motivation have shaped me as a mature scientist. He has walked me through the process of being an independent researcher from reading and reviewing articles with critical thinking to preparing research papers and conference presentations, networking with scientists, and applying for patents and awards. I am always thankful for his faith in my capacity and for choosing me as a graduate student in the lab even when the funding situation was low at the time.

I would also like to extend my great gratitude to my graduate advisor committee members: Dr. Yubin Zhou, Dr. David Reiner, Dr. Margarita Martinez-Moczygemba, and Dr. Wenbo Li, as well as Dr. Yun Huang and Dr. Gang Han (UMASS) for their helpful suggestions on my experiment designs, on how to shape the research work into a cohesive story, and on improving my writing and speaking skills to help me acquire competencies for professional growth.

I am also grateful to my friends and labmates – Dr. Jing Ji, Dr. Lian He, Dr. Goulin Ma, Dr. Kai Huang, Dr. Hongxiang Zeng, Dr. Rui Wang, Dr. Jiansheng Xie, Mr. Rui Chen, Mr. Yi Tsang Lee, Dr. Tianlu Wang, Dr. Tien Hung Lan, Mr. Shaohai Fang, and Dr. Tam Duong for their stimulating discussions, their co-authorships, and foremost, their wonderful friendships during the past 5 years.

I also acknowledge with a deep sense of gratitude to Dr. Clifford Stephan, Dr. Leoncio A Vergara, Dr. Sevinj Isgandarova, Ms. Nghi Nguyen, Ms. Mary Sobieski, Dr.

Reid Power, Mr. Yong Park, Ms. Goeun Bae, and Dr. Can Li for their technical support, data analysis help and consulting as well as gifts of essential reagents.

I would like to thank Dr. Stefan Siwko for his comments and efforts in proofreading and editing this study.

I am extremely thankful to all of the faculty, staff, and colleagues at the Texas A&M University Institute of Biosciences and Technology. Especially, I am grateful to Ms. Cynthia Lewis for helping with all the administrative issues and paperwork beginning from the date I applied to the IBT Graduate Study Program. I would also like to thank Ms. Denelle Orellana for helping manage all the matters related to my Ph.D. training. Special thanks to Dr. Peter J.A. Davies for encouraging me from the first day at the IBT.

Finally, it is my privilege to thank my husband, Dr. Tuan P.M. Ho, my parents, brother, sister, and nephews for their unconditional love and constant encouragement in all of my pursuits and for inspiring me to follow my goals.

## NOMENCLATURE

| | |
|---|---|
| AP-1 | Activator protein-1 |
| C21 | DREADD agonist 21/ Compound 21 |
| $Ca^{2+}$ | Calcium |
| CAD | CRAC activation domain |
| cAMP | Cyclic adenosine monophosphate |
| CC1 | Coiled-coil 1 |
| CD | cluster of differentiation |
| CIBN | Cryptochrome-interacting basic-helix-loop-helix protein |
| CNO | Clozapine-N-oxide |
| cpEGFP | Circular permutated green fluorescent protein |
| CRAC | Calcium release-activated calcium channel |
| CRY2 | Cryptochrome 2 |
| CT | C-terminus |
| CTLA-4 | cytotoxic T-lymphocyte-associated protein 4 |
| dCas9 | Catalytically deactivated CRISPR associated protein 9 |
| DMEM | Dulbecco's Modified Eagle's Medium |
| DNA | Deoxyribonucleic Acid |
| DREADD | Designer receptors exclusively activated by designer drugs |
| ER | Endoplasmic reticulum |
| FBS | Fetal Bovine Serum |
| FMN | Flavin mononucleotide |
| GAD | Grb2-related adapter protein |
| GPCR | G-protein coupled receptors |
| HEK | Human embryonic kidney |
| HEPES | N-2-hydroxyethylpiperazine-N-2-ethane sulfonic acid |
| HRP | Horseradish peroxidase |
| ICAM-1 | Intercellular Adhesion Molecule 1 |
| IFN-γ | Interferon-γ |

| | |
|---|---|
| IKK | IκB kinase |
| IL-2 | Interleukin 2 |
| iLID | Improved light-induced dimer |
| IP3 | Inositol trisphosphate |
| IP3R | Inositol trisphosphate receptor |
| IRES | Internal ribosome entry site |
| ITAM | Immunoreceptor tyrosine-based activation motifs |
| IκB | Inhibitor of NFκB |
| KD | Kinase domain |
| LAT | Linker For Activation Of T Cells |
| LFA-1 | Lymphocyte function-associated antigen 1 |
| LiCAR | Light-switchable chimeric antigen receptor |
| LOV | Light, oxygen and voltage |
| Luc | Luciferase |
| MAPK | Mitogen-activated protein kinase |
| mCh | mCherry |
| mEPAC1 | Mouse exchange protein activated by cAMP |
| NES | Nuclear export signal |
| NFAT | Nuclear factor of activated T-cells |
| NIR | Near-infrared |
| NIR | Near infrared |
| NLS | Nuclear localization signal |
| OLP | Olanzapine |
| ORAI1 | Calcium release-activated calcium channel protein 1 |
| PAS | Per-ARNT-Sim |
| PBS | Phosphate-buffered saline |
| PD-1 | Programmed cell death protein 1 |
| PI(3,4,5)P3 | Phosphatidylinositol (3,4,5)-trisphosphate |
| PI(4,5)P2 | Phosphatidylinositol 4,5-bisphosphate |

| | |
|---|---|
| PI3K | Phosphoinositide 3-kinase |
| PKC | Protein kinase C |
| PLP | Perlapine |
| PM | Plasma membrane |
| PS | Proline/Serine-rich domain |
| RNA | Ribonucleic acid |
| RTKs | Receptor tyrosine kinases |
| scFv | Single chain variable fragment |
| SDS-PAGE | SDS-polyacrylamide gels |
| SOAR | STIM-ORAI activation region |
| SOCE | Store-operated Ca2+ entry |
| SP | Signal peptide |
| sspB | Stringent starvation protein B |
| ssrA | Small stable RNA A |
| STIM1 | Stromal interaction molecule 1 |
| TG | Thapsigargin |
| TM | Transmembrane domain |
| UCNP | Upconversion nanoparticles |
| UCNPs | Upconversion nanoplates |
| WT | Wild type |
| Zap70 | Zeta-associated protein 70 kDa |
| Zdk | Zdark |

## CONTRIBUTORS AND FUNDING SOURCES

### Contributors

This work was supervised by a dissertation committee including Professor Yubin Zhou (advisor), Professor David Reiner, and Professor Margarita Martinez-Moczygemba of the Institute of Bioscience and Technology, Texas A&M University and Professor Wenbo Li of McGovern Medical School, The University of Texas Health Science Center at Houston.

### Funding Sources

All work for Chapter II of the dissertation was completed by Nhung Thi Nguyen, in collaboration with Dr. Lian He. All the work for Chapter III of the dissertation was completed by Nhung Thi Nguyen, in collaboration with Dr. Kai Huang. All the work for Chapter IV of the dissertation was completed independently by Nhung Thi Nguyen. This work was supported by grants from the National Institutes of Health (R01GM112003, R01HL134780, R21GM126532, and R01CA232017), the Cancer Prevention and Research Institute of Texas (RP170660 and RR140053), the John S. Dunn Foundation Collaborative Research Award, the Welch Foundation (BE-1913-20190330), and the American Cancer Society (RSG-16-215-01-TBE and and RSG-18-043-01-LIB).

Page

## TABLE OF CONTENTS

## LIST OF FIGURES

## LIST OF TABLES

Page

# CHAPTER I
# INTRODUCTION AND LITERATURE REVIEW

According to Dr. Jim Collins (MIT), “synthetic biology brings together engineering and molecular biology to model, design, and build synthetic gene circuits and other biomolecular components and uses them to rewire and reprogram organisms for a variety of purposes.” In our studies, we aim to build a diversity of advanced artificial optogenetic and chemogenetic tools, which can be used to control the expression of endogenous genes and modulate the activity of immune cells. The first tool is a synthetic $Ca^{2+}$-responsive transcriptional reprogramming device (CaRROT), which is composed of an NFAT regulatory domain (residues 1-460) fused with dCas9, and a transcription effector domain, $VP64$[4]. Nuclear dCas9 is targeted to specific genes by sgRNA to turn on reporter or endogenous gene expression. By taking advantage of naturally-existing photoreceptors derived from microbes, plants or mammals, we rewired $Ca^{2+}$ signaling via optogenetic engineering to achieve tailored functions with CaRROT. These tailored functions can be tightly controlled by chemicals or light to induce gene transcription with high precision. The second device is a light-switchable chimeric antigen receptor (LiCAR). We developed LiCAR T-cells by splitting a conventional CAR at different positions and installing photo-responsive modules into each half of a split CAR. The engineered T cell activation only occurs after functional assembly of two components of the split CAR in the presence of blue light illumination, thus conferring strict on-off spatiotemporal control over the anti-tumor ($CD19^{+}$ leukemia) immune response. Last but not least, we utilized the chemogenetic system Designer

Receptors Exclusively Activated by Designer Drugs (DREADDs) to fine-tune T cell activity with chemicals and FDA approved drugs.

$Ca^{2+}$ participates in various aspects of cellular activity and act as a second messenger in an array of cell types, particularly lymphocytes. In these mammalian cells, the intracellular $Ca^{2+}$ concentration is tightly regulated through coordinated actions of a repertoire of $Ca^{2+}$-signaling components, including G-protein coupled receptors (GPCRs), receptor tyrosine kinases (RTKs), various $Ca^{2+}$ channels and transporters/exchangers, and intracellular $Ca^{2+}$ sensing and buffering proteins[5-7]. Upon engagement of membrane receptors by ligands or antigens, phospholipase C gamma (PLCγ) is phosphorylated and activated to catalyze the hydrolysis of phosphatidylinositol 4,5-biphosphate ($PI(4,5)P_2$), yielding two important secondary messengers, diacylglycerol (DAG) and inositol 1,4,5-triphosphate ($IP_3$). $IP_3$ further binds to ER-resident $IP_3$ receptors to induce $Ca^{2+}$ release from the ER $Ca^{2+}$ store, known as store depletion, followed by the activation of store-operated $Ca^{2+}$ entry (SOCE)[6] (**Fig. 1a**). SOCE is best exemplified by the prototypical $Ca^{2+}$ release-activated $Ca^{2+}$ (CRAC) channel composed of ORAI1 and the stromal interaction molecule 1 (STIM1), and constitutes the primary route of $Ca^{2+}$ entry in non-excitable tissues[8-10]. During SOCE activation, STIM1 dynamically couples to ORAI1 via two major molecular steps (**Fig. 1b**): (i) the initiation of STIM1 activation via $Ca^{2+}$ depletion-induced oligomerization of the luminal domain containing the EF-SAM domain; (ii) inside-out signal propagation toward the STIM1 cytoplasmic domain (STIM1ct) to overcome an intramolecular inhibition primarily mediated by the interaction between the coiled-coil 1 region (CC1) and the STIM-Orai activating domain (SOAR)[6,9,10, 11]. In our study, we utilized

**a** **b**

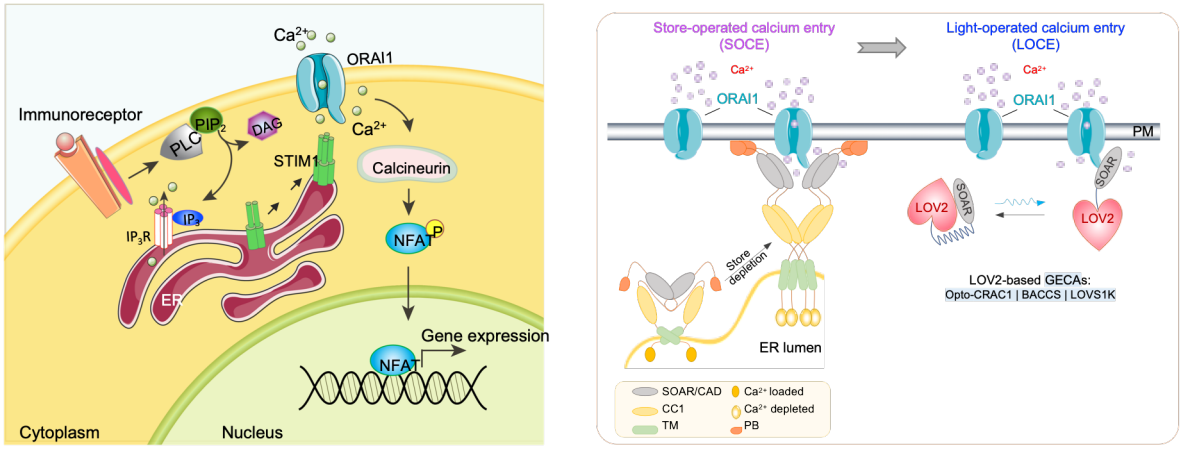


**Figure 1. ORAI-STIM signaling in lymphocytes[2,3].**
(**a**) Scheme of SOCE mediated by the ORAI1–STIM1 pathway in lymphocytes*. Upon engagement of immunoreceptors, the production of $IP_3$ leads to the activation of $IP_3R$ and release of $Ca^{2+}$ from internal stores. The decrease of ER $Ca^{2+}$ concentration is subsequently sensed by the EF-hand-containing ER $Ca^{2+}$ sensor STIM1, which in turn activates ORAI1 CRAC channels through its interaction with the pore-forming subunit ORAI1, followed by a second phase of intracellular $Ca^{2+}$ elevation and further activation of downstream effectors, including calcineurin, NFAT, and NFAT-dependent gene expression. (**b**) Genetically-encoded $Ca^{2+}$ channel actuators (GECAs) derived from STIM1**. (*Left*) schematic illustrating functional STIM1-ORAI1 coupling in response to store depletion. $Ca^{2+}$ depletion within the ER lumen induces oligomerization of the luminal EF-SAM domain to initiate STIM1 activation and triggers a conformational switch to expose SOAR/CAD and the C terminal PB domain. Next, STIM1 undergoes further oligomerization and migration toward the PM, a process facilitated by the association between SOAR/CAD and ORAI1, as well as the interaction between the positively-charged PB domain and negatively-charged phosphoinositides embedded in the PM. SOAR/CAD is responsible for direct engagement and activation of ORAI channels to mediate $Ca^{2+}$ influx. (*right*) The design of GECAs based on a LOV2 conformational switch (Opto-CRAC1, LOVS1K or BACCS), in which the CC1-SOAR interaction-mediated intramolecular autoinhibition is mimicked by LOV2-SOAR fusion in the dark. Upon photostimulation, LOV2 undergoes conformational changes to expose SOAR/CAD, which engages ORAI $Ca^{2+}$ channels to induce $Ca^{2+}$ influx.
*Reprinted from “Store-Operated ORAI Calcium Channel” by Nhung Thi Nguyen and Yubin Zhou. Elsevier. 2020, Encyclopedia of Biological Chemistry 3rd Edition.
**Reprinted from “Optogenetic approaches to control Ca2+-modulated physiological processes” by Nhung T. Nguyen, Goulin Ma, Yubin Zhou, and Ji Jing. Current Opinion in Physiology. 2020.

genetically-encoded $Ca^{2+}$ channel actuators (GECAs) engineered from the CRAC

channel to induce $Ca^{2+}$ influx (designated as Opto-CRAC). In this opto-CRAC design, a

genetically-encoded photoswitch, the light-oxygen-voltage domain 2 (LOV2) from *Avena sativa*[12,13] phototropin 1, is installed into STIM1 to mimic the STIM1 conformational switch, a critical step in CRAC channel activation (**Fig. 1b**). Specifically, the coiled coil 1 (CC1) domain of STIM1 was replaced by LOV2 and various STIM1ct fragments were optimized to generate LOV2-STIM1ct chimeras (Opto-CRAC[14,15], BACCS[16], and LOVS1K[17]). These LOV2-based GECAs enable more rapid and readily reversible control of $Ca^{2+}$ signals, with activation kinetics ranging from 10 sec to 30 sec and deactivation half-lives in the range of 30-50 sec.

The AsLOV2 module consists of a flavin mononucleotide (FMN)-binding core domain known as a Period-ARNT-Single (PAS core) motif [18] and a C-terminal Jα helix. In the dark, the Jα helix tightly docks to the PAS scaffold, thereby imposing steric hindrance to mask the active site or binding interface(s) of the STIM1ct fragment. Upon blue light illumination, photoexcitation creates a covalent adduct between LOV2 residue C450 and the cofactor FMN, allowing the Jα helix to undock, with subsequent exposure of SOAR/CAD, which then moves toward the plasma membrane to directly engage and activate ORAI1 $Ca^{2+}$ channels. This construct can rapidly translocate between the cytosol and the PM to reversibly induce $Ca^{2+}$ influx following repeated dark-light cycles. In T cells, $Ca^{2+}$ influx induced by CRAC activates downstream effectors such as calcineurin, a $Ca^{2+}$/calmodulin-dependent phosphatase, which dephosphorylates nuclear factor of activated T cells (NFAT) and subsequently leads to NFAT nuclear translocation[19] (**Fig. 1a**). In the CaRROT system, only an N terminal NFAT regulatory domain (residues 1−460) without the DNA binding domain was used to avoid binding to endogenous NFAT targets.

The mechanism of T cell activation via the T cell receptor and conventional CAR design guided our efforts to develop a LiCAR tool to mimic T cell activity. Naive T cell activation by antigen presenting cells (APCs) requires two signals[20]. Signal-1 is initialized by the interaction of the TCR with a peptide-MHC complex presented on the surface of an APC[21,22], while signal-2 comes from the interaction of costimulatory molecules at the interface between APCs and T cells such as B7-1 (CD80)/CD28, B7-2 (CD86)/CD28, LFA-1/ICAM-1 or ICAM2, ICOSL/ICOS, 4-1BBL/4-1BB, OX40L/OX40, CD2/LFA-3 (positive signal)[23,24] or CD80/CTLA-4, CD86/CTLA-4 (negative signal)[24] (**Fig. 2)**. The interaction of TCRs with peptide–MHC complexes is facilitated by co-receptors CD4 and CD8, which are closely adjacent to the membrane domains of MHC class II and class I molecules, respectively. CD4 and CD8 intracellular domain associates with the Src family kinase Lck, which then phosphorylates the immunoreceptor tyrosine-based activation motifs (ITAMs) in the CD3 δ-, γ-, ε- and ζ-chains. Phosphorylated CD3 becomes a docking site to recruit the Syk family kinase Zeta-associated protein 70 kDa (Zap70). Zap70 then phosphorylates other targets such as Linker For Activation Of T Cells (LAT), which then recruits Grb2-related adapter protein (GAD) and its binding partner SLP-76. SLP-76 has a PRR domain that binds phospholipase C (PLCγ1)[25], which subsequently hydrolyzes the membrane-bound phospholipid phosphatidyl inositiol 4,5 bisphosphate to generates both IP3 and DAG. IP3 triggers efflux of $Ca^{2+}$ from ER as mentioned above, while DAG results in the activation of two major pathways including Ras and PKCθ. Ras is a guanine nucleotide-binding protein, which ultimately leads to the activation of mitogen-activated protein kinase (MAPK) pathways consisting of Raf–MEK–ERK. This pathway is involved in the

early expression c-Fos, a component of the activator protein-1 (AP-1) transcription complex composed of c-Jun/c-Fos, as well as in the upregulation of CD69, an early marker of T cells[25,26]. Upon induction of AP-1, endogenous NFAT and AP1 cooperatively bind to adjacent sites on composite DNA elements and synergistically regulate key genes essential for lymphocyte activation (e.g., IL-2 and IFN-γ)[27]. Another important signaling pathway regulated by DAG involves PKCθ, which modulates NFκB activation. PKCθ belongs to the family of serine/threonine protein kinases, which promotes phosphorylation of Inhibitor of NFκB (IκB) via the IκB kinase (IKK) complex, leading to IκB's ubiquitination and degradation. IκB degradation frees NFκB for translocation into the nucleus and turn on gene transcription[25,28]. Interestingly, if T cells only receive signal through TCR (signal-1), it undergoes anergy or exhaustion, in which T cells become non- responsive to stimuli as well as replication incompetent or clone deleted. Costimulatory receptors such as CD28 provide additional signals necessary for anergy prevention, productive T cell activation[29], as well as for controlling the immune response and stabilizing the internal environment[24]. CD28 binds and activates different pathways including PI3K, Ras and PKCθ[29]. In general, both signal 1 and signal 2 leads to full T cell activation mediated by the nuclear translocation and activation of three transcription factors (TFs) including NFAT, AP-1, and NF-κB. The combination of these three TFs promotes the expression of cell surface receptors, cytokines, or chemokines required for T cell activation, proliferation, and differentiation. In the case of missing co-stimulatory molecules, NFAT is activated in the absence of AP-1, which will trigger the expression of diacylglycerol kinase-α (*DGKA*), the E3

ubiquitin-protein ligase *CBLB,* and *GRAIL,* all of which are related to anergy in lymphocytes and inhibit full T cell activation[1].

Chimeric antigen receptors (CARs) (*a.k.a*., chimeric immunoreceptors, chimeric T cell receptors or artificial T cell receptors) are synthetic receptors engineered onto the surface of T cells, where they can engage specific tumor antigens in a major

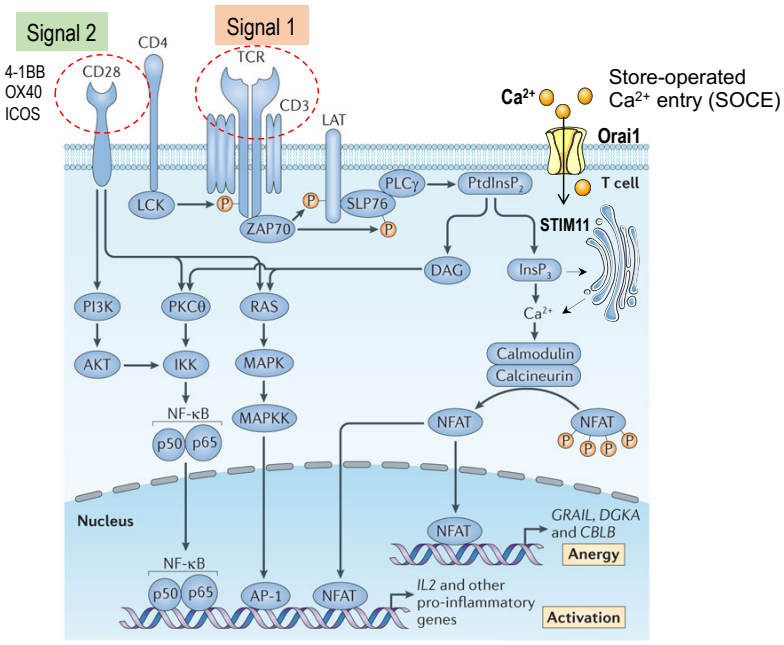


**Figure 2. T cell receptor-dependent signaling pathways[1]**

histocompatibility complex (MHC)-independent manner[30]. Antigen recognition allows these engineered T cells to be activated and subsequently perform their killing/effector activities toward tumor cells. A typical FDA-approved second-generation CAR contains an antibody-derived single chain variable fragment (scFv) in the extracellular domain, a transmembrane domain, costimulatory signals (*e.g*., 4-1BB or CD28), and the intracellular signal transduction component known as the immunoreceptor tyrosine-based activation motif (ITAM) derived from CD3ζ. CAR T-cell therapy has demonstrated

a curative potential for elimination of tumors with complete response rates of 69%–90% in pediatric patients who have relapsed or refractory acute lymphoblastic leukemia (ALL) in a phase 1 trial[31]. The T-cells used in this approach are typically collected from a patient or a donor and are then engineered in the laboratory to express tumor-specific recombinant receptors composed of key signaling modules from both the T cell receptor (TCR) and co-stimulatory receptors. The membrane receptor of these CAR T-cells can be precisely targeted to a surface antigen on the cancer cells due to its antigen-specific scFv. Following reintroduction into patients, the CAR-T cells can recognize their cognate target antigen and become activated to attack cancer cells.

CAR design has evolved to the fourth generation thus far with a considerable increase in sophistication. The original first-generation CAR design consisted of two bound modules: an extracellular recognition moiety, which usually comes in the form of an antibody-derived single chain variable fragment (scFv), antigen-binding fragments (Fabs), or naturally occurring ligand binding domains, and a lymphocyte intracellular stimulating domain including either a CD3z chain or a FcR$\gamma$ activation chain[32,33]. In an attempt to mimic full physiological T cell activation by co-stimulation signals provided by the interaction of T cells with antigen presenting cells (APCs), second generation CARs were developed by fusing scFv with one costimulatory domain, e.g., 4-1BB, OX40, or CD28, while the third generation adds two or more costimulatory domains[34-36]. This modification has tremendously enhanced the expression of downstream cytokines, tumor rejection and avoiding T cells anergy. The fourth generation - so called TRUCK - is derived from the second one with the addition of an expression cassette for a

cytokine such as IL-12 to facilitate T cell activation as well as to recruit innate immune cells to eliminate cancer cells that are not recognized by CAR T cells[37].

In a general procedure, T cells collected from a patient or donor are genetically engineered by introducing specific anti-tumor CAR DNA (e.g. CD19 antigen, in this application) into them. CAR T-cells are then infused back to the patient's bloodstream, where they recognize their cognate target antigen on cancer cells, and become activated to attack cancer cells expressing the targeted antigen on their surface. However, CAR still has a substantial lack of control that causes it to have significant off-target effects. CAR T-cell therapy commonly causes cytokine release syndrome due to the rapid activation of T cells after interaction with antigens[38,39] and it has been linked to neurologic toxicity as well[39,40]. CAR designs also lack the ability to discriminate between normal $CD19^+$ cells and cancerous $CD19^+$ cells, which often leads to B cell aplasia[41]. These side-effects have devastating consequences for certain patients in clinical trials and pose significant limitations on the current use of CAR T therapy.

Several studies have been conducted to mitigate these side effects and safety concerns. One strategy is to use suicide switches called iCasp9[42] that can be triggered to eliminate T cells when they present overly toxic effects. Briefly, the caspase 9 gene, a pro-apoptotic molecule, is split and fused with a drug-binding domain derived from the human FK506-binding protein. When a chemical inducer of dimerization (CID) drug, AP1903, is added, caspase9 dimerizes and activates the downstream executioner caspase 3 molecule, resulting in cellular apoptosis. A second strategy for removing overactive CAR T cells is the expression of a tag that can induce antibody-dependent cellular cytotoxicity (ADCC). The tag is a truncated human EGFR polypeptide

(huEGFRt), which lacks extracellular N terminal ligand binding domains and the intracellular receptor tyrosine kinase but retains the transmembrane domain and a binding epitope (domains III, IV) for an anti-EGFR monoclonal antibody, cetuximab (Erbitux)[43]. The binding of antibody induces ADCC mainly via natural killer (NK) effector cells. Another approach to avoid the off-target issue is to design inhibitor chimeric antigen receptors (iCARs)[44]. iCAR is comprised of a scFv domain that recognizes the antigen presented in a normal cell but not in cancer cells and the cytosolic immunoreceptor tyrosine-based inhibitory motif (ITIM) of PD-1 or CTLA-4, which mitigates the immune responses. Upon iCAR binding to a specific antigen expressed only by normal tissues (e.g., human prostate specific membrane antigen-PSMA in the study of Fedorov et al., 2014[44]), it switches off the response of CAR T cells. In this way, iCAR T-cells can discriminate cancer cells from healthy ones, and reversibly block transduced T cell activities in an antigen-dependent manner. This strategy seems promising; however, it requires the identification of human antigens that are present on the surface of most healthy tissues but not on the tumor cells.

A different strategy based on the targeting of two antigens at the same time, which can be employed to reduce off-target side effects, is the tandem CAR. One scFv is fused with CD3z, and another is with a costimulatory domain (i.e., 4-1BB or CD28)[45]. The recognition of both antigens on tumor cells allows a superior activation of the dual CAR T-cells. Healthy cells, which engage only one of the scFvs, will induce low or no response due to the absence of costimulatory signals or a signal transduction domain. Therefore, tandem CARs provide a safer path that restricts CAR-T cell activity to cancer cells co-expressing two antigens rather than just one.

The great advantage of our LiCAR strategy is that it requires two inputs, light and antigen, in order to activate T cells. One of these factors alone should not trigger a productive T cell response. This strategy also allows titration of the therapeutic activity of CAR T-cells by varying the length and intensity of photostimulation. Furthermore, the control over T cells is reversibly by switching on and off the light source, which promises

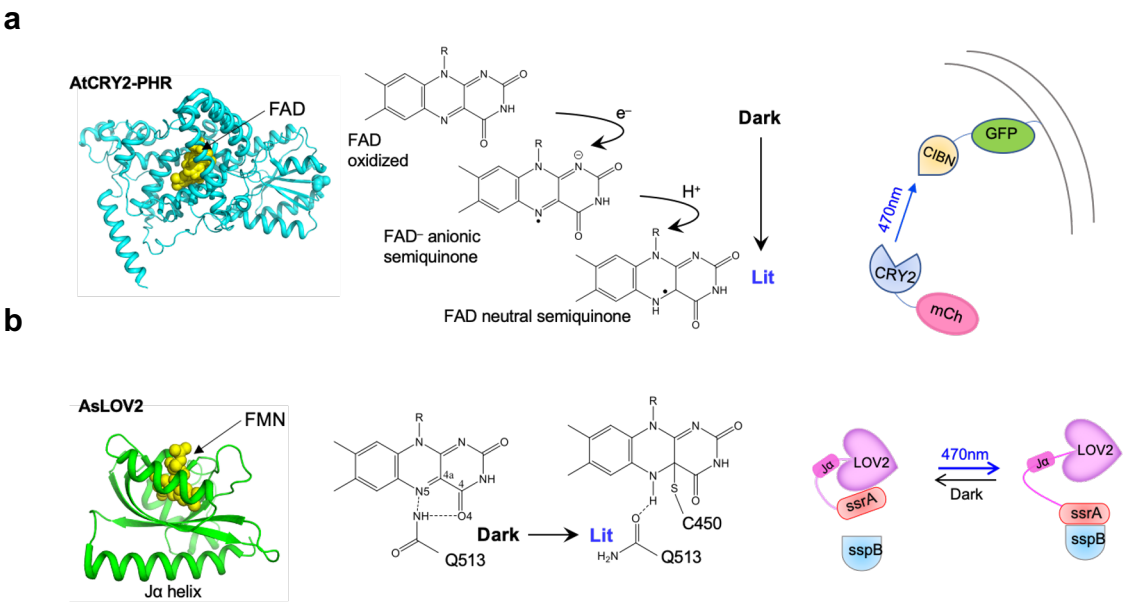


**Figure 3: Optical dimerizers for light-inducible assembly of CARs.**
The 3D structure and simplified photocycle reactions of AtCRY2-PHR (modeled from CRY2, PDB entry: 1U3D, (**a**)) and AsLOV2 (PDB entry: 2V0W, (**b**)). CRY2 binds to its photo-sensitive binding partner CIBN, while LOV2-ssrA binds to sspB upon blue light illumination. FAD, flavin adenine dinucleotide; FMN: flavin mononucleotide; ssrA, small stable RNA; sspB, tringent starvation protein B.

to prevent T cell overactivation or unexpected cross-reaction with healthy normal cells. Our optogenetic LiCAR system would lead to a new generation of cancer immunotherapy, in which the precise control over anti-tumor immunity enables the real-time tuning of treatment amplitude and duration, therefore mitigating the toxicity encountered in the current therapeutic modalities.

In order to engineer LiCAR, we need to use different photosensitive modules, which can be exploited for optogenetic design. The recent discovery of photoinducible protein-protein interactions *(e.g., LOV2-ssrA*- SspB, CRY2-CIBN1) has paved the way for the development of LiCAR (**Fig. 3**). These proteins are native to plants and animals; therefore, the light-switchable operation can be achieved in mammalian cells with minimal toxicity. CRY2 and LOV2 are operated by using widely accessible flavin chromophores from cells and thus obviating the need to supply exogenous cofactors. iLID stands for improved light-induced dimer, which consists of a bacterial SsrA peptide fused to the C-terminus of AsLOV2 and sspB. In the dark, the SsrA peptide is caged by LOV2, therefore, it is unable to bind to its natural binding partner, sspB. Exposure to blue light allows the undocking of SsrA to restore its interaction with sspB[46]. Another optical dimerizer consists of the N-terminal photolyase homology region (PHR) from blue light-absorbing photosensor cryptochrome 2 (CRY2) and a truncated version of CIB1 (residues 1-170), a basic helix-loop-helix (bHLH) protein from *Arabidopsis*[47]*.* While the dissociation kinetics of iLID-SspB to its dark state following photoactivation is quite fast ($T_{½}$ = ~20 s)[38], the reversion of CRY2-CIBN1 is slower with a half-life of about 5 minutes[47]. Two systems, therefore, provide diverse options for level of activation as desired, either for a prolonged T cell response or for transient stimulation.

Aside from CaRROT and LiCAR that are responsive to light stimulation, we also incorporate DREADDs, chemogenetic tools that have been widely used in neuroscience, into lymphocytes to modulate cell fate by either boosting T cell activation or suppressing immune response. DREADDs are evolved from G-protein-coupled receptors (GPCRs), which are recognized as the largest protein superfamily of cell-

surface molecules participating in signal transmission[48,49]. There are about 720–800 GPCRs in the human genome, which are classified based on their tissue distribution, subcellular expression profiles, and their coupling with different G protein families[50]. GPCRs consist of an extracellular N-terminal domain, seven transmembrane α-helices embedded in the plasma membrane with interspersed portions that loop in and out of the cell, and a C-terminal tail often involved in regulating GPCR activity. In the resting state, GPCRs interact with a GDP-bound G protein heterotrimer, which contains α, β and γ subunits anchored in the plasma membrane (PM). Subunits α and γ connect to the PM by lipid anchors and the α subunit binds to GTP (active state) or GDP (inactive state) depending on the activity of the protein. When an external stimulus (e.g. odorant, photons, hormone, peptides, proteins, neurotransmitter or small molecule) engages its cognate GPCR, it triggers conformational changes to activate the G protein, catalyzing the dissociation of GDP from the α subunit which is immediately replaced by GTP. This leads to a structural change in Gα and the release of $G_{\alpha}$ from the Gβγ subunits. Separated $G_{\alpha}$ and Gβγ disperse, relaying the signal to downstream effectors[51]. There are four major α subunit subfamilies including $G\alpha_s$, $G\alpha_i$, $G\alpha_q$ and $G\alpha_{12/13}$, and specific GPCRs can engage one or several Gα subfamilies[48]. Gα proteins are able to activate different downstream target proteins. In particular, $G\alpha_s$ stimulates adenylyl cyclase which catalyzes adenosine triphosphate (ATP) conversion into cyclic adenosine monophosphate (cAMP), thus increasing the levels of intracellular cAMP. $G\alpha_i$, by contrast, is an inhibitor of adenylyl cyclase. $G\alpha_q$ family proteins bind to and activate phospholipase C (PLC), which hydrolyzes phosphatidylinositol 4,5-bisphosphate [PtdIns(4,5)$P_2$] into diacylglycerol (DAG) and inositol trisphosphate ($IP_3$)[52] and causes

calcium efflux from the ER calcium store. Finally, $G\alpha_{12}$ plays a crucial role in the activation of Rho GTPase nucleotide exchange factors (RhoGEFs), which catalyze the exchange of GDP for GTP by inducing an active conformation of the small monomeric GTPase RhoA. The Gβ subunits and Gγ subunits function as a dimer to modulate the activity of phospholipases, ion channels and lipid kinases.

As many GPCRs share common structures and are extremely diverse, ligands acting on one GPCR may also have “off-target” effects on other molecular targets[53]. Therefore, it would be beneficial to engineer selected GPCRs to be exclusively activated by a specific ligand without affecting other molecular targets. As such, the engineered GPCRs can be placed in different cellular contexts to understand the function of a particular GPCR signal cascade in various physiological processes[54]. Receptors activated solely by synthetic ligands (RASSLs) or designer receptors exclusively activated by designer drugs (DREADDs) were generated based on this idea. In general, these chemogenetic tools represents a strategy for engineering proteins to become unresponsive to their endogenous ligands but activated by a different molecule. In our study, DREADDs were engineered into T cells to regulate immune response.

# CHAPTER II
# REWIRING CACIUM SIGNALING FOR PRECISE TRANSCRIPTIONAL REPROGRAMMING*

## Introduction

Diverse cellular activities such as cell growth, cell differentiation, metabolism, and homeostasis are dictated by complex gene networks and active transcription regulation[55,56]. To illuminate gene functions during these biological processes, interventional tools that enable real-time manipulation and perturbation of target gene expression are critically needed. The clustered regularly interspaced short palindromic repeats (CRISPR)-associated-9 nuclease also known as Cas9 derived from *Streptococcus pyogenes* has emerged recently as a powerful tool for genome engineering[57-61]. Cas9 can be guided by a single RNA (sgRNA) to a genomic target site complementary to the sgRNA and juxtaposed to a protospacer adjacent motif (PAM) sequence: NGG[62]. The CRISPR-Cas9 genome editing system only requires two major molecules to bind to a target DNA sequence, and thus has great potential to become an RNA-dependent DNA recognition platform. Recently, engineered catalytically inactive Cas9 (or dCas9) has been developed as a robust tool for targeted endogenous gene regulation without genetically altering the DNA sequence[57,63-68]. The dCas9-sgRNA complex can induce repression of endogenous genes in bacteria by blocking RNA polymerase or perturbing transcription factor binding[55,64,69]. Also, dCas9 fused to effector

*Part of this chapter is reprinted with permission from "Rewiring Calcium Signaling for Precise Transcriptional Reprogramming" by Nhung Thi Nguyen[#], Lian He[#], Margarita Martinez-Moczygemba, Yun Huang and Yubin Zhou. ACS Synth Biol. 2018 Mar 16;7(3):814-821. [#] These authors contributed equally to this work.

domains such as multiple tandem copies of Herpes Simplex Viral Protein 16 (VP64) or p65 activator domain (p65AD) have been used to activate reporter genes or endogenous genes in both *E. coli* and human cells[55,57,70]. However, without temporal control, the application of these reprogramming tools will likely cause off-target effects and lack strict reversibility.

In order to overcome this limitation, we decided to generate synthetic chemical and light-sensitive dCas9 nuclear translocation systems. Our design combines genetically encoded photoactivatable $Ca^{2+}$ actuators with an engineered $Ca^{2+}$-responsive transcription factor fused to a dCas9-effector (**Fig. 4**). The most effective construct used a photo-switchable $Ca^{2+}$ actuator engineered from the CRAC channel (Opto-CRAC)[15,71-73] to remotely control calcium signals and $Ca^{2+}$-dependent nuclear translocation of engineered dCas9 fusion proteins. We improved the Opto-CRAC system to reduce the "leakiness" of $Ca^{2+}$ influx, or dark-state background activity. $Ca^{2+}$ influx induced by Opto-CRAC activates calcineurin, a $Ca^{2+}$-dependent phosphatase, which dephosphorylates nuclear factor of activated T cells (NFAT) and subsequently leads to NFAT nuclear translocation (**Fig. 1**)[74]. Hence, upon co-transfection with the Opto-CRAC system, an NFAT fragment (residues 1-460) fused with dCas9-VP64 was induced to translocate into the nucleus upon blue light illumination. Nuclear dCas9 was further directed toward its target genes by sgRNA to turn on a reporter or endogenous target gene expression. The calcium signals can be generated either with calcium channel agonists or light illumination. We demonstrate herein the use of this chemical- or light-inducible transcriptional reprogramming device (designated as CaRROT for "*calcium-responsive transcriptional reprogramming tool*") to modulate gene expression with high precision.

## Materials and Methods

### *Cloning and plasmid construction*

Opto-CRAC vectors were designed by amplifying *Homo sapiens* STIM1-CT fragments (residues 336–486, 336–442, 347–448) and *Danio rerio* STIM1(341-442) using the KOD Hot start DNA polymerase (EMD Millipore, Billerica, MA, USA). STIM1 sequences were inserted downstream of $LOV2_{404-546}$ between the HindIII-XhoI restriction sites to replace Rac1 in the pTriEX-mcherry-PA-Rac1 plasmid (Addgene, #22027). Linker 1 (GSGLEGSGG) or linker 2 (GSGLESG) was introduced into the Opto-CRAC vectors at NotI-XhoI sites. cDNAs encoding Zdk1 and Zdk2 were a gift from Dr. Klaus M Hahn at the University of North Carolina at Chapel Hill. They were amplified and inserted between XhoI-XbaI sites.

To construct dCas9-based nuclear translocation vectors, we sequentially introduced NFAT (1-460) and dCas9, VP64 (derived from Addgene plasmid 22027), and GFP or BFP, to the AflII/AgeI/HindIII and XhoI sites of pcDNA3.1(+). The NLS oligonucleotides were also inserted during amplification depending on the construct. AsLOV2-based bipartite NLS1 and NLS2 generated from biLINUS 9 and biLINUS 11, respectively, were gifts from Dr. Barbara Di Ventura at the University of Heidelberg, Germany. All the restriction enzymes used in our studies were purchased from New England Biolabs.

The sgRNA targeting EGFP reporter, MYOD1 sgRNA 1 and sgRNA2 were obtained from Addgene (#60719, #64137 and #64138). The sgRNAs targeting ASCL1 were generated by annealed oligo cloning using the BsmBI site of LentiCRISPRv2,

(Addgene: #52961). An EGFP reporter containing eight copies of a gRNA binding site for light-inducible dCas9 activation was obtained from Addgene (#60718).

***Cell culture and transfection***

HEK293T and HeLa cells from the American Type Culture Collection (ATCC) were maintained in DMEM medium (Gibco) supplemented with 10% FBS, 100 units/ml penicillin and 100 μg/ml Streptomycin (Gibco) at 37$^{o}$C in a humidified atmosphere under 5% CO2. For confocal imaging, 2x10$^{5}$ cultured cells were seeded on 35-mm glass-bottom dishes 24 hours before transfection using Lipofectamine 3000 (Life Technologies) according to the manufacturer's instructions.

***Fluorescence imaging and statistical analysis***

Confocal imaging was performed generally at 24 hours after transfection by using an inverted Nikon Eclipse Ti-E microscope customized with Nikon A1R+ confocal laser sources (405/488/561/640 nm). We used an external blue light (470 nm, tunable intensity of 0–50 $\mu W/mm^2$, ThorLabs Inc., Newton, NJ, USA) for photostimulation.

For measurements of $Ca^{2+}$ influx using the green color calcium indicator GCaMP6s or red indicator jRCaMP1b, we co-transfected 100 ng of each Opto-CRAC construct and 100 ng cytosolic GCaMP6s or jRCaMP1b plasmid into HeLa cells using Lipofectamine 3000. Twenty-four hours after transfection, a 488-nm laser was used to excite GFP, and a 561-nm laser to excite mCherry at intervals of 1–5 s. mCherry-positive cells were used for statistical analysis.

In order to evaluate the nuclear translocation of dCas9 variants, we transfected single dCas9-VP64-mCherry-AsLOV2-bipartite NLS version 1.0 or Version 2.0 into Hela cells or co-transfected Opto-CRAC with one of the following constructs: CaRROT-V3, V4, and V5, then incubated for one day. Photo-stimulation was used to induce $Ca^{2+}$ influx mediated by Opto-CRAC constructs, and the cells were time-lapse recorded for more than 30 minutes at intervals of 2 minutes. Nine mCherry-positive cells (the first two constructs) and both mCherry and BFP/GFP-positive cells (the last three constructs) were selected to calculate the ratio of fluorescence signal between nuclei and the total fluorescence (nuclei plus cytosolic intensities).

For the EGFP reporter assay, HeLa cells were seeded onto 4-well glass bottom dishes for confocal imaging and transfected with the different sets of vectors in each well: BFP-tagged CaRROT-V5, sgRNA, Opto-CRAC, and EGFP reporter at ratio 3:1:1:2. Twenty-four hours later, fluorescent images were acquired at 37$^{o}$C and 5% $CO_2$ at 40x or 60x magnification. Imaged fields were selected from three different areas in each well, and time-lapse recording was done for 12 hours at intervals of 5 minutes under blue light exposure (pulsed blue LED at 470 nm; power density of 0–50 $\mu W/mm^2$; 5 sec ON, 20 sec OFF) or following addition of TG (2 μM). At least nine BFP, GFP and mCherry-positive cells (the group used Opto-CRAC) or BFP and GFP-positive cells (without Opto-CRAC) were chosen for EGFP reporter expression analysis.

***Flow cytometry analysis***

Hela cells were seeded in two 6-well plates transfected with a combination of vectors in each well: BFP-tagged-CaRROT-V5 (750ng), sgRNA (250ng), EGFP reporter

(500ng), Opto-CRAC (250 ng). After 24 hours of transfection, one plate was kept in the dark, and to another plate TG (2 μM) was added, or the plate was subjected to blue light irradiation (470 nm, tunable intensity of 0–50 $\mu W/mm^2$) for 1 hour, subsequently followed by pulsed stimulation (5 seconds ON for every 20 seconds) for another 24 hours to maintain constant activation of the light-inducible system. Next, the cells were washed, trypsinized and washed with PBS twice. The levels of fluorescence protein were determined using a LSRII flow cytometer (BD Biosciences). Cells were sampled at a medium flow rate, and 10,000 cells were counted for each condition. FlowJo software (TreeStar) was used to analyze the data ($EGFP^+$ in $BFP^+$ or $BFP^+mch^+$ cell populations). The experiments were conducted in duplicate.

***Endogenous gene expression assay***

HEK293T cells were plated at approximately $5x10^4$ cells/well in 12-well plates (Corning Inc., USA) and cultured for 24 hours. Each well was transfected with 250ng, 250ng and 750 ng of the sgRNA expression plasmid, Opto-CRAC, and BFP-tagged-CaRROT-V5, respectively. As a positive control, plasmids encoding dCas9-NLS-VP64 and sgRNA were transfected at a 3:1 ratio. 24 hours after transfection, samples underwent blue light stimulation or incubation in the dark as described above. On the next day, mRNA was extracted using Qiagen RNeasy spin prep columns and reverse transcription PCR was performed using amfiRivert cDNA Synthesis Platinum Master Mix (genDEPOT). Relative levels of cDNA were detected using amfiSure qGreen Q-PCR Master Mix (genDEPOT) and Mastercycle Real-Time PCR (Eppendorf, USA). The data

were normalized to GAPDH levels and cells transfected with an empty plasmid (control) using the ΔΔCt method.

## Results

***Design of second generation Opto-CRAC and CaRROT constructs.***

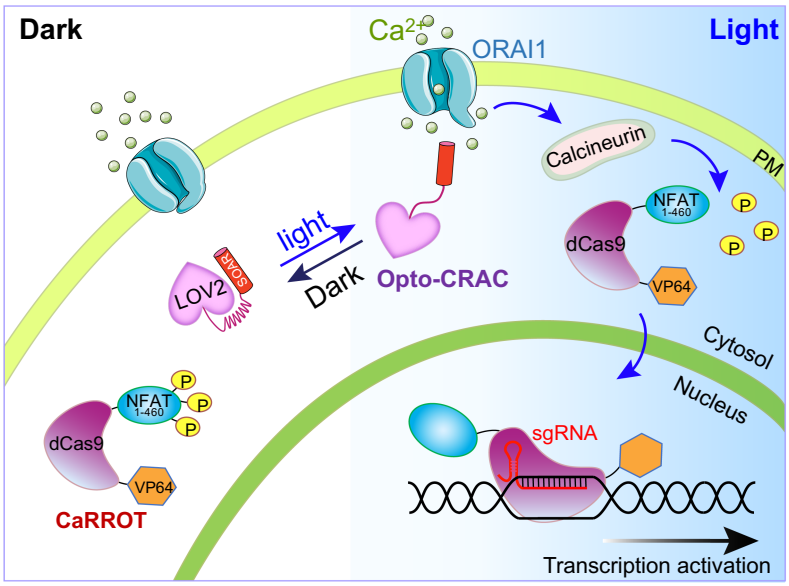


**Figure 4. Design of genetically encoded CaRROT to enable spatiotemporal control of transcriptional reprogramming in mammals.**
This synthetic device is composed of (i) second-generation Opto-CRAC made of LOV2-SOAR chimeras that could photoactivate ORAI calcium channels on the plasma membrane with tight control over $Ca^{2+}$ signals; and (ii) a calcium-responsive dCas9 fusion construct (e.g., NFAT1−460-dCas9-VP64). The N-terminal NFAT fragment used in the design lacks the C-terminal DNA binding domain to avoid binding to endogenous NFAT targets. In the dark, CaRROT stays in the cytosol. Upon blue light illumination, CaRROT undergoes light inducible nuclear translocation due to the cleavage of the phosphate groups (P) by calcineurin to turn on gene expression at targeted loci in the presence of small guide RNAs (sgRNAs). In addition to light, chemicals or ligands that could elicit intracellular calcium mobilization could likewise rewire calcium signaling to achieve inducible transcriptional reprogramming at targeted genomic loci.

In order to regulate specific gene expression, dCas9 is required to translocate into the nucleus and is directed by a sgRNA to the promoter of the targeted genes. In most

applications, the nuclear localization of dCas9 is enabled by adding several nuclear localization signals (NLS) at both the N and C-termini of dCas9[57,68]. Without the NLS signals, dCas9 generally resides in the cytoplasm given its relatively large size and lack of a strong intrinsic NLS (**Fig. 5a**). To enable light-controllable nuclear translocation to execute its function, we designed and constructed several photosensitive dCas9-Vp64 systems based on two strategies: i) fusion of dCas9-VP64 with a light-sensitive NLS; or ii) design of a synthetic $Ca^{2+}$-dependent nuclear translocation device, thereafter termed as calcium-responsive transcriptional reprogramming tool (or CaRROT) (**Fig. 6a**).

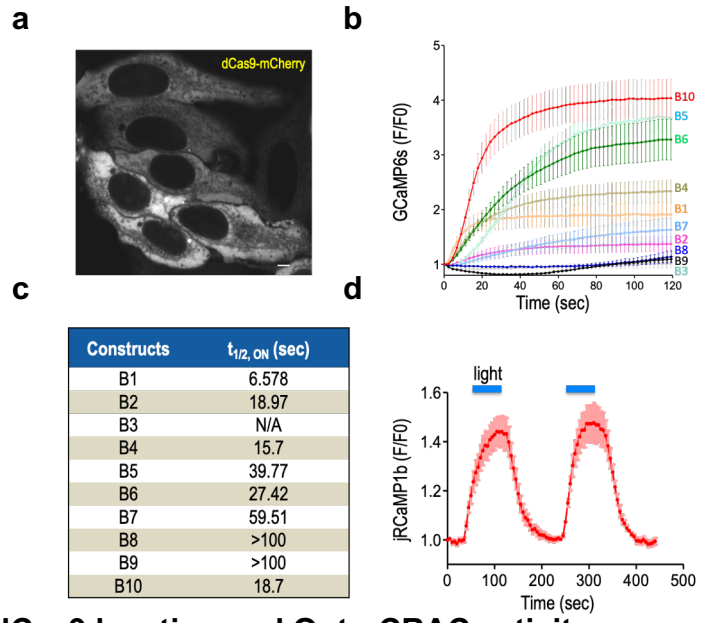


| Constructs | $t_{1/2, ON}$ (sec) |
|---|---|
| B1 | 6.578 |
| B2 | 18.97 |
| B3 | N/A |
| B4 | 15.7 |
| B5 | 39.77 |
| B6 | 27.42 |
| B7 | 59.51 |
| B8 | >100 |
| B9 | >100 |
| B10 | 18.7 |

**Figure 5. dCas9 location and Opto-CRAC activity**
(**a**) Cytosolic location of dCas9-mCherry when expressed in HeLa cells. (**b**) Time course of fluorescence changes in HeLa cells co-expressing the genetically-encoded $Ca^{2+}$ sensors (GCaMP6s) and the indicated Opto-CRAC constructs following blue light stimulation (470 nm; power density = 50 μW/cm$^2$). (**c**) Summary of the activation kinetics (activation half-lives based on representative curves shown in panel B; $t_{1/2, ON}$) of the 10 tested Opto-CRAC constructs. (**d**) Monitoring Opto-CRAC-B10 induced reversible calcium influx in HeLa cells with jR-CaMP1b ($t_{1/2, on}$ = 18.7 ± 1.4 sec; $t_{1/2}$, off = 24.5 ± 1.1 sec). Blue bar, light stimulation at 470 nm.

For the first approach, a light-sensitive NLS is designed by fusing bipartite NLS peptides[75] to LOV2 (AsLOV2) derived from Avena sativa phototropin[76] . Bipartite NLS was introduced to the C-terminal Jα helix of the AsLOV2 domain, while dCas9-Vp64 was placed at the N-terminus. In the dark, NLS is caged by the LOV2 domain and hidden from the nuclear import cargo; therefore, the fusion protein is trapped in the cytoplasm. Upon blue light illumination, photoexcitation creates a covalent adduct between LOV2 residue C450 and the cofactor FMN[76], allowing the undocking of the Jα helix to expose the NLS. The NLS binds to importin, which mediates interactions with the nuclear pore complex, thereby causing the translocation of dCas9-Vp64 from the cytosol to the nucleus. We used two different mCherry-tagged versions of bipartite NLS (NLS1 and NLS2), which has been shown to induce nuclear translocation after blue light induction[75]. But this strategy did not work out as anticipated since we failed to observe light-inducible nuclear entry of dCas9 (**Fig. 6**; constructs V1-V2).

We therefore resorted to the second photoactivatable nuclear translocation approach, which is based on a $Ca^{2+}$-dependent system, consisting of two components: i) a GFP-tagged fusion protein that contains dCas9, VP64 and an N-terminal fragment of NFAT (residues 1-460 without the DNA binding domain to avoid binding to endogenous NFAT targets), in which $NFAT_{1-460}$ was fused to either the N- or C- terminus of dCas9, and the NLS was inserted in different positions depending on the constructs; ii) Opto-CRAC, which comprises an ORAI-activating fragment from the cytoplasmic domain of STIM1 (SOAR or CAD) and a LOV2 domain to induce $Ca^{2+}$ influx following blue light stimulation.

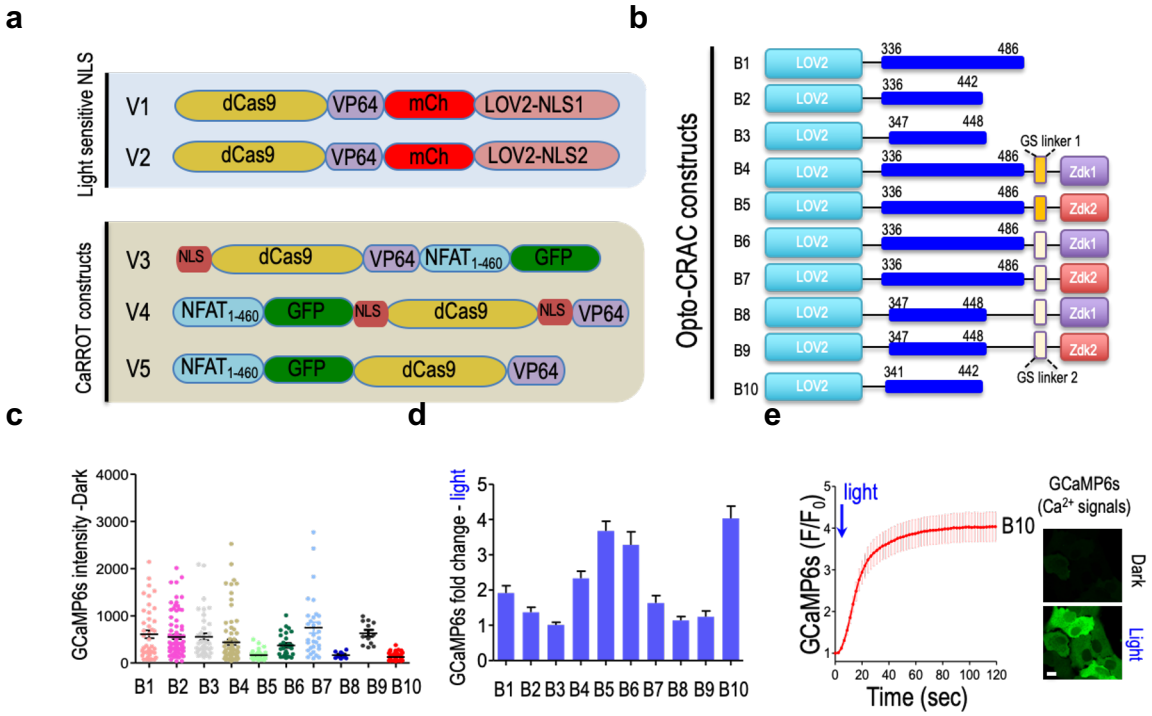


**Figure 6. Design and optimization of CaRROT and second-generation Opto-CRAC constructs to enable tight control of dCas9 nuclear translocation.**
(**a**) Design of dCas9-fusion constructs for inducible nuclear translocation: i) fusion with light-sensitive NLS signals (BiNLS: V1-V2); or ii) through $Ca^{2+}$-dependent nuclear translocation (V3-V5). (**b**) Opto-CRAC designed to photo-induce $Ca^{2+}$ influx by optimizing STIM1-CT fragments, the linker, and fusion to LOV2-binder Zdk. (**c**) Basal fluorescence intensities of GCaMP6s-HeLa cells transfected with indicated Opto-CRAC constructs in the dark. At least 30 cells were analyzed in the assay for each construct. (**d**) Light-inducible fold-change in the GCaMP6s fluorescence intensity (at 2 min post-photostimulation at 470 nm; 50 μW/cm$^2$) in HeLa cells expressing the indicated second generation Opto-CRAC constructs. Data were shown as mean ± S.D. (n=30 cells from three independent experiments). (**e**) Time course showing light-inducible increase of GCaMP6s signal in HeLa cells expressing Opto-CRAC-B10. Representative images showing GCaMP6s fluorescence before and after light stimulation are presented on the right. Data are shown as mean ± S.D. (n=30 cells).

In the dark, the SOAR/CAD domain was caged by LOV2 to prevent the activation of ORAI calcium channels. Following blue light exposure, the unwinding of the LOV2-Jα helix promoted the exposure of SOAR/CAD, which subsequently moved toward the plasma membrane to directly engage and activate ORAI1 $Ca^{2+}$ channels[8,15,77-80].

The prototypical design of Opto-CRAC contains LOV2 and a STIM1 cytosolic fragment (aa 336-486) as we described previously[15]. However, this construct showed appreciable dark activity (construct B1, **Fig. 6b-c**), which might cause constitutive nuclear translocation of NFAT in the dark. To confer tighter control over the CaRROT system, we created a series of second generation Opto-CRAC constructs by i) varying

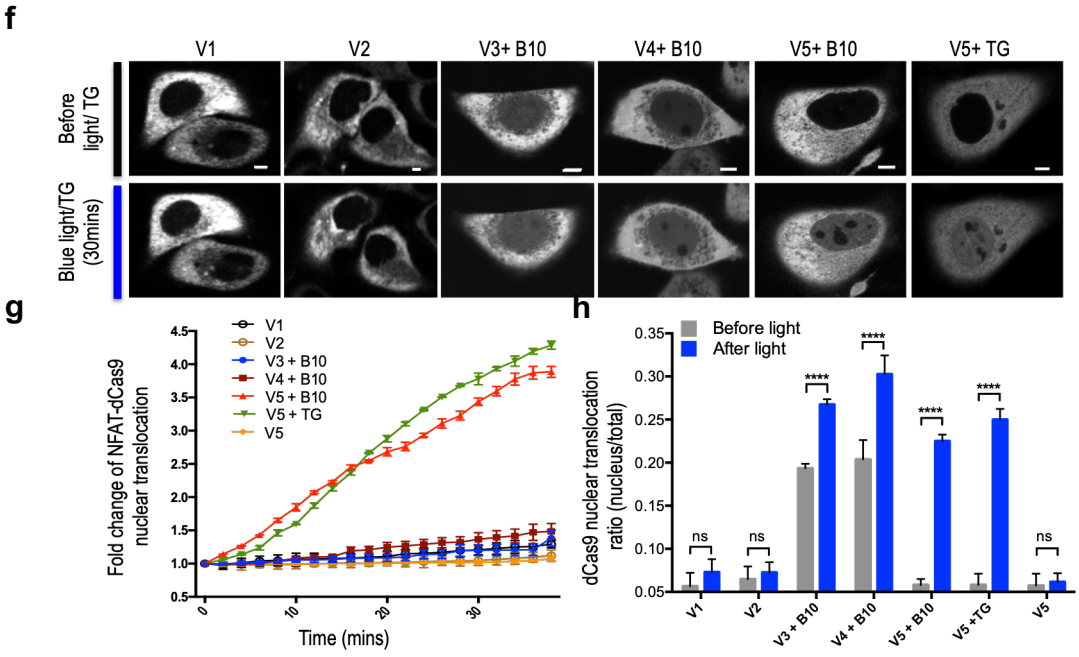


**Figure 6. Design and optimization of CaRROT and second-generation Opto-CRAC constructs to enable tight control of dCas9 nuclear translocation. (Continued).** ((**f**) Monitoring light-inducible translocation of dCas9-VP64 or dCas9-$NFAT_{1\text{-}460}$-VP64 from cytosol to the nucleus in the same cells expressing the indicated constructs by confocal imaging. (**g-h**) Time course showing the fold-change of nuclear GFP intensity following blue light stimulation (g) and quantification of signals before and after light illumination for 30 min (h). Data are shown as mean ± S.D. (n=9). Data are shown as mean ± SD (n = 9). Scale bar: 5 μm. ****$P < 0.0001$ compared to the dark group (two-tailed Student's *t*-test).

the length of STIM1-CT fragments (B1-3; **Fig. 6b**); ii) fusion to Zdark (Zdk) protein[81], a light-dependent LOV2 binder, and changing the linkers (B4-9); or iii) using a SOAR domain derived from other species (such as zebrafish; B10). After transfecting Opto-

CRAC constructs to a GCaMP6s-stable HeLa cells, we next set out to identify the best performing construct based on two criteria: i) reduced dark activity; ii) enhanced dynamic range of calcium signal changes in response to light stimulation. Since Zdk binds to LOV2 tightly in the dark but dissociates from LOV2 upon light stimulation[81], we reasoned that Zdk might serve as an additional 'lock' to further cage the LOV2-SOAR fusion in a quiescent configuration, thus reducing the background activation. Indeed, some of the Zdk constructs showed substantially reduced dark activity (constructs B5, B6, and B8; **Fig. 6c**). However, in some constructs, the addition of Zdk led to a narrower dynamic range (B8 and B9, **Fig. 6d**) and slower onset of light-inducible $Ca^{2+}$ responses when compared to B1 (**Fig. 5b and 5c**). Ultimately, the chimera made of LOV2 and *D. rerio* SOAR (DrSOAR; residues 341-442) turned out to be an ideal candidate with negligible dark activation but potent photo-induced calcium influx, with activation and deactivation half-lives of 18.7 sec and 24.5 sec, respectively (construct B10; **Fig. 5d** and **Fig. 6d-e**). We therefore used this construct for our downstream applications.

***Chemical and photo-inducible nuclear translocation of dCas9.***

We next evaluated the dCas9 nuclear translocation of different designs upon blue light illumination by transfecting HeLa cells with mCherry-tagged dCas9-VP64-LOV2-NLS constructs (**Fig. 6a**, constructs V1 and V2) or co-transfecting LOV2-DrSOAR (construct B10) with various CaRROT constructs (**Fig. 6a**, constructs V3-5). When expressing mCherry-tagged V1 or V2, dCas9 underwent very low translocation from cytosol to nuclei in response to blue light illumination (**Fig. 6f**, first and second panels), suggesting that either the NLS is not strong enough or not fully exposed to drive nuclear entry of dCas9. Contrariwise, for cells transfected with V3 or V4, dCas9 was observed in the nuclei prior

to light illumination when co-transfected with Opto-CRAC-B10 (**Fig. 6f**, third and fourth panel). This result indicated that the NLS inserted in these constructs had a strong affinity for the import machinery, which shuttled the fusion protein into the nucleus even in the dark. After removing all the NLSs in dCas9, the CaRROT construct V5 remained exclusively in the cytosol in the dark. Upon light stimulation, CaRROT-V5 showed light-inducible translocation into the nuclei of cells co-transfected with Opto-CRAC-B10 (~3.5-fold change; **Fig. 6f-g**). This system also showed no discernible dark-state background activity (**Fig. 6h**), which was concordant with the minimal $Ca^{2+}$ influx "leakiness" of the improved Opto-CRAC system (**Fig. 6c** and **6f**).

Next, to confirm that our system could be likewise manipulated by chemicals that could alter intracellular calcium signals, we used thapsigargin (TG), which blocks the sarcoplasmic/endoplasmic reticulum $Ca^{2+}$ ATPase (SERCA) pump to passively induce calcium store depletion in the ER[82]. This process is immediately followed by the activation of STIM1 to open ORAI calcium channels and cause bulk flooding of calcium ions into the cytosol. Time-lapse imaging showed that TG, similar to photo-activated Opto-CRAC, could lead to nuclear entry of dCas9 (~4-fold change in nuclear fluorescence signals; **Fig. 6f-h**). Taken together, our results establish that we could use both chemical and light to control the cytosol-to-nucleus shuttling of a dCas9-fused transcriptional effector, which is an indispensable step for the fusion protein to execute its function within the nuclei.

***Chemical and photo-activatable transcriptional modulation.***

Several previous studies have demonstrated that gene activation could be achieved by targeting a VP64 effector domain to the transcribed region of a gene[62,63,83] due to its ability to recruit basal transcriptional machinery[84]. In our design, the dCas9-sgRNA complex serves as a locus-positioning apparatus to direct VP64 to targeted

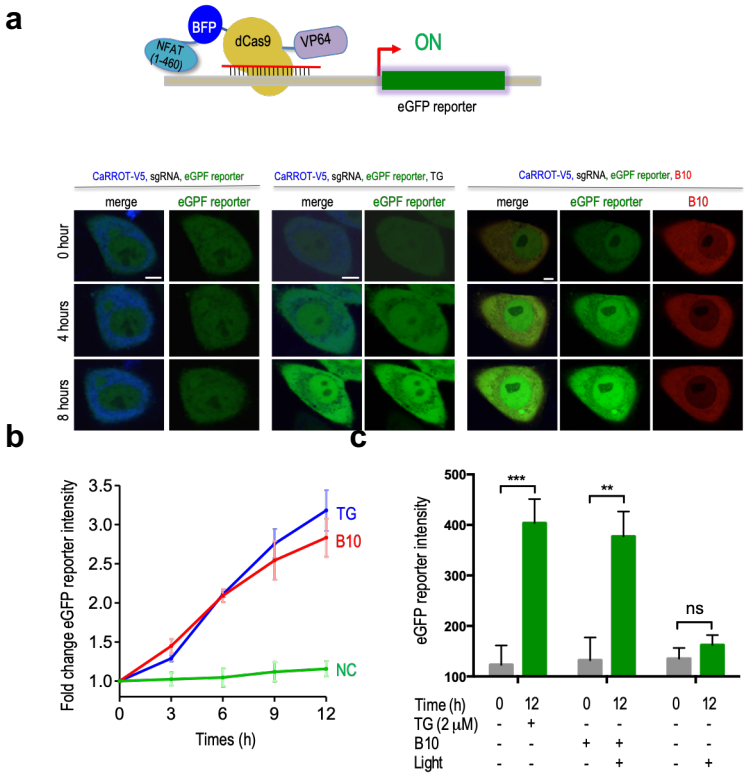


**Figure 7. Use of CaRROT to chemically or photo-induce EGFP reporter expression.**
(**a**) Monitoring the EGFP reporter signals in HeLa cell expressing the indicated set of constructs with the combination of Opto-CRAC-B10 or chemical (TG, 2 μM). Scale bar: 5 μm. (**b**) Time course showing the changes of GFP signals in the same imaging field under the indicated conditions. (**c**) Quantification of EGFP reporter intensities before and after light or TG treatment. Data were showed as mean ± S.D. (n=9). ***P*<0.01; ****P* < 0.001 compared to untreated conditions (two-tailed Student's *t*-test).

genomic loci, e.g., promoters of targeted genes (**Fig. 7a**). To rapidly evaluate if our CaRROT system can precisely control gene expression in response to light or chemicals,

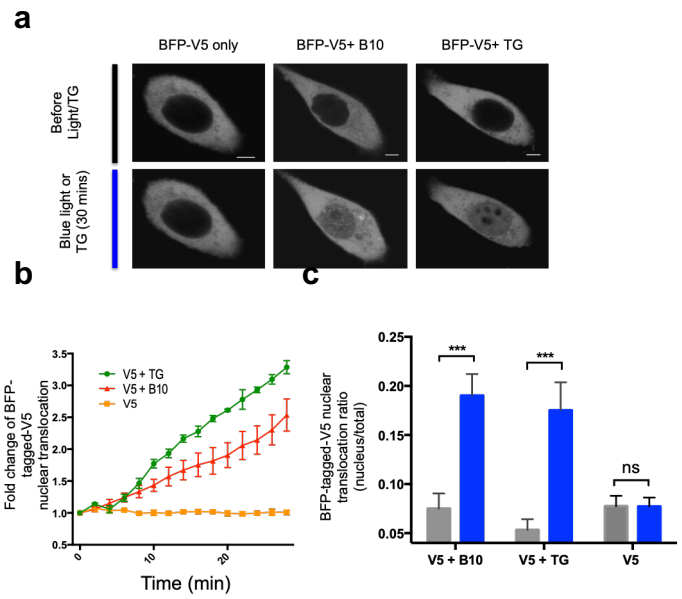


**Figure 8**. **BFP-tagged CaRROT-V5**
(**a**) Light- or TG-inducible nuclear translocation of BFP-tagged CaRROT-V5 monitored in the same cells by confocal imaging. (**b-c**) Time course showing the fold-change of nuclear BFP intensity following blue light stimulation (b) and quantification of signals before and after light illumination for 30 min (c). Data are shown as mean ± S.D. (n=9). Scale bar: 5 μm. ****P* < *0.001* compared to the dark group (two-tailed Student's t-test).

we used an EGFP reporter assay, in which eight repeats of a guide RNA target sequence were situated upstream of a minimal cytomegalovirus (CMV) promoter[85]. Since the activated reporter expressed EGFP, we replaced the GFP module on the CaRROT-V5 construct by BFP to avoid fluorescence overlap. Similar to the GFP-tagged version, BFP-tagged CaRROT-V5 showed undetectable dark-state background activity, but underwent nuclear translocation when co-transfected with Opto-CRAC-B10 upon blue light

stimulation or TG treatment (**Fig. 8a-c**). After addition of TG to induce calcium influx in cells transfected with BFP-tagged CaRROT-V5 and corresponding sgRNA, we observed a pronounced increase in EGFP levels compared with control cells without TG

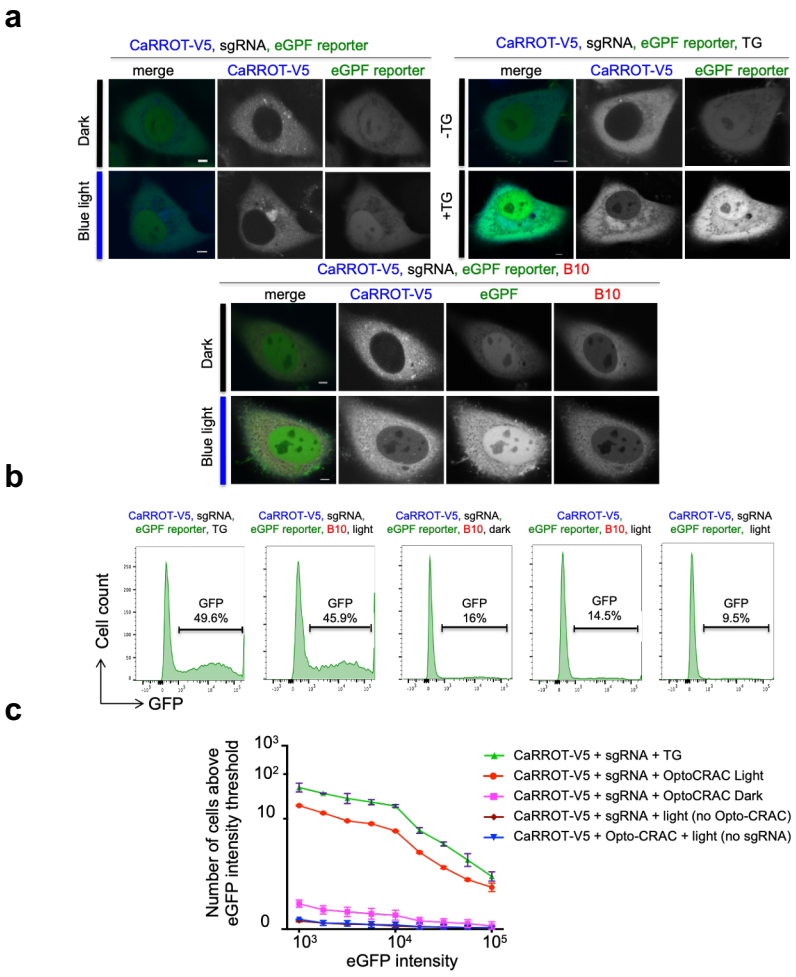


**Figure 9**: **Activity of EGFP-reporter**
(**a**) Activity of EGFP-reporter induced by indicated set of constructs with the combination of Opto-CRAC-B10 or chemical (TG, 2 µM), CaRROT-V5 and corresponding sgRNA in the dark or without TG (upper panels) or exposed to blue light or TG (lower panels) under different microscopic fields. Scale bar: 5 µm. (**b-c**) The number of EGFP-positive cells was counted by flow cytometry (shown are representative data from one experiment, n = 2).

administration per different microscopic fields (**Fig. 9a**, second panel). We performed a similar experiment by using Opto-CRAC-V5, rather than TG, to elicit calcium entry, and noticed a similar increase of EGFP expression (**Fig. 9a**, last panel). As a control, cells

transfected with CaRROT-V5 and sgRNA did not show a significant increase of EGFP signals regardless of the presence of light (**Fig. 9a**, first panel).

To better visualize the behavior in the same transfected cells at real time in response to blue light, we co-transfected different sets of vectors for 24 hours into Hela cells, and then recorded the time-lapse imaging with pulsed photostimulation (blue LED at 470 nm; power density of 0–50 μW/mm$^2$; 5 sec ON, 20 sec OFF) or by adding TG to

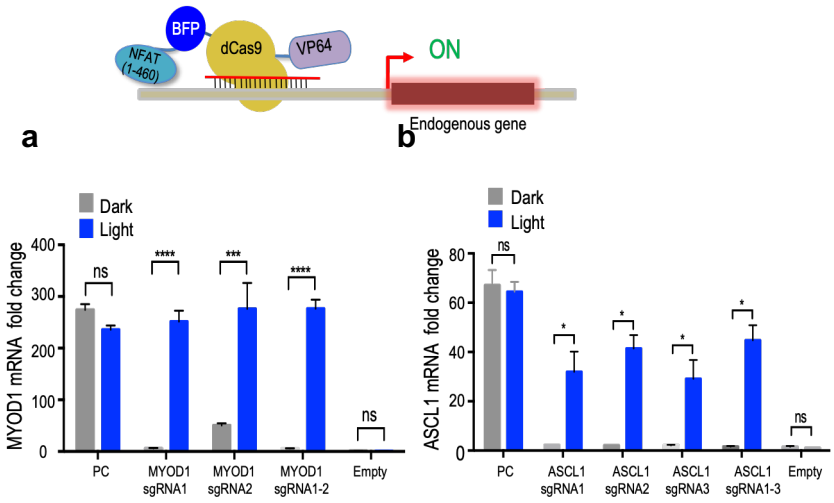


**Figure 10**. **CaRROT-mediated light-inducible activation of endogenous gene expression.**
Light-induced endogenous gene expression of (a) MYOD1 and (b) ASCL1 in HEK293T cells was measured by qRT-PCR. Cells were transfected with dCas9-NLS-VP64 as positive control (PC), BFP-tagged-CaRROT-V5 construct, Opto-CRAC-B10 and indicated sgRNAs or the empty plasmid (pTriEX-BFP). Cells were subjected to pulsed blue light stimulation (470 nm, 40 μW/cm2). *P < 0.05; ***P < 0.001; ****P < 0.0001 compared to the dark group (two-tailed Student's t-test).

the cells (12 hrs). The assay was performed with the following three groups: i) BFP-tagged CaRROT-V5, sgRNA, Opto-CRAC-B10 and EGFP reporter; ii) BFP-tagged CaRROT-V5, sgRNA, adding TG and EGFP reporter; iii) BFP-tagged CaRROT-V5, sgRNA and EGFP reporter as a negative control. The addition of TG to CaRROT-V5-transfected cells (**Fig.**

**7a**, middle panels) turned on the EGFP signal to statistically significantly higher levels than cells that only received CaRROT-V5 and the reporter construct (**Fig. 7a**, left panels). a similar trend was observed in the group of cells transfected with CaRROT-V5 and Opto-CRAC-B10, in which the EGFP signals following illumination were markedly higher than before light stimulation or in the negative control (**Fig. 7a**, right panels). The EGFP signals increased up to three-fold compared to baseline (**Fig. 7b**).

Each cell probably received a different amount of the vector mixture; therefore, the evaluation of the EGFP intensity of the whole cell population would reflect better the efficiency of the CaRROT system. We therefore used flow cytometry to quantify the numbers of cells showing chemical or light-inducible activation of the EGFP reporter (**Fig. 9b**). Since the magnitude of the difference between cells irradiated with light and incubated in the dark varied with the threshold gate applied to the EGFP fluorescence intensity, we calculated the number of EGFP-positive cells at different indicated threshold gates. The cells transfected with CaRROT-V5, Opto-CRAC-B10, sgRNA, and EGFP reporter and subjected to light illumination presented a statistically higher number of $EGFP^+$ cells than either cells kept in the dark or the negative control group at any threshold (**Fig. 9c**). A similar trend was also observed in the group receiving CaRROT-V5 and TG, which showed a significant enrichment of $EGFP^+$ cells compared to negative controls (**Fig. 9c**).

To demonstrate that our synthetic system would also allow photoactivation of endogenous genes, we used a set of sgRNAs designed to target the promoter region of the human achaete-scute family bHLH transcription factor 1 (*ASCL1*) or myogenic differentiation 1 (*MYOD1*), and then evaluated their light-dependent transcription in

HEK293T cells. ASCL1 acts as a pioneer transcription factor to control neuronal differentiation[86]; whereas MyoD is a key regulator for skeletal muscle differentiation, which is able to induce transdifferentiation of fibroblasts or other cell types into myocytes[87]. Based on their fundamental roles in developmental biology[88,89], light-inducible expression of *ASCL1* or *MYOD1* will likely be useful for future temporal control of the differentiation of neurons or muscle cells in regenerative medicine. We therefore chose these two genes to test the CaRROT system. Cells transfected with dCas9-NLS-VP64 were used as a positive control, which showed light-independent expression of both genes (left bars, **Fig. 10a-b**). For cells transfected with CaRROT-V5 and Opto-CRAC-B10, we observed a significant increase in gene expression upon light illumination for each individual or combined sgRNAs. For MYOD1, the mean levels of expression were enhanced by over 200-fold, which was comparable to those of dCas9-NLS-VP64 expressing cells (**Fig. 10a**). This remarkable light-dependent transcription induction was also observed when we targeted the ASCL1 locus (**Fig. 10b**). In all cases, gene expression levels in cells maintained in the dark were comparable to cells transfected with the empty vectors (right bar, **Fig. 10a-b**). Notably, the coexpression of our system with two sgRNAs targeting MYOD1 or three sgRNAs targeting ASCL1 did not show a significant difference compared to individual sgRNA transfection, suggesting that the expression of multiple guide RNAs targeted to the same gene does not seem to cause synergistic activation of both endogenous genes ASCL1 and MYOD1 (**Fig. 10a-b**). This observation also indicates that by using our system, one well-designed sgRNA probably would be sufficient to activate the expression of endogenous genes.

## Conclusion and Discussion

In summary, we have devised a synthetic transcriptional reprogramming device (CaRROT) that can be tightly controlled by chemicals or light to induce endogenous gene transcription with high precision. Since the system relies on the generation of $Ca^{2+}$ signals to drive nuclear translocation of CaRROT, it can be further extended to record or permanently mark $Ca^{2+}$ dependent activities in neurons or lymphocytes once coupled with a reporter gene (e.g., GFP or luciferase).

# CHAPTER III
# NANO-OPTOGENETIC IMMUNOENGINEERING: PHOTO-TUNABLE REMOTE CONTROL OF CAR T-CELLS

## Introduction

Chimeric antigen receptor (CAR) T-cell immunotherapy has demonstrated a high potential for the elimination of tumors, particularly in patients with CD19-positive lymphoma and leukemia[90]. CARs are synthetic receptors engineered to be expressed on the surface of T cells, where they can engage specific tumor antigens in a major histocompatibility complex (MHC)-independent manner[30]. Antigen recognition allows engineered T cells to be activated and subsequently perform their killing/effector activities toward tumor cells. A typical FDA-approved second-generation CAR contains an antibody-derived single chain variable fragment (scFv) in the extracellular domain, a transmembrane domain, costimulatory signals (e.g., 4-1BB), and the intracellular signal transduction component known as the immunoreceptor tyrosine-based activation motif (ITAM) derived from CD3ζ. The latter component constitutes an essential subunit of the T cell receptor required for T cell activation[34]. Despite the tremendous success of CAR T-cell therapy in cancer treatment[38,90,91], this type of immunotherapy imposes significant safety challenges due to the lack of control over the dose, location, and timing of T cell activity[34]. This is most notably exemplified by cytokine release syndrome (CRS) and "on-target, off-tumor" cytotoxicity[34]. While the recently FDA approved CAR T-cell therapies (Kymriah[91] and Yescarta[92]) are designed to target CD19-positive tumors, they cannot discriminate between normal $CD19^+$ cells and cancerous $CD19^+$ cells. As such, CAR T-cells will likely attack normal cells or tissues, leading to B cell aplasia[41] or even more devastating systemic consequences in certain patients[93], thereby posing

limitations on the use of current CAR T-cell therapy regimens. Besides the obstacles in hematological malignancies, challenges also remain for CAR T-cell therapy in solid tumors such as targeting carcinoembryonic antigen (CEA) in gastrointestinal carcinoma[94], EFGRvIII antigen in glioblastoma[95], or ganglioside (GD2) antigen in neuroblastoma[96]. The reasons for these barriers are mostly due to the hostile tumor microenvironment[94,97], limitations in CAR T trafficking and infiltration to tumor sites[96,98], and unspecific target antigens[95,99]. To overcome these limitations, several strategies have been proposed, including arming CAR-T cells with knock-out of PD-1 expression to reduce responsiveness to the immunosuppressive tumor microenvironment or altering the expression of chemokine receptors[100], as well as the secretion of cytokines on engineered CAR T cells[37]. Despite these efforts, CAR T therapy for solid tumors has not been approved by FDA for clinical use at present. Due to current drawbacks, intelligent CAR-T cell-based therapies with precise spatiotemporal control over therapeutic activities are urgently needed.

Here, we describe the engineering of light sensitivity into the chimeric antigen receptors to create light-switchable CAR (LiCAR) T-cells. Given the success of CAR T cells in hematological malignancies and its tremendous well-studied background, we focused our efforts on targeting the CD19 antigen. LiCAR-expressing T-cells can selectively produce anti-tumor immune responses in the dual presence of tumor antigen and light. To enhance the feasibility of such wireless optogenetic intervention *in vivo*, we further combined LiCAR with surgically removable upconversion nanoplates (UCNPs) that have enhanced near infrared (NIR)-to-blue upconversion luminescence. The UCNPs act as miniature light transducers that allow inducible activation of CAR T-cells

in living animals to occur upon stimulation with deep tissue-penetrable NIR light. This NIR light-tunable nano-optogenetic immunomodulation platform enables spatiotemporal control of CAR T-cell mediated cytotoxicity against both hematological malignancies and solid tumors with tailored doses and duration.

## Materials and Methods

### *Molecular Cloning and Plasmid Construction*

To construct plasmids encoding Component I (A0, C0, E0, and G0), gBlocks gene fragments were synthesized by Integrated DNA Technologies (Coralville, Lowa, USA) to generate the following cDNA sequences: CD8 signal peptide, Myc tag, anti-CD19 scFv, CD8-alpha transmembrane domain, hinge region, and 4-1BB. The synthetic block was inserted between the NheI-XhoI restriction sites into the mCerulean N1 vector (#27795; Addgene, Watertown, Massachusetts, USA). The optical dimerization components, including CIBN (#60553; Addgene), LOV2-ssrA (#60413; Addgene), CRY2PHR (#89877; Addgene), sspB (#60410; Addgene) were first amplified via standard PCR with KOD Hot Start DNA polymerase (EMD Millipore, Burlington, Massachusetts, USA), and then inserted downstream of 4-1BB between the XhoI-XmaI sites. Two linkers, GSGSGEF and GSGSGSGS, were introduced before and after the dimerization modules, respectively. EGFP was amplified from the hRIP3-eGFP vector (#41387; Addgene) and then inserted between the AgeI-NotI restriction sites to replace mCerulean in the backbone vector. For Component I constructs, we generated versions with or without eGFP. To facilitate PM localization, Component I was further modified by inserting (i) a short ER export sequence to the N-terminus and (ii) an ER trafficking signal between the AgeI and MluI sites in front of eGFP in constructs A0 and C0.

To construct plasmids encoding Component II (constructs B1.0/D1.0), we sequentially introduced the 4-1BB, sspB and human CD3ζ intracellular chain derived from gBlocks gene fragments and inserted them between the KpnI, EcoRI, HindIII, and BamHI restriction sites upstream of mCherry in the pmCherry2-N1 vector (#54517; Addgene). CRY2PHR (#89877; Addgene) was used to replace sspB to generate CRY2-based constructs.

To create B2.0/D2.0 constructs, we rearranged the intracellular CAR components, and optical dimerization molecules with mCherry, 4-1BB, CD3ζ, and sspB/CRY2 were sequentially inserted into the BamHI, XhoI, EcoRI, and ApaI sites of pcDNA3.1 (+). The plasma membrane (PM)-tethered Component II constructs (B3/D3) were designed by fusing the CD8-alpha hinge and transmembrane domain upstream of the 4-1BB module in the reorganized CAR construct (4-1BB, CD3ζ, mCherry, and CRY2/sspB). B4/D4 were generated by placing DAP10 (gBlock gene fragment) and the CD8-alpha transmembrane domain upstream of 4-1BB in the B1.0/D1.0 constructs between the XhoI and KpnI restriction sites. The defective LiCAR constructs (B5/D5) were generated from B4/D4 by removing the T cell-activating CD3ζ component. To reduce undesired nuclear accumulation, an NES sequence was inserted into the N-terminus of Component II constructs between the NheI and XhoI sites. Construct D4.1 and D4.2 were generated by replacing sspB from construct D4 and D2 by sspB (R73Q) (#60420; Addgene) between the EcoRI/HindIII and EcoRI/ApaI sites, respectively. Construct D4.3 and D4.4 were generated by introducing the point mutation A58V to sspB in the original construct D4 and D2 by using the QuikChange Lightning Multi Site-

Directed Mutagenesis Kit (Agilent Technologies, Santa Clara, CA, USA) following the manufacturer's instructions.

For viral transduction, the pMSGV1 retroviral vector (#107227; Addgene) and MIGR1 (#27490; Addgene) were used as the backbones into which all the optimized CAR or LiCAR components were inserted between two modified restriction enzyme sites, HpaI and PacI. The helper plasmids including the gag/pol viral packaging vector (#14887; Addgene), a modified envelope vector encoding the amphotropic envelope glycoprotein RD114 (#17576; Addgene), and packaging vector pcl-Eco (#12371; Addgene) were acquired from Addgene.

***Mammalian Cell Culture, Transfection and Fluorescence Microscopy***

An NFAT-dependent luciferase reporter in a Jurkat cell line was used to examine NFAT-dependent gene transcription as previously described[15]. Human cancer cell lines (K562 myelogenous leukemia cells (#CCL-243), Daudi (#CCL-213) and Raji cell lymphoblasts (#CCL-86)) were purchased from the American Type Culture Collection (ATCC, Manassas, Virginia, USA), and cultured in Roswell Park Memorial Institute (RPMI 1640) medium with L-glutamine (#MT10040CV, Thermo Fisher Scientific, Waltham, Massachusetts, USA) supplemented with 10% FBS, 100 units/ml penicillin and 100 µg/mL Streptomycin (Gibco, Big Cabin, Oklahoma, USA). B16-OVA and the B16-OVA mouse melanoma cell lines transduced with an amphotropic virus containing human CD19 (hCD19) (gifts from Dr. Anjana Rao, La Jolla Institute for Immunology) were maintained in Dulbecco's Modified Eagle Medium (DMEM) (#MT10013CV, Thermo Fisher Scientific) supplemented with 10% FBS, 100 units/ml penicillin and 100

μg/mL Streptomycin (Gibco). The CD19 level of each cell line was quantified by staining the cell surface with a monoclonal antibody against CD19 (APC-conjugated; #17-0199-42; eBioscience, San Diego, California, USA) in FACS buffer (PBS, 2% BSA, and 2 mM EDTA) at 4 $^{o}$C for 30 min. The stained cells were washed three times with FACS buffer, and the levels of fluorescence protein were determined by using a LSRII flow cytometer (BD Biosciences, San Jose, California, USA). Cells were sampled at a medium flow rate, and at least 10,000 cells were counted for each condition. FACSDiva8.0 (BD Biosciences) and FlowJo software v10.5.3 (TreeStar, Ashland, Oregon, USA) were used to analyze the data ($APC^+$ cell populations).

HeLa cells from ATCC (#CCL-2) were maintained in Dulbecco's Modified Eagle Medium (DMEM) (#MT10013CV, Thermo Fisher Scientific) supplemented with 10% FBS, 100 units/ml penicillin and 100 μg/mL Streptomycin (Gibco) at 37 °C in a humidified atmosphere under 5% $CO_2$. For confocal imaging, $10^5$ cultured cells were seeded on 35 mm glass-bottom dishes. After 24 h, LiCAR components I (1000 ng) and II (600 ng) were co-transfected into HeLa cells using Lipofectamine 3000 (Life Technologies; Carlsbad, California, USA) according to the manufacturer's instructions. Confocal imaging was performed at 24 h post-transfection by using an inverted Nikon Eclipse Ti-E microscope customized with Nikon A1R+ confocal laser sources (405/488/561/640 nm). A 488-nm laser was used to excite GFP, which also served as an internal light source for photo-stimulation in some cases, and a 561-nm laser was used to excite mCherry fluorescence. The cells were subjected to two dark-light cycles, in which each cycle had fifteen repetitions of 1-s stimulation and either 3-min of image acquisition for LOV2-based constructs or 6 minutes for CRY2-based constructs. At least

four GFP- or mCherry-positive cells were selected to calculate the cytosolic fluorescence at selected areas before and after photo-stimulation ($\Delta F/F_0$).

### *Isolation and Culture of Primary Human T Cells*

Peripheral blood mononuclear cells (PBMCs) were collected from blood samples of healthy blood donors through the Gulf Coast Regional Blood Center (Houston, Texas, USA) by density gradient centrifugation using the Ficoll-Paque Plus media (#GE17-1440-02; Sigma, St. Louis, Missouri, USA). PBMCs were washed three times with sterile PBS and resuspended at a concentration of $1 \times 10^6$ cells/ml in PBS supplemented with 2% BSA and 2 mM EDTA. $CD8^+$ T cells from PBMCs were enriched by magnetic cell sorting, using negative selection kits (#130-096-495; Miltenyi Biotec, Auburn, California, USA). The purity of the $CD8^+$ cell populations was determined using flow cytometry by staining with APC-conjugated anti-human CD8 (#344721; Biolegend). $CD8^+$ T cells were cultured in RPMI L-glutamine medium supplemented with 10% FBS, 1X NEAA (non-essential amino acid medium; #1939940; Gibco), 1 mM sodium pyruvate (#13-115E; Lonza, Houston, Texas, USA), 10 mM HEPES (#15630-080; Gibco), 0.55 µM 2-mercaptoethanol (#21985023; Gibco**)**, 100 units/ml penicillin, and 100 µg/mL streptomycin. Recombinant human IL-2 (#PHC0027; Gibco) was used at a final concentration of 100 IU/mL for culturing $CD8^+$ cells.

### *Isolation and Culture of Mouse T Cells*

Spleens were excised from 6 – 12 week old C57BL/6 mice and put in 5 ml of FACS buffer. Each spleen was then transferred to a 100 µm cell strainer atop a 35 mm

plate containing 2 ml of FACS buffer. The plunger of a small syringe was used to crush the spleen on the strainer. The cell suspension from the plate beneath was collected and briefly centrifuged. Red blood cells were removed from the cell pellets by resuspension in 1 ml of ACK lysis buffer (#10-548E; Lonza) for 1 minute. After that, AKC buffer was diluted by adding 9 ml FACS buffer. The cells were then harvested, washed one more time, and resuspended at a concentration of $1 \times 10^6$ cells/ml in FACS buffer. Mouse spleen $CD8^+$ T cells were enriched by magnetic cell sorting using negative selection kits (#130-104-075; Miltenyi Biotec). The purity of the $CD8^+$ cell populations was determined using flow cytometry by staining with anti-mouse CD8a eFluor 450 (#48-0081-82; eBioscience). Mouse $CD8^+$ T cells were cultured in TexMACS media (#130-097-196; Miltenyi Biotec) supplemented with 10% FBS, 100 units/ml penicillin, and 100 µg/mL streptomycin. 400 µg/mL anti-mouse CD3 (#50-139-2707, Fisher Scientific), 400 µg/mL anti-mouse CD28 (#50-562-020, Fisher Scientific), and 100 IU/mL recombinant mouse IL-2 (#PMC0025; Gibco) was freshly added to the medium each time used.

***Viral Transduction of Jurkat T cells and Primary T Cells***

Retroviruses encoding the conventional CAR or engineered CARs were packaged in HEK293T cells (#CRL-3216; ATCC) transfected with the corresponding retroviral vector pMSGV1, the gag/pol viral packaging vectors (#14887; Addgene) and a modified vector encoding the amphotropic envelope glycoprotein RD114 (#17576; Addgene) using the iMFectin DNA Transfection Reagent (#I7200-101; Gendepot, Katy, Texas, USA). For mouse T cell transduction, the retroviruses were packed in Plate-E

cells (#RV-101; Cell Biolabs, San Diego, California, USA) transfected with the packaging vector pcl-Eco (#12371; Addgene) and MIGR1-WT CAR, MIGR1-LiCAR, or MIGR1-defective CAR constructs. The supernatant containing packaged viruses was collected twice at 48 hours and 72 hours after transfection.

Cultured Jurkat T cells at a concentration of $10^5$ cells/ml were co-incubated with 2 ml of the 0.45 μM filtered virus supernatant and 10 μg/ml of polybrene per well in a 12-well plate format. Plates containing cultured cells were centrifuged at 2000 x g for 2 hours at 32 °C and incubated 2 more hours at 37°C. The viral supernatant was removed and replaced with fresh RPMI medium supplemented with 10% FBS, 100 units/ml penicillin and 100 μg/mL streptomycin. Cells were repeatedly transduced four times to yield a high transduction efficiency.

For human primary T cells, the virus-containing supernatant was first concentrated using an Amicon Ultra-15 Centrifugal Filter (#UFC903024; Millipore Sigma, *St. Louis,* Missouri*, USA*). Before performing T cell transduction, human primary $CD8^+$ T cells were activated for 48 hours using the Dynabeads Human T-Activator CD3/CD28 system (#11132D; Thermo Fisher Scientific) at a bead-to-cell ratio of 1:1. Retroviral transduction of primary T cells was performed by mixing concentrated viruses and RetroNectin (#T100B; Takara Bio, Mountain View, California, USA) with T cells according to the manufacturer's instructions.

For mouse primary T cells, $CD8^+$ T cells were activated overnight in IgG (H+L) goat anti-Hamster (#PI31115, Fisher Scientific)-coated plates and soluble anti-mouse CD3 (#50-139-2707, Fisher Scientific) and anti-mouse CD28 (#50-562-020, Fisher Scientific) in mouse T cell culture medium. Mouse T cells were transduced with 2 ml of

0.45-μM filtered virus supernatant and 10 μg/ml of polybrene per well in a 12-well plate. Both human and mouse primary T cells were transduced by centrifugation two times to achieve efficient transduction. Expression of transgenes was confirmed by detecting fluorescent reporters using an LSRII flow cytometer (BD Biosciences).

### *In Vitro Quantification of NFAT-Luciferase (NFAT-Luc) Reporter Activity of Jurkat-Luc T cells*

Jurkat T cells expressing conventional CARs, LiCAR, or defective LiCAR ($10^5$ cells/well) were co-cultured with cognate CD19-positive Raji cells or non-cognate CD19-negative K562 cells at indicated effector T cell: target cell (E/T) ratios or at the ratio of 1:3 in a 96-well flat-bottom microplate (#E17073EF; Greiner Bio-one, Monroe, North Carolina, USA). Plates with cells were incubated at 37 °C in a humidified atmosphere under 5% $CO_2$ and either kept in the dark or subjected to photostimulation (470 nm at a power density of 40 mW/cm$^2$) for 1 to 25 minutes and then with pulsed blue light (10-30 sec ON, 100 sec OFF) for up to 8 hours. Cell pellets were then harvested, and luciferase activity was assayed by using the Dual Luciferase Reporter Assay System (Promega, Fitchburg, Wisconsin, USA) on a Cytation 5 luminescence microplate reader (BioTek, Winooski, Vermont, USA). Data plots were generated by using Prism version 8.0.0 software (GraphPad, San Diego, California, USA).

### *ELISA for Detection of Cytokine Production*

Jurkat cells expressing conventional CARs, LiCAR, or defective LiCAR ($10^5$ cells/well) were mixed with either $CD19^+$ Raji cells or $CD19^-$ K562 cells at an E/T ratio of

1:3, while mouse CD8 T cells transduced with viruses encoding CAR constructs were co-cultured with B16-OVA or B16-OVA-hCD19 at the indicated E:T ratios. The cells were incubated in the dark or exposed to blue light (470 nm at a power density of 40 $mW/cm^2$) continuously for 1 to 25 minutes and then to pulsed blue light (10-30 sec ON, 100 sec OFF) for up to 12 hours. Cell supernatants were collected and analyzed with BD OptEIA Human IL-2 ELISA Set (#555190; BD Biosciences, San Jose, California, USA) or mouse IFN-γ ELISA set (#88-7314-22, Invitrogen, Carlsbad, California, USA) according to the manufacturer's instructions. Briefly, one day before collecting cell supernatant, a 96-well flat-bottom microplate (#E17073HT; Greiner Bio-one) was coated with human anti-IL-2 or mouse anti-IFN-γ antibody (at a dilution of 1:1000 in PBS) at 4°C overnight. On day 2, the plate was washed with 200 µl PBS/0.05% Tween 20 and then blocked with 1% BSA/PBS for 2 h at room temperature. Cell supernatants were diluted 1:10 in 1% BSA/PBS before being added into the plate wells. A series of cytokine standard dilutions were applied to obtain a standard curve. The plate was then incubated at 4°C overnight. The next day, 100 µl of biotin-conjugated detection antibody (1:1000 in 1%BSA/PBS) was added and incubated with cell supernatants for 1 hour at RT. The plate was then washed and incubated with HRP streptavidin (1:3000 in 1% BSA/PBS) at RT for 30 min. After a final wash, each well was incubated with 100 µl of the tetramethyl-benzidine substrate solution (#34028, Thermo Fisher Scientific). 50 µl of 2.5N $H_2SO4$ (#35348, Honeywell Fluka, Mexico City, Mexico, USA) was added to each well to stop the reaction. For mIL-6 quantification, mouse blood serum was collected and analyzed with IL-6 Mouse ELISA Kit (#KMC0062, Invitrogen, Carlsbad, California, USA) according to the manufacturer's instructions. The absorbance of each well was

measured at 450 nm using a Cytation 5 luminescence microplate reader (BioTek). The concentration of samples was calculated based on the standard curve, and data were plotted with Prism software (GraphPad).

### *Flow Cytometry Analysis on CD69 Surface Expression in T cells*

Jurkat T cells transduced with conventional CARs, LiCAR, or defective LiCAR ($10^5$ cells/well) were co-cultured with either CD19-negative (K562) or CD19-positive (Daudi/Raji) target tumor cells at a ratio of 1:3 in 96-well flat-bottom microplates (#E17073EF; Greiner Bio-one). Cells were stimulated with blue light for 20 min at a power density of 40 mW/cm$^2$ and then with pulsed blue light (10 sec ON, 60 sec OFF) for 10 h. After incubation, cells were washed and stained with an Alexa Fluor 700 conjugated anti-human CD69 antibody (#310922; Biolegend) at 4°C for 30 min in FACS buffer. Cells were washed three times in PBS and then analyzed by a BD LSRII cytometer (BD Biosciences). Data were analyzed using FACSDiva8.0 (BD Biosciences) and FlowJo software v10.5.3 (TreeStar).

### *Tumor Cell Killing Assay*

Human CD8$^+$ T cells expressing conventional CARs, LiCAR, or defective LiCAR and the cognate CD19$^+$ Daudi target cells used in this assay were maintained with a viability of over 97%. The effector T cells were co-cultured with target cells at an E/T ratio ranging from 1:1 to 1:3 using CD8 T cell medium in 96-well plates. Cells were evenly distributed into two plates, with one plate shielded from light as the control in the dark state and the other subjected to photostimulation (470 nm, power density of 40

mW/cm$^2$) for 20 min every 2 hours for the first 8 h, followed by pulsed blue light (10 s ON, 60 s OFF) for 16 h.

The mixture of human CD8$^+$ T and Daudi cells was then harvested and stained with SYTOX Blue dye (#S11348; Invitrogen) at a final concentration of 100 nM for 15 min at 4 $^o$C in FACS buffer. The cells were then washed twice and resuspended in FACS buffer and subjected to flow cytometry analysis by using a BD LSRII cytometer or a BD FACSAria sorter (BD Biosciences). FlowJo software v10.5.3 (TreeStar) was used to calculate the death rate of targeted B cells (gated on GFP$^-$, mCh$^-$, and SYTOX$^+$).

For time-lapse fluorescence microscopy, engineered CD8$^+$ T-cells were immobilized on 35-mm glass-bottom dishes by using 0.1 mg/ml poly-L-lysine (#2840311; EMD Millipore). CD19$^+$ Daudi cells and SYTOX Blue (100 nM) were subsequently added to the well in T cell culture media. Fluorescence images were acquired at 37 $^o$C and 5% $CO_2$ in a humidified atmosphere at 40x magnification. The time-lapse recording lasted for about 5 hours at an interval of 2 min under blue light illumination (blue LED at 470 nm with a power density of 40 mW/cm$^2$). The tumor cell killing activity of LiCAR T-cells (GFP$^+$, mCh$^+$) was monitored by their engagement with Daudi cells to induce target cell death, which was made visible by the SYTOX Blue nucleic acid staining dye.

For the *ex vivo* murine melanoma cell killing assay, B16-OVA-hCD19 cells were seeded onto 96-well glass bottom plates (#655892; Greiner Bio-one) with $10^3$ cells per well. Cells were incubated overnight for attachment. Mouse CD8$^+$ T cells expressing CAR constructs were added to pre-seeded B16-OVA-hCD19 cells at the indicated E/T ratios. One plate was kept in the dark and another plate was subjected to blue light illumination (470 nm with a power density of 40 mW/cm$^2$) for 20 min every 2 hours for the first 8 h,

followed by pulsed blue light (10 s ON, 60 s OFF) for 16 h. The plates were then washed three times with PBS to remove unattached T cells and dead B16-OVA-hCD19 cells. The surviving B16-OVA-hCD19cells, which remained attached to the plate bottom, were visualized by DAPI staining. A high-content confocal imaging system (In cell Analyzer 6000; GE Healthcare Life Sciences, Chicago, Illinois, USA) was used to capture the images of each well. Cell numbers were quantified using the IN Cell Developer Toolbox version 1.9 (GE Healthcare). Data plots were generated by using Prism version 8.0.0 software (GraphPad).

***Synthesis of β-$NaYbF_4$:0.5%Tm@$NaYF_4$ Core-shell UCNPs***

The β-NaYbF4:0.5%Tm@NaYF4 UCNPs were prepared by a three-step thermolysis method. In the first step, CF3COONa (0.50 mmol), Yb(CF3COO)3 (0.4975 mmol) and Tm(CF3COO)3 (0.0025 mmol) precursors were mixed with oleic acid (5 mmol), oleyamine (5 mmol), and 1-octadecene (10 mmol) in a two-neck round bottom flask. The mixture was heated to 110 °C to form a transparent solution followed by 10 min of degassing. Then the mixture was heated to 300 °C at a rate of 15 °C/min under dry argon flow, and maintained at 300 °C for 30 min to form the α-NaYbF4:0.5%Tm intermediate UCNPs. After the mixture cooled down to room temperature, the α-NaYbF4:0.5%Tm intermediate UCNPs were collected by centrifugal washing with excess ethanol (7500 x g, 30 min). In the second step, the α-NaYbF4:0.5%Tm intermediate UCNPs were redispersed into oleic acid (10 mmol) and 1-octadecene (10 mmol) together with CF3COONa (0.5 mmol) in a new two-neck round bottom flask. After degassing at 110 °C for 10 min, this flask was heated to 325

°C at a rate of 15 °C/min under dry argon flow and maintained at 325 °C for 30 min to complete the phase transfer from α to β. After the mixture cooled to room temperature, the β-NaYbF4:0.5%Tm core UCNPs were collected by precipitation with an equal volume of ethanol followed by centrifugation (7500 x g, 30 min). The β-NaYbF4:0.5%Tm core UCNPs were stored in hexane (10 mL). In the third step, the as-synthesized β-NaYbF4:0.5%Tm core UCNPs served as cores for the epitaxial growth of core-shell UCNPs. Typically, a hexane stock solution of β-NaYbF4:0.5%Tm core UCNPs was transferred into a two-neck round bottom flask, and the hexane was sequentially evaporated by heating. CF3COONa (0.25 mmol) and Y(CF3COO)3 (0.25 mmol) were introduced as UCNP shell precursors with oleic acid (10 mmol) and 1-octadecene (10 mmol). After 10 min of degassing at 110 °C, the flask was heated to 325 °C at a rate of 15 °C/min under dry argon flow, and maintained at 325 °C for 30 min to complete the shell crystal growth. After the mixture cooled to room temperature, the β-NaYbF4:0.5%Tm@NaYF4 core-shell UCNPs were collected by precipitation with an equal volume of ethanol followed by centrifugation (7500g, 30 min). β-NaYbF4:0.5%Tm@NaYF4 core-shell UCNPs were stored in hexane (10 mL). The control sample of β-NaYF4:30%Yb,0.5%Tm@NaYF4 core-shell UCNPs were synthesized similarly, except for changing the amount of Ln(CF3COO)3 according to the stoichiometric ratio.

***Synthesis of Silica Coated Core-shell UCNPs***

A silica shell was coated onto the core-shell UCNPs via a modified Stober method. In a typical process, 4 mL of the core-shell UCNP hexane solution was added to 21 mL hexane in a 50 mL one-neck round bottom flask. 1.5 mL of Igepal

CO-520 was added to the solution which was kept in a water bath while sonicated for 2 minutes. 160 µL of ammonia was added to the solution. After 30 minutes of stirring, 80 µL of TEOS (Tetraethoxysilane) was added to the solution. After 2 days of stirring, the silica-coated core-shell UCNPs were collected by precipitation with an equal volume of ethanol, followed by centrifugation (7500 x g, 30 min) for 3 times. Silica-coated core-shell UCNPs were stored in water (20 mL).

***Cell Proliferation Assay***

Cell proliferation was quantified using the WST-1 colorimetric assay (#05015944001; Sigma) according to the manufacturer's instructions. Briefly, on day 1, B16-OVA and B16-OVA-hCD19 cells were seeded in a 96-well plate ($10^3$ cells per well) in 200 µl of DMEM medium supplemented with 10% FBS, 100 unit/ml penicillin and 100 µg/mL streptomycin. After incubation for the indicated times, 20 µl of WST-1 was added to each well and incubated at 37°C, 5% $CO_2$ for 2 h. The cell plates were shaken for 1 min on a shaker. The absorbance of each well against a background control (medium with WST-1 only) was measured at 450 nm using a Cytation 5 luminescence microplate reader (BioTek). Data plots were generated by using Prism version 8.0.0 software (GraphPad).

***Mouse Syngeneic Models of Melanoma***

All animal studies were approved by the Institutional Animal Care and Use Committee of Texas A&M University Institute of Biosciences and Technology. On day 0, 6-12-week-old C57BL/6J mice (either sex) were inoculated intradermally with 2.5-5 x

$10^5$ B16-OVA and B16-OVA-hCD19 or B16-OVA-mCD19 cells depending on each experiment. When the tumors became visible, their sizes were measured with a digital caliper every day, and the tumor area was calculated in square millimeters (length x width). The tumors were allowed to grow for 8 additional days after inoculation. On day 9, 2 x $10^6$ mouse CD8 T cells expressing CAR constructs and 150 µg of UCNP were co-injected into each tumor. From day 10, LiCAR-transferred mice (hLiCAR or mLiCAR) were subjected to pulsed near-infrared light treatment (980 nm at a power density of 250 mW/$cm^2$; pulse:  20 sec ON, 5 minutes OFF for 2 hours per day). On days 16 to 19, tumors were collected from euthanized mice. For the analysis of hLiCAR T cells residing within the tumors, tumors were collected, perfused in PBS, cut into small pieces and enzymatically digested with 5 ug/ml of Liberase TL (#298569; Roche, Basel, Switzerland) for 1 hour at 37°C. Tumor cells were then filtered by using a 100 µm cell strainer. Cells were washed twice in PBS to remove cell debris and resuspended in FACS buffer. The number of adoptively transferred hLiCAR T cells was determined by detecting hLiCAR fluorescence protein using the LSRII flow cytometer (BD Biosciences). FACSDiva8.0 (BD Biosciences) and FlowJo software v10.5.3 (TreeStar, Ashland, Oregon, USA) were used to analyze the data (gated on the $GFP^+/mCh^+$ population). For the analysis of hLiCAR T-cells residing within the spleen or blood, spleen cells were isolated by crushing the spleen on the strainer as described above while blood cells were collected from the retro-orbital sinus by glass capillary from anesthetized mice. Spleen and blood cells were then treated with ACK lysis buffer (#10-548E; Lonza) to remove red blood cells. The spleen and blood cells were washed twice before performing flow cytometry analyses.

***Mouse B cell quantification***

mWT CAR T or mLiCAR T-cells/UCNPs were implanted into C57BL/6 mice bearing B16-OVA or B16-OVA-mCD19 tumors. mLiCAR-transferred mice were subjected to pulsed near-infrared light treatment (980 nm at a power density of 250 $mW/cm^2$; pulse: 20 sec ON, 5 minutes OFF for 2 hours a day). On day 0 and day 3, 200 ul of blood was collected from the retro-orbital sinus by glass capillary or from tail-clip from anesthetized mice. RBCs were then removed by using ACK lysis buffer (#10-548E; Lonza). Total cell counts in 200 ul blood were determined by using a TC20 Automated Cell Counter (Biorad, CA, USA). The percentage of B cells in the total cell population was quantified using a LSRII flow cytometer (BD Biosciences) after staining cells with a monoclonal antibody against mCD19 (APC-conjugated; #17-0193-82; eBioscience) in FACS buffer at 4 $^oC$ for 30 min. The stained cells were washed three times with FACS buffer and were sampled at a medium flow rate with 10,000 cells counted. FACSDiva8.0 (BD Biosciences) and FlowJo software v10.5.3 (TreeStar, Ashland, Oregon, USA) were used to analyze the data ($APC^+$ cell populations). Based on the percentage of B cells in the cell population, we calculated the concentration of B cells per ul blood.

***Xenogeneic models in SCID-Beige mice (CRS model)***

On day 0, $3x10^6$ Raji cells were intraperitoneally injected into 6- to 8-week-old female C.B-*Igh*-1b/GbmsTac-*Prkdc*$^{scid}$-*Lyst*$^{bg}$ N7 mice (Taconic Biosciences, New York, USA). After 3 weeks, mice were divided into three groups: one group was injected

intraperitoneally with 3 x $10^7$ hWT CAR-expressing CD8 T-cells, while another group was injected with 3 x $10^7$ hLiCAR-expressing CD8 T-cells. The control group received PBS only. For 3 days after that, LiCAR-transferred mice were subjected to pulsed near-infrared light treatment (980 nm at a power density of 250 mW/$cm^2$; pulse: 20 sec ON, 5 minutes OFF for 2 hours a day). All the mice were weighed every day to evaluate the weight change. On day 0 and day 3, blood cells were collected from the retro-orbital sinus by glass capillary or by tail-clip from anesthetized mice. Blood was left to clot for 30 min at room temperature and then centrifuged 6000 x g at 4$^o$C for 10 min. Serum was collected and kept frozen at -80$^o$C until analysis. mIL-6 in the serum was detected using ELISA (#KMC0061, Invitrogen) following the manufacturer's instructions.

***Element analysis of the UCNP distribution in mouse tissues***

Element mapping was performed in the Electron Microscopy Facility at the University of Massachusetts Medical School. Dissected mouse tissues were fixed by immersion in 4% paraformaldehyde for 2 days at 4 $^o$C and then kept frozen. After thawing the tissues, a second fixation was performed with 2.5% glutaraldehyde in 0.1.M Na Cacodylate buffer (ph 7.2) for 30 min at room temperature. The fixed samples were then washed three times in the same fixation buffer. Following the third wash, the samples were dehydrated through a graded series of ethanol (10, 30, 50, 70, 85, 95% for 20 min each) to three changes of 100% ethanol, and then they underwent critical point drying in liquid $CO_2$. The dried mouse tissues were then cut to expose the inside, and they were mounted onto aluminum stubs with carbon tape making sure that the exposed surfaces were facing up. All the samples were then carbon coated with 3 nm of

carbon to ensure conductivity. The specimens were examined using an FEI Quanta 200 FEG MK II scanning electron microscope at 15 Kv accelerating voltage under two modalities, secondary electron and backscattered imaging. The samples were also examined using an EDS system (Oxford Link Inca 350 x-ray spectrometer) to determine the element distributions in the tissues. The element spectrum, element mapping, and atomic ratio of each element were presented as the raw data obtained in the INCA EDS system without further manipulation.

***Cytotoxicity of UCNPs***

*Cell culture:* B16-OVA-hCD19 cells were cultured in Dulbecco's modified Eagle's medium (DMEM) containing 10% fetal bovine serum (FBS), 100 μg $mL^{-1}$ streptomycin and 100 U $mL^{-1}$ penicillin at 37 °C in a humidified incubator containing 5% CO2 and 95% air. The medium was replenished every other day and the cells were subcultured after reaching confluence.

*Cell viability assay:* Cell viability was verified by MTT assay. B16-OVA-hCD19 cells were plated in a 96-well plate. After 12 h, the nanoparticles were added at different concentrations (0, 20, 40, 60, 80, 100 μg $mL^{-1}$). The cells were incubated another 24 h under 5 % CO2 at 37°C. MTT solution (5.0 mg $mL^{-1}$, 50 μL) was added to every well and left for 4 h. The old cell culture medium was removed carefully and 200 μL DMSO was added to every well. A microplate reader (Bio-Rad) was used to record the absorption at 595 nm. Cell viability (%) = OD value test/OD value control × 100 %.

***In vivo assesment of UCNP toxicity***

*Pathological sectioning to evaluate the toxicity of UCNPs to major organs:* On the 1st, 7th and 14th day after injection of UCNPs (1mg $mL^{-1}$, 150 μL), mice were sacrificed and major organs (heart, liver, spleen, lung, kidney, and tumor) were dissected for H&E staining. Mice injected with 150μL PBS were used as the control.

*Blood biochemistry and complete blood panel analysis:* The mice were injected with UCNPs (1mg $mL^{-1}$, 150 μL) and then sacrificed at various time points (1, 7, and 14 days) after injection. Mice injected with 150 μL PBS were used as the control. Before the mice were euthanatized, blood samples (~ 0.5 mL) were collected for blood panel analyses and blood chemistry tests.

***Macrophage assay of UCNP-injected mice***

The mice were injected with UCNPs (1mg $mL^{-1}$, 150 μL) and then sacrificed 14 days after injection.

*Flow cytometry assay of the macrophage cells in the tumor:* Tumors were isolated from mice. Tumor tissue was divided into small pieces, treated with 1 mg $ml^{-1}$ collagenase I (Gibco) for 1 h at 37 $^{o}$C and ground using the rubber end of a syringe (BD, 10 mL syringe). Cells were filtered through nylon mesh filters (Corning, cell strainer, 70 μm nylon). The single cells were collected by centrifugation (800 × g, 5 min), blood cells in the tumor tissue were eliminated by cold $NH_4Cl$ lysis. The tumor single cell suspensions were washed in cold PBS containing 2 % FBS. The tumor cells were stained with fluorescence-labeled antibodies FITC-anti-F4/80 (total macrophages) and APC-anti-CD86 (M1 macrophages) following the manufacturer's instructions. All

antibodies were diluted 200 times. Flow cytometric analyses were performed on an LSRFortessa (BD Biosciences) and analyzed using FlowJo Software (Tree Star).

*Flow cytometry assessment of spleen immune cells:* Spleens were isolated from mice after different treatments. We ground the spleen and cells were filtered by nylon mesh filters. The blood cells were lysed by two immersions in $NH_4Cl$ solution, and then washed in cold PBS containing 2% FBS. The spleen cells were stained with fluorescence-labeled antibodies FITC-anti-F4/80 (total macrophages), APC-anti-CD86 (M1 macrophages), or PE/Cy7-anti-CD206 (M2 macrophages) following the manufacturer's instructions. All antibodies were diluted 1:200. Flow cytometric analyses were performed on an LSRFortessa (BD Biosciences) and analyzed using FlowJo Software (Tree Star).

***In vivo study of UCNP stability***

150 μL UCNPs (1mg $mL^{-1}$) were injected into mouse tumors or muscle. On the 1st, 7th, 14th and 28th day after UCNP injection, mice were sacrificed, and the UCNP-injected tumor or muscle was isolated and fixed with 4% paraformaldehyde (PFA)/0.25% glutaraldehyde in 0.1 M sodium phosphate buffer (PB) overnight. After several washes in 0.1M cacodylate buffer (pH7.4), sections were postfixed with 1% osmium tetroxide (Sigma) in 0.1 M cacodylate buffer for 1 h. After six washes with water for 1 h each, samples underwent dehydration through a graded ethanol series of 10%, 30%, 50%, 70%, 85%, 95% and 100% EtOH (10 min each for 10%-70%, 20 min each for 85%, 30 min each for 95% and 100% (three times)). UCNP-injected tumor or muscle was treated with propylene oxide for 10 min twice and then immersed in freshly

prepared 50% (v/v) Durcupan resin in propylene oxide overnight for resin infiltration (Sigma). UCNP-injected tumor or muscle was then immersed in freshly prepared Durcupan resin for six times, 1 hour each. Sections were then transferred to freshly prepared Durcupan resin contained in a tube and left in a 60°C oven for 2 days for resin curing. The UCNP-injected tumor/muscle was excised out from the flat-embedded sections and glued onto a resin block for ultrathin sectioning. 70 nm ultrathin sections were cut with a diamond knife (Diatome), collected in a formvar-coated single-slot copper grid and briefly counterstained with 2% uranyl acetate in 50% ethanol and 0.4 % lead citrate. Sections were observed under electron microscope (Philips CM10 Electron Microscope) at 100 KeV accelerating voltage. The above sample preparation and imaging were performed in the Electron Microscopy Facility at the University of Massachusetts Medical School.

***Data and statistical analysis***

All the data collected were plotted by GraphPad Prism version 8.0.0 as mean ± s.e.m unless otherwise noted. The statistical significance was assessed by using two-tailed Student's t-test. *$*P<0.05; **P<0.01; ***P<0.001$*. The half-lives of activation and deactivation kinetics were calculated by the same statistical software.

## Results

### *Design and optimization of LiCARs.*

In our envisioned design, LiCARs were engineered by intracellularly splitting the functional domains of a CAR and installing photo-responsive modules into each half of a split CAR (**Fig. 11**). T cell activation would then only occur after the functional assembly of the two components of the split CAR in the presence of blue light, thus conferring on-off spatiotemporal control over the anti-tumor immune response. To test our idea, we set out to design a series of candidate receptors for light-dependent assembly of functional CARs (A+B or C+D combinations (**Fig. 12a-b**). Two optical dimerizers with different activation and deactivation kinetics were tested. The first pair was composed of the photolyase homology domain of *Arabidopsis thaliana* cryptochrome 2 (CRY2) and the N-terminal region of its photo-sensitive binding partner CIB1 (the CRY2/CIBN pair)[47]

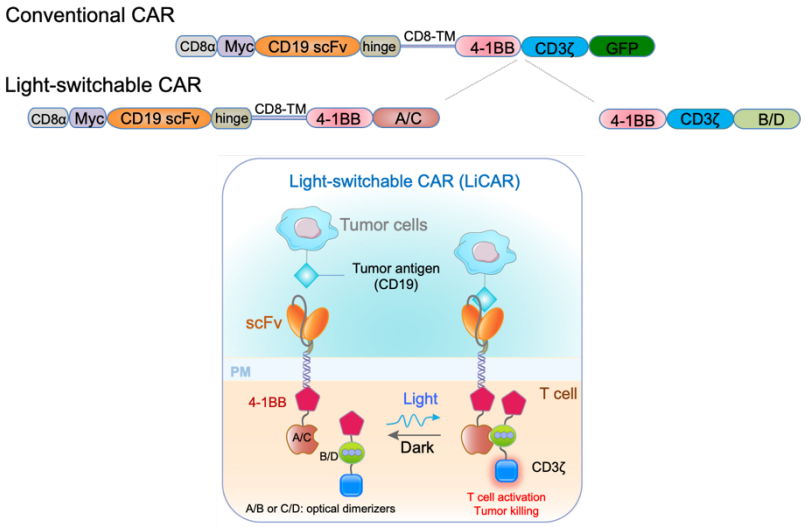


**Figure 11: Design of LiCAR for light-inducible assembly of functional chimeric antigen receptors (CARs).**
Design of photoactivatable CARs that are dually gated by tumor antigen (CD19) and light. Engineered CAR T-cells can only be switched on in the presence of light when engaged with cognate tumor cells.

**(Fig. 3a)**. The second system was termed iLID, in which a bacterial peptide ssrA was fused to the C-terminus of *Avena sativa* light-oxygen-voltage domain 2 (LOV2) and exhibited light-dependent interaction with its binding partner sspB (the LOV2-ssrA/sspB pair)[46] **(Fig. 3b)**. Based on these elementary building blocks, we generated a series of hybrid constructs by fusing optical dimerizers with either the extracellular antigen-binding modules or the intracellular signal transduction modules from a conventional CAR (**Fig. 12a**). In a typical design, Component I of LiCAR shares several similar features with CAR, which bears a signal peptide from the T cell surface glycoprotein

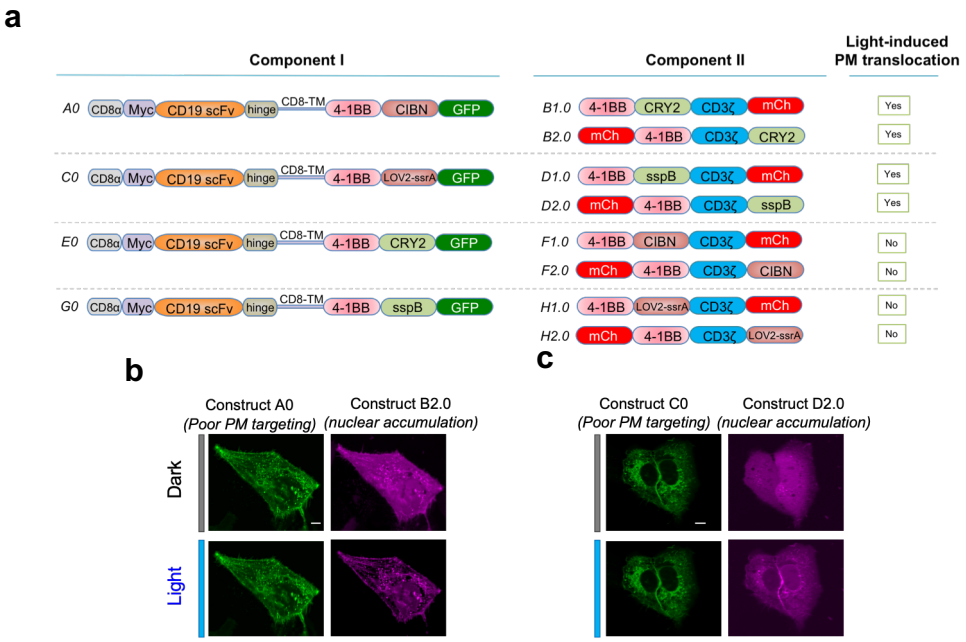


**Figure 12: Design and screening of CRY2- and LOV2-based LiCARs.**
(**a**) Constructs used to screen and optimize the design of LiCARs (Components I+II). **(b-c)** Representative confocal images of HeLa cells expressing the indicated components before and after light illumination. Scale bar, 5 μm.

CD8 alpha chain, a Myc tag to aid extracellular staining, an anti-CD19 scFv, CD8α hinge, the CD8 transmembrane domain, the co-stimulatory 4-1BB domain, and one part

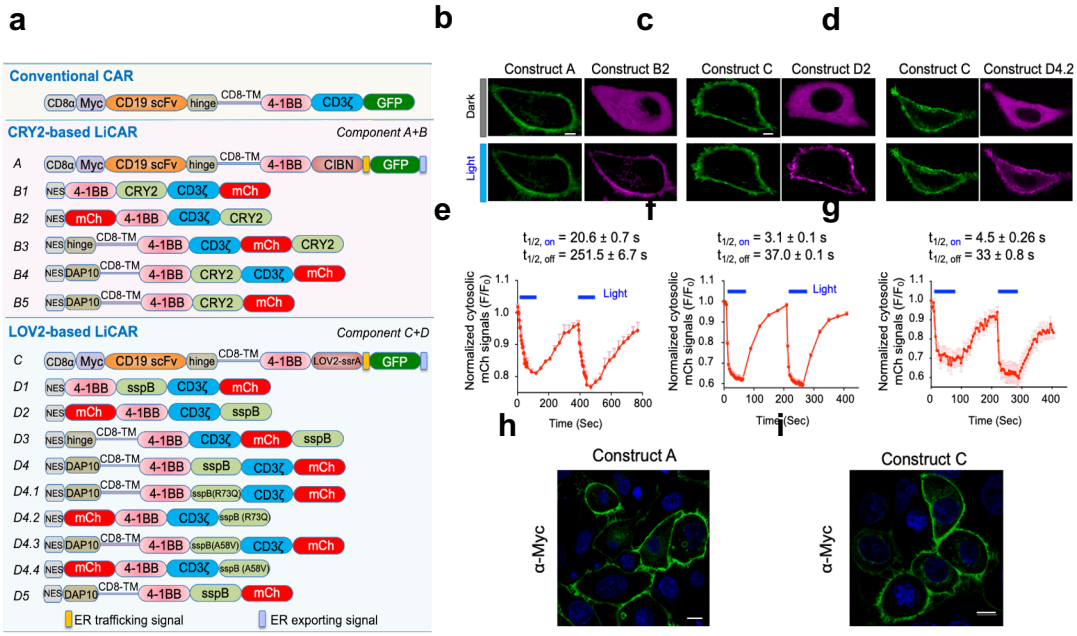


**Figure 13**: **Optimized constructs of LiCAR.**
(**a**) Optimized constructs used in the study. Modular domains within a typical CAR were split into two polypeptides (constructs A+B or C+D), the functional assembly of which can only be achieved upon light-induced interaction using two optical dimerizers (CRY2/CIBN or LOV2-ssrA/sspB pairs). (**b-d**) Representative confocal images showing reversible recruitment of cytosolic Construct B or D (mCherry-tagged; magenta) toward the PM-resident Construct A (GFP-tagged; green, b) or Construct C (c-d) in response to two dark-light cycles (40 mW/cm$^2$; 470 nm) in Hela cells. (**e-g**) The activation and deactivation kinetics are shown below the images. n = 4 (panel e); n = 36 (panel f); n = 11 (panel g, mean ± s.e.m.). Scale bar, 5 μm. (**h-i**) The confocal images of HeLa cells expressing the PM-embedded constructs A or C (without fluorescence tag) after non-permeabilized immunostaining with an anti-Myc antibody.

of the optical dimerizer pair. GFP was tagged to the C-terminus to aid visualization and detection of protein expression. The prototypical Component II construct comprised a co-stimulatory 4-1BB domain, the T cell activating ITAM fragment of the CD3ζ subunit, and the complementary part of the optical dimerizer pair, as well as the mCherry (mCh) tag to aid in visualization and flow cytometry analysis of protein expression.

By using HeLa cells as a model cellular system, we first examined the subcellular distribution of the designed constructs. We found that Component I showed poor trafficking toward the plasma membrane (PM), whereas Component II tended to accumulate within the nucleus (A0+B2.0 or C0+D2.0; **Fig. 12**). To overcome these issues, we inserted ER trafficking and export signal peptides, derived from an inward rectifier potassium channel[101,102], into Component I to enhance PM targeting. In parallel, we appended a nuclear export signal (NES) from a cyclical AMP-dependent protein kinase inhibitor (PKIα)[103] into Component II in order to minimize its nuclear entry (**Fig. 13a-c**). When co-expressed in mammalian cells, in response to blue light illumination, these improved constructs (A+B2 or C+D2) exhibited light-dependent heteromerization, as reflected by the rapid cytosol-to-PM translocation of Component II (**Fig. 13b-d**). This process can be repeated multiple times by toggling the light switch (**Fig. 13e-g**). While the dissociation of the LOV2-based LiCAR complex occurred with a relatively fast half-life ($t_{1/2,\ off}$= 37 s) **(Fig. 13f)**, the reversion of CRY2-CIBN1 binding took a much longer time ($t_{1/2,\ off}$ = 4-5 min) **(Fig. 13e)**. The varying range of deactivation half-lives makes it possible to temporally control the duration of the elicited anti-tumor immune response. The cell surface expression and membrane topology of Component I was confirmed by the non-permeabilized staining of the transfected cells with an anti-Myc antibody (**Fig. 13h-i**)

### *LiCAR allows for photo-tunable and antigen-specific activation of engineered T cells*

We next sought to screen combinations that would permit the light-induced functional assembly of LiCARs in T cells. We used the NFAT-dependent luciferase

(NFAT-Luc) reporter assay as a convenient method to assess the degree of T cell activation[15]. In human Jurkat-Luc T cells co-transduced with retroviruses encoding the split CAR components, we were able to achieve a transduction efficiency of 70-80% for the CRY2-based LiCAR (A+B) and over 97% for the LOV2-based LiCAR (C+D; GFP as indicator for Component I and mCherry for Component II; **Fig. 14a**). The co-expression

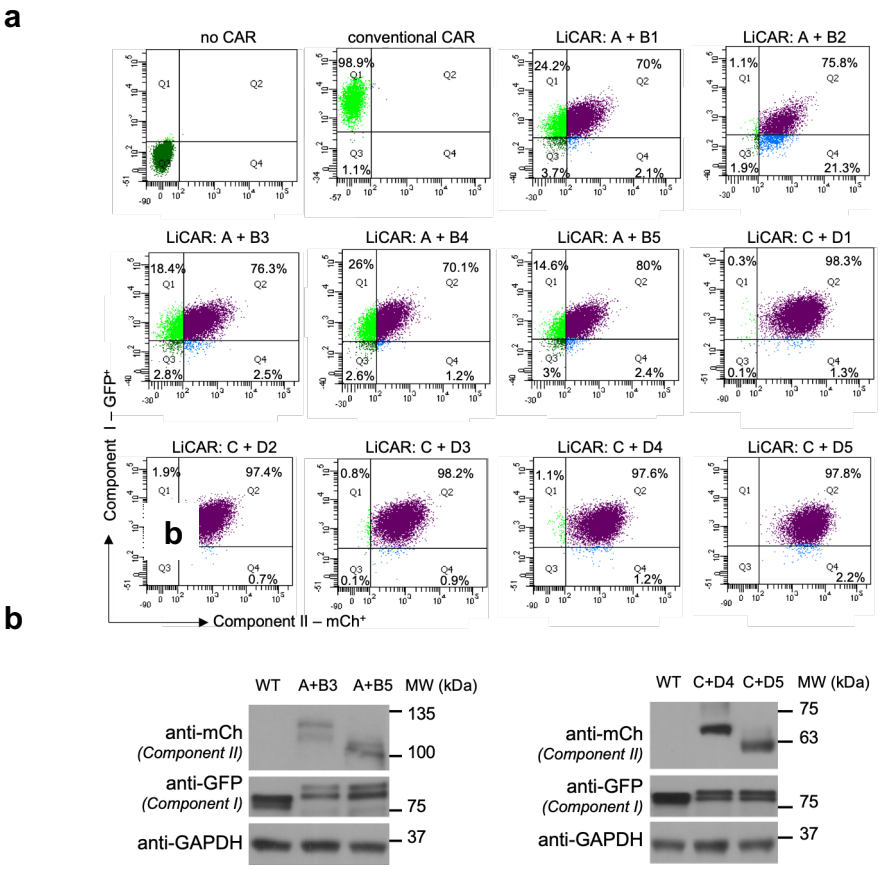


**Figure 14**: **Expression of engineered CAR components (A+B or C+D combinations) in human Jurkat T cells.**
(**a**) Quantification of transduction efficiency in human Jurkat T cells. Jurkat cells were retrovirally transduced with the indicated A+B or C+D combinations to assemble functional LiCARs. The expression of A/C ($GFP^+$) or B/D ($mCherry^+$) components was determined by flow cytometry. (**b**) Immunoblot analysis of LiCAR component expression in Jurkat T cells. T cells were transduced with retroviruses encoding GFP-tagged WT CAR or LiCAR components (A-GFP + B-mCherry; or C-GFP + D-mCherry). Component I was probed with an anti-GFP antibody whereas Component II was probed with an anti-mCh antibody. GAPDH was used as a loading control.

of both components at the protein level in T cells was further confirmed by immunoblotting (**Fig. 14b**). NFAT-Luc Jurkat T cells expressing engineered receptors were then engaged with CD19-negative K562 leukemia cells or CD19-positive Raji lymphoma cells (**Fig. 15a-c**). In the dual presence of cognate tumor antigen ($CD19^+$ Raji cells) and light stimulation, we detected a pronounced increase in NFAT reporter bioluminescence, indicating the antigen/light-dependent activation of engineered T cells (A+B1, A+B2, C+D1, or C+D2; **Fig. 16**). However, these prototypical LiCAR T-cells did

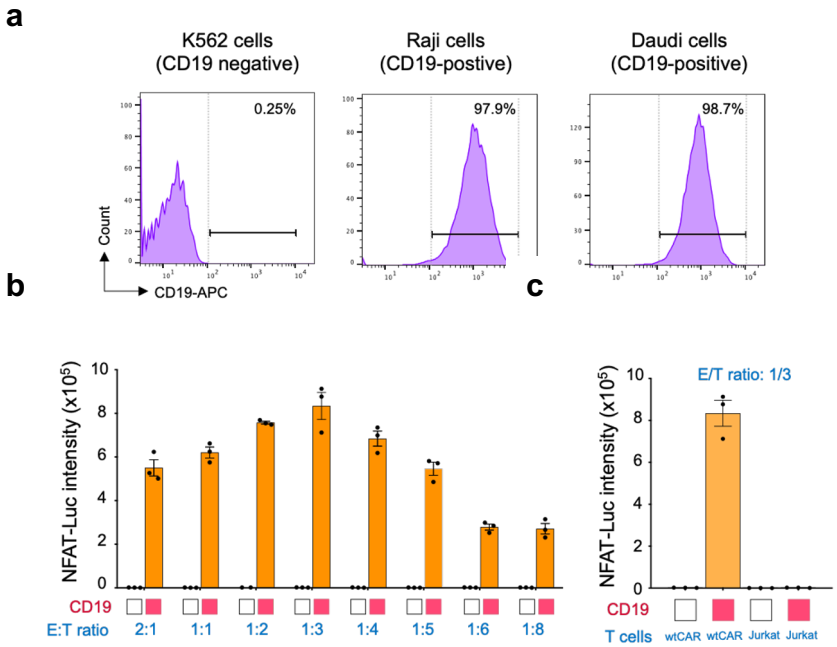


**Figure 15: Optimizing the ratio of effector T cells to target tumor cells (E/T ratio) to evaluate the function of engineered CAR T-cells.** (**a**) Quantification of CD19 expression in target B cells. K562 cells showed negligible CD19 expression whereas Raji or Daudi lymphoma cells showed over 98% positive staining for CD19. (**b**) NFAT-Luc activity of conventional CAR T-cells when co-cultured with different amounts of either $CD19^-$ K562 cells (open box) or $CD19^+$ Raji cells (red box). An E/T ratio of 1:3 was able to elicit the highest NFAT-dependent activity. n = 3 (mean ± s.e.m.). (**c**) NFAT-Luc activity of WT CAR T-cells incubated with Raji cells at a ratio of 1:3 compared with that of non-transduced (negative control) T cells. n = 3 (mean ± s.e.m.).

not appear to be efficiently activated, as they only produced 16-21% of the maximal response seen in WT CAR T-cells (**Fig. 16**). We reasoned that targeting both components to the PM might reduce the entropic cost of driving the cytosolic Component II to couple with the PM-resident Component I. Therefore, we continued to modify Component II by adding the transmembrane domain of CD8 (Constructs B3 or D3) and/or the homodimeric DAP10 ectodomain (B4 or D4)[104,105], the latter of which was added to double the available numbers of CD3ζ-ITAMs in each assembled LiCAR complex in order to amplify the activation signals[106]. We also reordered the positions of intracellular CAR components and optical dimerization modules, anticipating that we would be able to identify the best configuration for maximal light-inducible reconstitution of functional CARs (**Fig. 13a)**. Ultimately, we identified the best combinations for both

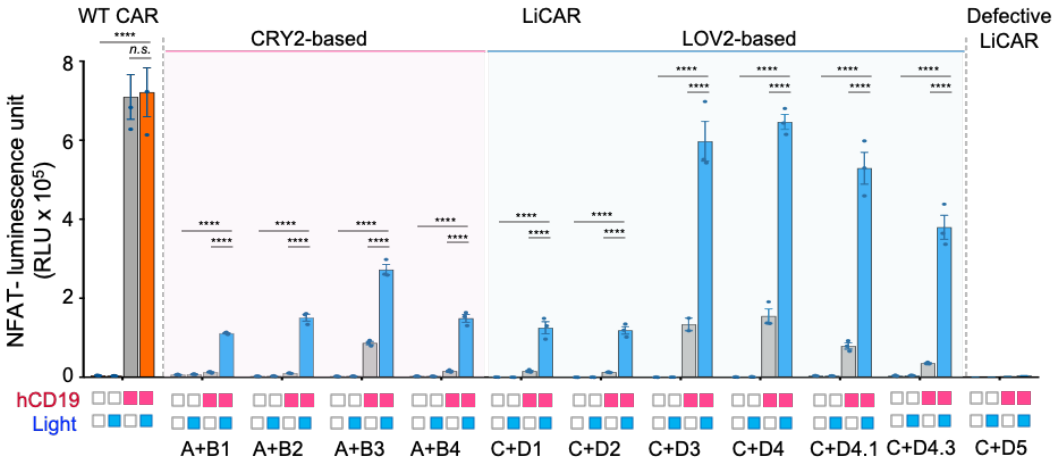


**Figure 16: Quantification of NFAT-dependent luciferase (NFAT-Luc) reporter activity in Jurkat T cells.**
CAR, LiCAR, or defective LiCAR-transduced T cells engaged tumor cells bearing noncognate (open box; CD19-negative K562 cells) or cognate antigens (red box; $CD19^{+}$ Raji cells) under dark (open box) or lit conditions (blue box). Defective LiCAR lacking the CD3ζ-ITAM domain was used as negative control. n = 3 (mean ± s.e.m.). ****$P$ < 0.0001 compared to the dark group; *n.s.*, not significant (two-tailed Student's *t*-test).

CRY2- and LOV2-based LiCARs, which led to 39% (A+B3) and 93% (C+D4; **Fig. 16**) of the maximal response in the NFAT-Luc assay, respectively. As a stringent control, defective LiCAR T-cells (C+D5) lacking CD3ζ-ITAM in Component II did not show discernible antigen/light-dependent changes (right, **Fig. 16**).

Nevertheless, these improved LiCAR T-cells (A+B3 or C+D4) displayed appreciable dark activity (i.e., pre-activation of NFAT-Luc in the dark; **Figs. 16, 17a**). This is probably due to two reasons: (i) the relatively strong binding affinity of iLiD-sspB ($K_d$: 4.7 ± 0.7 μM (dark) vs 0.132 ± 0.005 μM (lit))[46]; (ii) the highly sensitive nature of the synthetic NFAT-Luc reporter, which bears multiple copies of NFAT response elements in the promoter. We therefore explored two additional weaker versions of iLID in which wild type sspB was mutated to sspB R73Q ($K_d$: 47 ± 13 μM (dark) vs 0.8 ± 0.1 μM (lit))[46] **(Figs. 13a, 13d, 13g)**, or sspB A58V ($K_d$: 56 ± 6 μM (lit))[107] **(Fig. 13a)** and found that the use of sspB (R73Q) or sspB (A58V) led to a substantial reduction of background activation but also reduced the light activity to 71% (C+D4.1) and 51% (C+D4.3) of the maximal response in the NFAT-Luc assay, respectively **(Fig. 16**). We next examined the antigen/light-dependent expression of IL-2 – a naturally existing NFAT target gene – as a stringent and more physiologically relevant readout in T cells (**Fig. 17c**). In both the NFAT-Luc reporter assay and the IL-2 ELISA assay, LiCAR T-cells exhibited light-tunable activation of NFAT-dependent activity (**Fig. 17b-c**). Most importantly, we did not detect the pre-activation of IL-2 production in the dark for all the combinations of both CRY2- and LOV2-based LiCARs (**Fig. 17c**). Collectively, these data established the feasibility of using light to fine-tune the dosage of T cell activity.

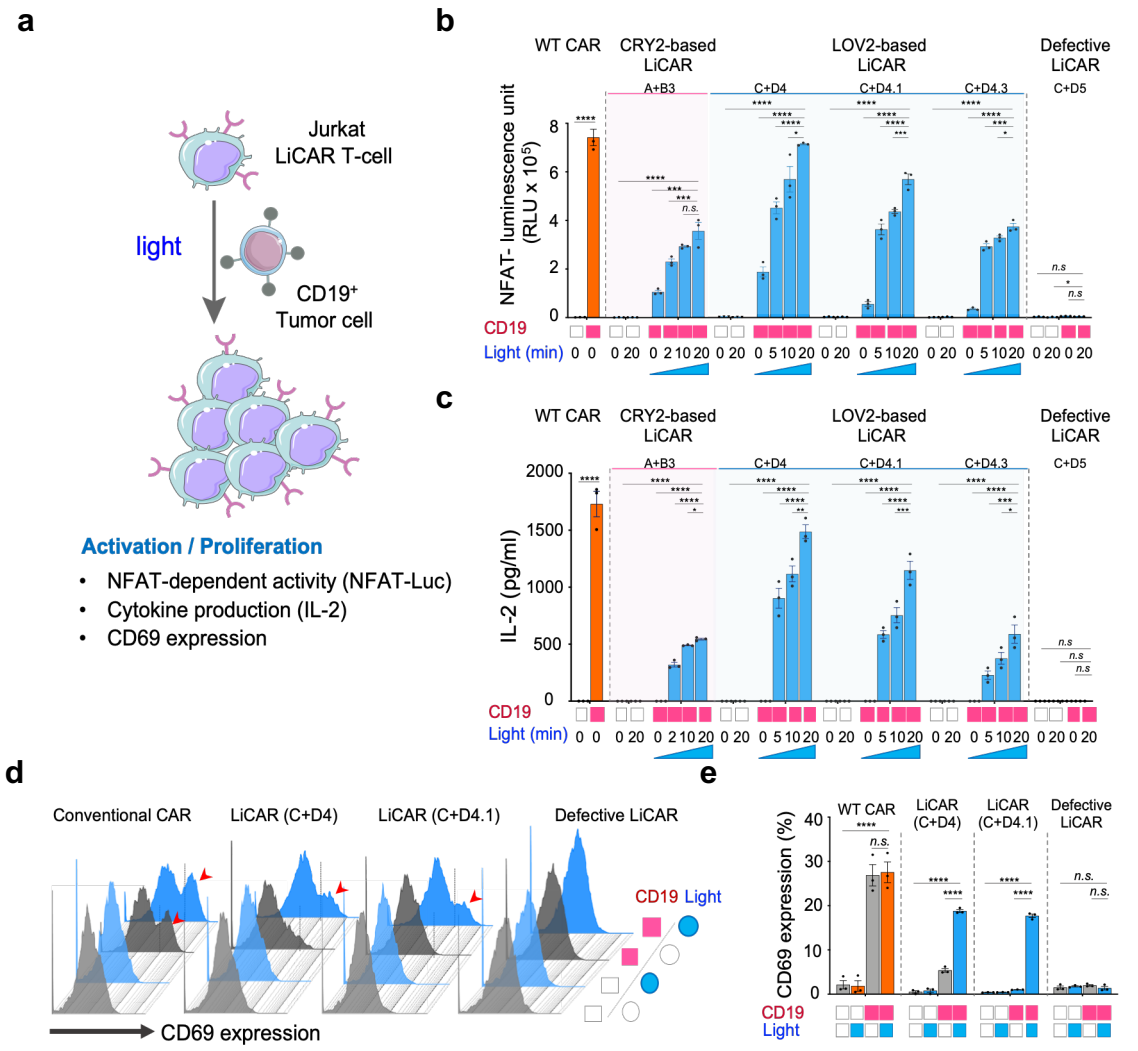


**Figure 17: Photo-tunable immune response enabled by LiCAR T-cells.** (**a**) Human Jurkat T cells were virally transduced to express WT CAR, LiCARs, or defective LiCAR, followed by functional assays to determine their therapeutic responses. (**b-c**) Light-tunable responses of engineered CAR T-cells examined by (b) photo-inducible NFAT-dependent luciferase reporter activity and (c) IL-2 production in Jurkat T cells. n = 3 (mean ± s.e.m.). ON time of constant photostimulation was indicated at the bottom. **P* < 0.05; ***P* < 0.01; ****P* < 0.001; *****P* < 0.0001 compared to the dark group or the lit groups; *n.s.*, not significant (two-tailed Student's *t*-test). (**d-e**) Determination of early T cell activation as reflected by upregulated CD69 expression on cell surface. Jurkat T cells transduced with conventional CAR, defective LiCAR, and LiCAR were engaged with $CD19^+$ Daudi or $CD19^-$ K562 cells under dark or lit conditions. n = 3 (mean ± s.e.m.). *n = 3* (mean ± s.e.m.). *****P* < 0.0001 compared to dark group; *n.s.*, not significant (two-tailed Student's *t*-test).

Notably, the LOV2-based LiCAR seemed superior to the rival CRY2-based version by photo-triggering T cell activation to an extent comparable to WT CAR T-cells (**Fig. 17b-c**). We, therefore, focused on the C+D4 or C+D4.1 combination for further functional characterization. Following T cell activation, we set out to evaluate an early event indicative of T cell activity by monitoring CD69 expression in Jurkat T cells (**Fig. 17d-e**). CD69 is up-regulated within 2-4 hours after T cell activation and is reported to

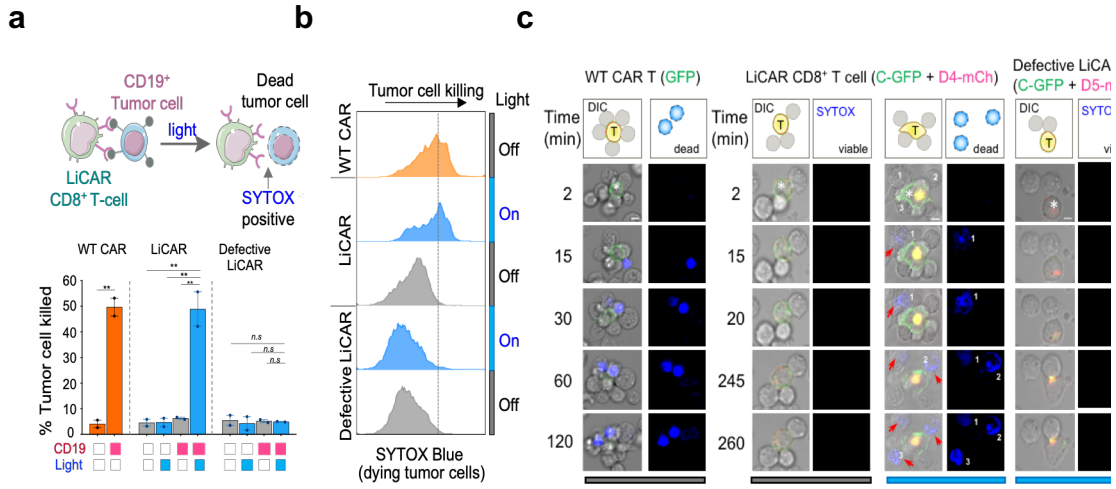


**Figure 18: LiCAR human CD8⁺ T-cells enable photo-inducible killing of human tumor cells *ex vivo*.**

(**a**) Primary CD8⁺ T cells isolated from the peripheral blood of healthy donors were transduced to express WT CAR, LiCAR, or defective LiCAR, followed by functional assays (SYTOX Blue dead cell staining) to determine the tumor cell killing efficacy. The tumor killing results, quantified by SYTOX staining, are shown in the bar graph below the cartoon. n = 2 (mean ± range). $^{**}P < 0.01$ compared to dark group; *n.s.*, not significant (two-tailed Student's *t*-test). (**b-c**) Light-induced tumor cell killing assessed by flow cytometry (b) and time-lapse confocal imaging (c). Transduced human CD8⁺ T cells were engaged with CD19⁻ K562 or CD19⁺ Daudi lymphoma cells and kept in the dark or exposed to blue light. SYTOX blue was used to stain dying tumor cells with compromised plasma membranes. Shown in panel c are overlaid images of WT CAR, LiCAR, or defective LiCAR-expressing human CD8⁺ T cells (green, C-GFP; red, D4-mCherry) engaged with Daudi cells (indicated by numbers). Red arrowheads, dying Daudi cells with positive SYTOX blue staining. Cells were either kept in the dark or exposed to blue light illumination (470 nm; 40 mW/cm$^2$; 5 h). Scale bar, 5 µm.

be essential for lymphocyte retention in lymphoid organs[108]. We compared the CD69 expression level in engineered Jurkat T cells that were engaged with either $CD19^-$ or $CD19^+$ tumor cells, before and after photo-stimulation. While conventional CAR T-cells only required the cognate CD19 antigen to activate T cells and boost CD69 expression, engineered T cells expressing LiCAR showed a light-dependent increase in CD69 expression in the presence of $CD19^+$ tumor cells, including Daudi (**Fig. 17d**). The (C+D4.1) combination showed a lower background activity in the dark compared to (C+D4) (**Fig. 17d-e**). By contrast, $CD19^-$ K562 cells did not induce any significant change in CD69 expression in either the dark or lit state. Taken together, these results validated the successful construction of LiCAR to achieve dual input-gated control of T cell activation in a photo-tunable manner.

***LiCAR T-cells enable photo-inducible killing of tumor cells ex vivo***

A hallmark of CAR T-cells is their ability to induce apoptosis in targeted tumor cells. Controlled activation of CAR T-cells to trigger inducible cytotoxicity against tumors is one of the most desirable features of smart immunotherapy. Hence, we moved on to test the LiCAR's ability to mediate the killing of cognate tumor cells (e.g., Daudi cells derived from Burkitt's lymphoma) when expressed in primary human $CD8^+$ cytotoxic T cells (**Fig. 18**). Both components of LiCAR were co-expressed in $CD8^+$ T cells derived from peripheral blood mononuclear cells (PBMC), as confirmed by flow cytometry analysis and confocal imaging (**Fig. 19**). Subsequently, the cytotoxic activity of engineered $CD8^+$ T cells against co-cultured K562 ($CD19^-$) or Daudi ($CD19^+$) cancer cells was quantified by staining target cells with the SYTOX Blue dye, which only

penetrates dead cells with a compromised plasma membrane. After overnight

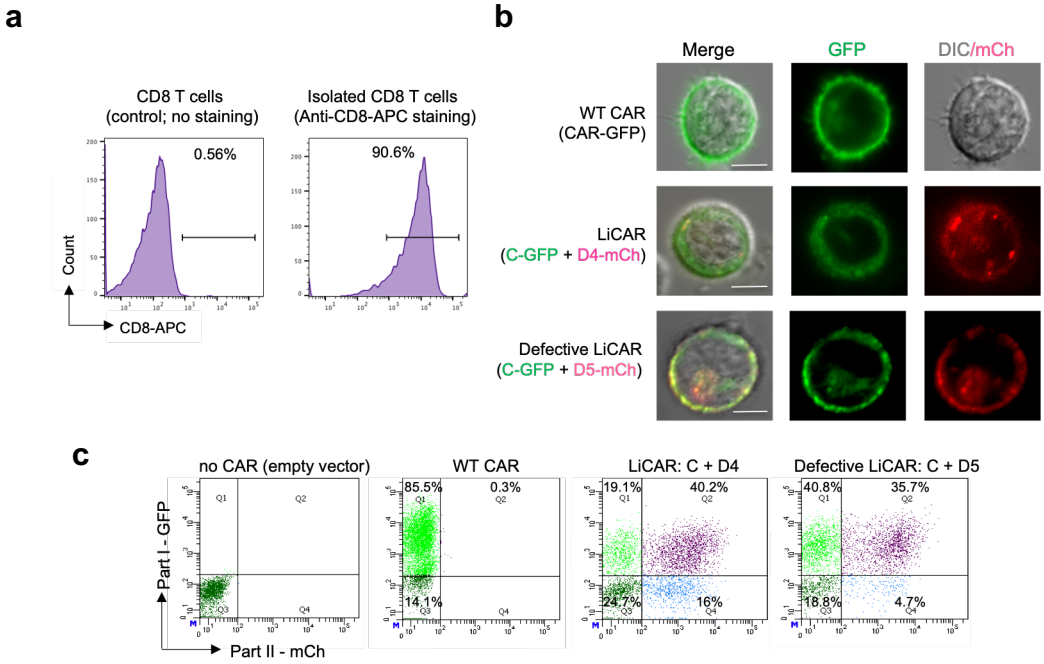


**Figure 19: Expression of engineered CARs in human primary CD8⁺ T cells.** (**a**) Evaluation of the purity of CD8⁺ T cells isolated from PBMCs of healthy donors. Isolated T cells were stained with anti-CD8-APC. Non-stained CD8⁺ T cells were used as negative controls to aid the gating of cell populations. (**b**) Representative confocal images of human CD8⁺ T-cells transduced with WT CAR (green, top panel) or the indicated CAR components (C-GFP, green; or D4/D5-mCherry, red; middle and bottom panels). (**c**) Quantification of WT CAR (GFP-tagged), LiCAR (C-GFP + D4-mCh) or defective LiCAR (C-GFP + D5-mCh) expression in human CD8⁺ T cells. GFP-positive (for the WT CAR group) or double positive cells (for the LiCAR and the defective LiCAR groups) were used for functional assays.

incubation in the presence of pulsed blue light illumination, we observed a light-dependent boost of tumor cell killing, as reflected in the rightward shift of the SYTOX Blue staining peak in the flow cytometric histograms (**Fig. 18b**). The degree of targeted tumor cell killing was comparable to that observed with WT CAR T-cells. As a stringent control, the killing of cognate tumor cells was not observed in the defective LiCAR group (**Fig. 18**). Noncognate tumor cells (CD19⁻ K562 cells) survived throughout the assay,

regardless of the presence of light. This attests to the strict tumor antigen specificity of the designed LiCAR T-cells.

To better visualize the spatiotemporal features of CD8$^+$ LiCAR T-cell mediated killing in response to light illumination, we performed time-lapse confocal imaging of LiCAR T-

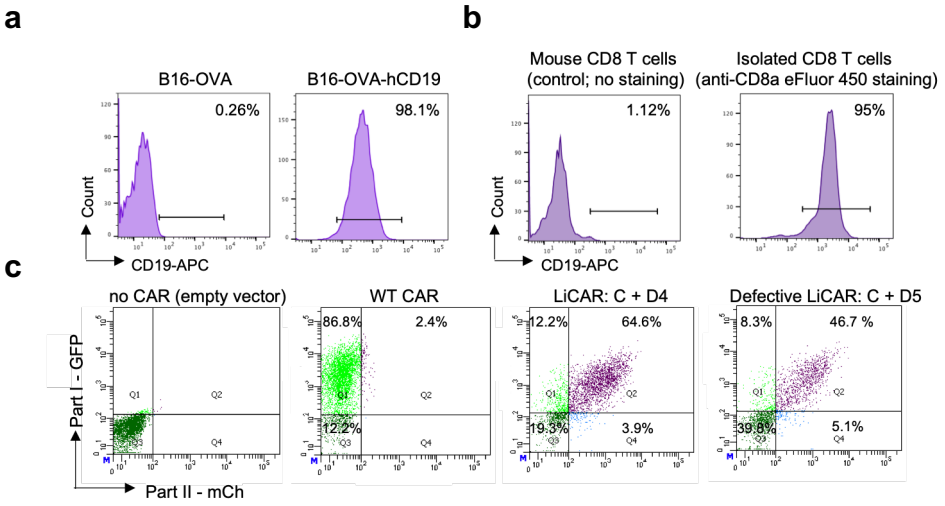


**Figure 20: Expression of engineered CARs in mouse primary CD8$^+$ T cells.** (**a**) Quantification of CD19 expression in melanoma cells (B16-OVA) and melanoma cells exogenously expressing human CD19 (B16-OVA-hCD19). (**b**) Evaluation of the purity of CD8$^+$ T cells isolated from mouse spleens. Isolated T cells were stained with an anti-mouse CD8a eFluor 450 antibody. Non-stained CD8$^+$ T cells were used as negative control to aid the gating. (**c**) Quantification of WT CAR (GFP-tagged), LiCAR (C-GFP + D4-mCh) or defective LiCAR (C-GFP + D5-mCh) expression in transduced mouse CD8$^+$ T cells. GFP-positive (for the WT CAR group) or double positive cells (for the LiCAR and the defective LiCAR groups) were used for functional assays.

cells mixed with CD19$^+$ Daudi cells (**Fig. 18c**). Engineered CD8$^+$ T cells expressing WT CAR or defective LiCAR were used as positive and negative controls, respectively. Again, SYTOX blue dye was added to monitor dying cells with a compromised plasma membrane. Within 15 minutes of exposure to blue light, we started to observe the

appearance of blue staining in Daudi cells engaged with LiCAR-expressing CD8⁺ T cells but not in those with defective LiCAR T-cells. Collectively, LiCAR T-cells were able to

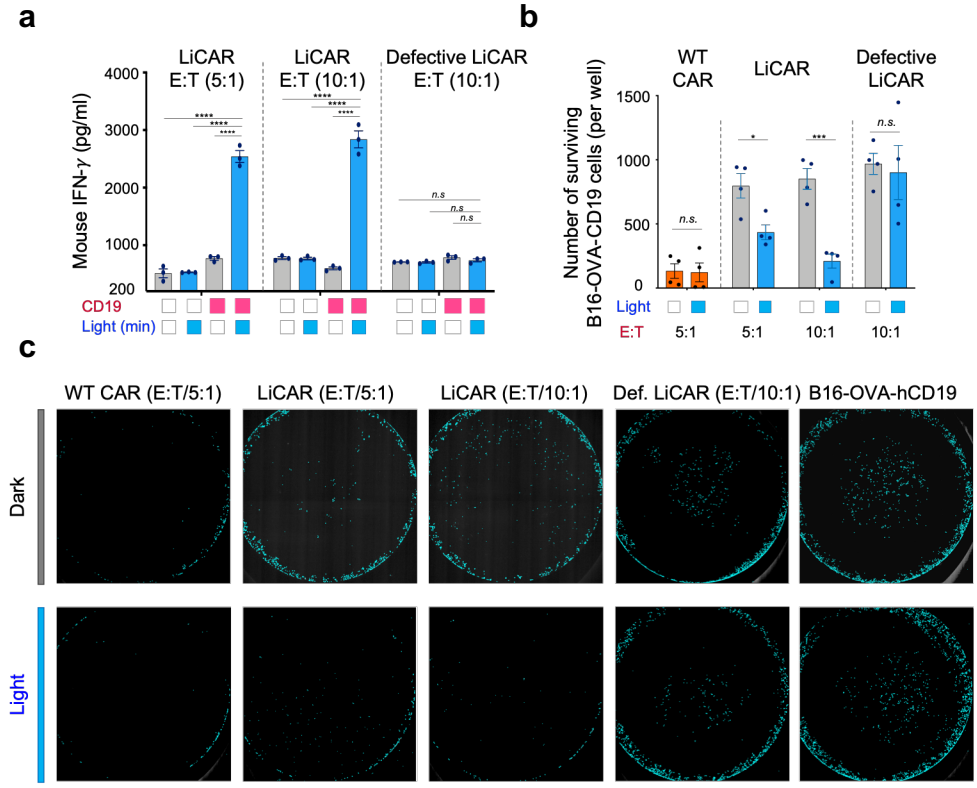


**Figure 21: LiCAR mouse CD8⁺ T-cells enable photo-inducible killing of mouse tumor cells *ex vivo*.**

(**a**) Quantification of IFN-γ produced by engineered mouse CD8⁺ T cells expressing LiCAR or defective LiCAR after co-culturing with melanoma cells (B16-OVA cells expressing human CD19 [B16-OVA-hCD19] or B16-OVA [as control]) at different effector: target (E:T) ratios. n = 3 (mean ± s.e.m.). ****$P$ < 0.0001 compared to the dark group; *n.s.*, not significant (two-tailed Student's *t*-test). (**b**) B16-OVA-hCD19 cell killing efficacy of mouse CD8⁺ T cells expressing WT CAR, LiCAR, or defective LiCAR at the indicated effector: target (E:T) ratios. n = 4 (mean ± s.e.m.). *$P$ < 0.05; ***$P$ < 0.001 compared to the dark group; *n.s.*, not significant (two-tailed Student's *t*-test). (**c**) Quantification of WT CAR (GFP-tagged), LiCAR (C-GFP + D4-mCh) or defective LiCAR (C-GFP + D5-mCh) expression in transduced mouse CD8⁺ T cells. GFP-positive (for the WT CAR group) or double positive cells (for the LiCAR and the defective LiCAR groups) were used for functional assays.

inducibly mount anti-tumor cytotoxicity toward cognate target cells in the dual presence of tumor antigen and light *ex vivo*.

Next, we performed similar *ex vivo* co-culture experiments to examine whether engineered $CD8^+$ T cells derived from mice would likewise trigger productive immune responses and evoke cytotoxicity against cancer cells upon blue light stimulation. To test this, we resorted to a mouse B16-OVA melanoma cell line stably expressing human CD19 (B16-OVA-hCD19)[109] and used the parent B16-OVA melanoma cells as the CD19-negative control (**Fig. 20**). WT CAR, LiCAR, and defective CAR constructs were individually transduced into mouse $CD8^+$ T cells with their expression confirmed by flow cytometry (**Fig. 20b-c**). Subsequently, we quantified the production of mouse IFN-γ, which is secreted by activated T cells and plays a critical role in regulating cytotoxic $CD8^+$ T cell expansion in response to antigen recognition[110]. Indeed, the engineered B16-OVA-hCD19 cells effectively activated LiCAR-expressing mouse CD8 T-cells in the dual presence of CD19 and blue light, as reflected by the production of IFN-γ (**Fig. 21a**). Consequently, LiCAR-expressing $CD8^+$ T-cells showed photo-inducible killing of B16-OVA-hCD19 melanoma cells, with an E:T ratio of 10:1 showing the highest potency (**Fig. 21b-c**). By comparison, WT CAR T-cells induced tumor killing in a light-independent manner (**Fig. 21b** and **Fig. 21c**; left); whereas defective LiCAR T-cells co-cultured with B16-OVA-hCD19 cells showed no or negligible light-induced effects (**Fig. 21a-b** and **Fig. 21c**; right). Together, we demonstrated the successful engineering of photoswitchable CAR T-cells from both humans and mice to kill cancer cells derived from hematological malignancies (*e.g.,* lymphoma) and solid tumors (*e.g.*, melanoma).

***A hybrid nano-optogenetic platform for NIR light-instructed tumor killing in vivo.***

To further validate inducible and selective tumor killing mediated by LiCAR T-cells *in vivo*, we generated a syngeneic melanoma mouse model of CD19-positive solid

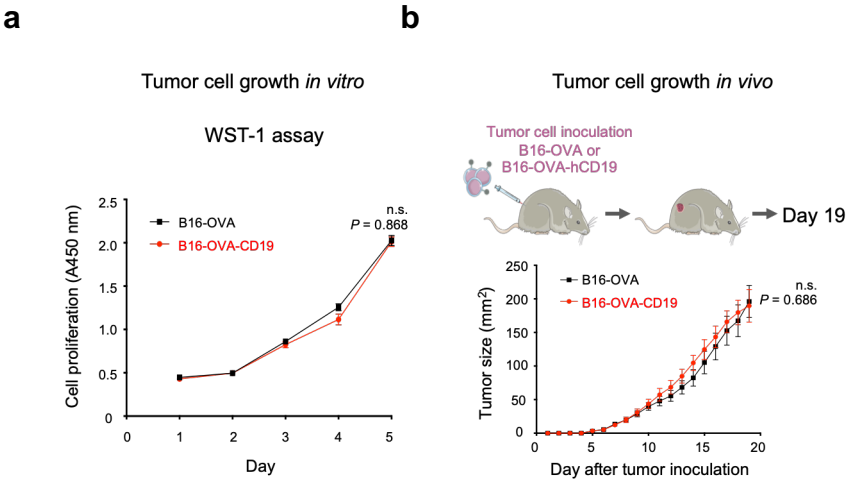


**Figure 22: The growth rates of B16-OVA and B16-OVA-hCD19 cells *in vitro* and *in vivo*.**
(**a**) *In vitro* cell proliferation of B16-OVA-CD19 and B16-OVA cells quantified using the WST-1 colorimetric assay. Absorbance at 450 nm was used as readout. n = 6 (mean ± s.e.m.)**.** (**b**) The growth curves of $5x10^5$ B16-OVA-CD19 and B16-OVA melanoma cells after intradermal injection into the left and right flanks, respectively, of C57BL/6J mice. Tumor sizes at the indicated time points were measured by a digital caliper with the tumor areas calculated in $mm^2$ (length x width). No significant difference in tumor sizes were noted. *P* = 0.686 when compared to the CD19-negative B16-OVA group at day 19 (paired two-tailed Student's *t-test;* n = 9; mean ± s.e.m.)

tumors by inoculating rodent B16-OVA-hCD19 cells into the flanks of C57BL/6J mice[109] (**Fig. 22**). Again, B16-OVA melanoma cells without CD19 were used as negative control. These two cancer cell lines showed comparable growth rates both *in vitro* (**Fig. 22a**) and *in vivo* (**Fig. 22b**), thus ruling out the possibility that CD19 *per se* might induce the differential growth of tumor cells.

We then set out to combine LiCAR T-cells with NIR light-activatable upconversion nanoparticles (UCNPs) to mitigate the tissue penetration issue associated with the *in vivo* application of blue light-activatable optogenetic tools[111]. We chose lanthanide-doped UCNPs as injectable nanoscale light transducers in order to enable wireless optogenetics, thereby obviating invasive procedures, such as implanting micro-LEDs or inserting fiber optics in tissues to deliver visible light[112]. The most significant advantage of upconversion nanoparticles is their unusual inverse excitation and emission profiles: UCNPs are excited using low power, deep tissue-penetrating, near infrared radiation, but this low energy input can be efficiently converted to a higher energy output emission at diverse shorter wavelengths, including blue light (400-500 nm) that can *in vivo* activate LiCAR T-cells **(Fig. 23a)**. We have previously employed this strategy to remotely control $Ca^{2+}$ signaling and the immune system during dendritic cell-based immunotherapy[9,15].

Here, to enhance upconversion luminescence intensity, we designed injectable hexagonal shaped upconversion nanoplates (UCNPs) with a core-shell composition of β-$NaYbF_4$:0.5%Tm@$NaYF_4$, in which $Yb^{3+}$ serves as the sensitizer to accept excitation energy and $Tm^{3+}$ serves as the emitter (**Fig. 23a**). Compared to the conventional ~30 nm spherical β-$NaYF_4$:30%Yb,0.5%Tm@$NaYF_4$ core-shell UCNPs used previously[15], such UCNPs possessed an elevated $Yb^{3+}$ concentration and enlarged nanoparticle size (**Fig. 23a**). This nanoplate design is expected to be able to enhance upconversion luminescence. This is due to the prior knowledge that the increased amount of $Yb^{3+}$ could enhance the energy absorption ability of the UCNPs and that surface defect-induced luminescence quench can be further significantly reduced in large

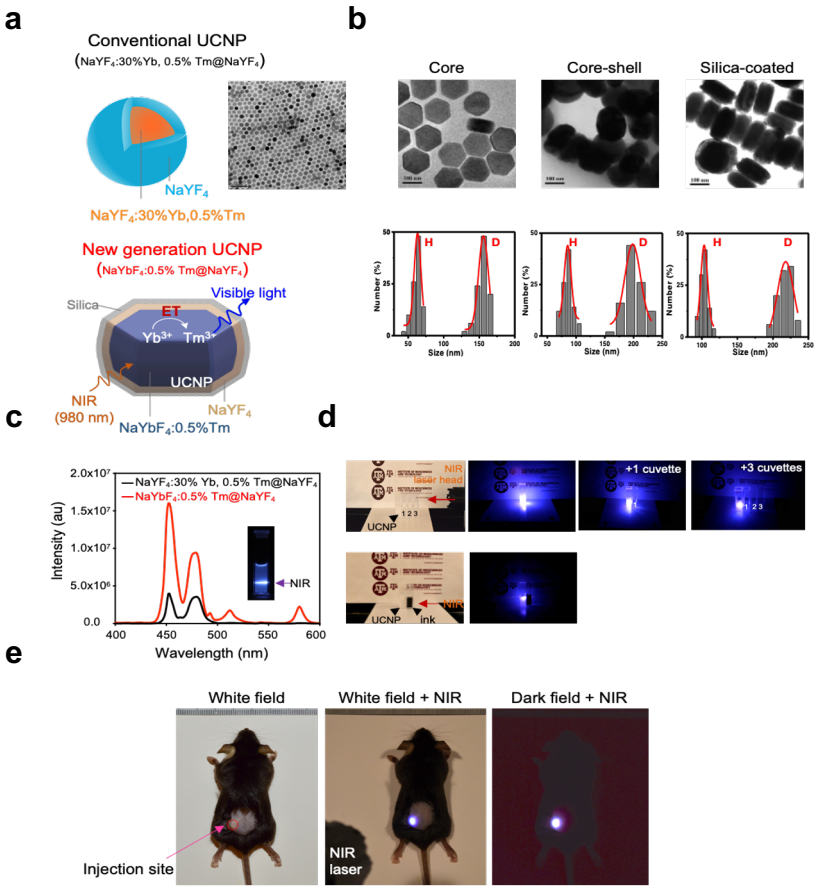


**Figure 23: Optimization and characterization of synthesized UCNPs.** (**a**) Comparison of the the core/shell structures of synthesized UCNPs and representative TEM images (right). Scale bar, 100 nm. (**b**) Representative TEM images and the size distribution (height denoted as "H" and diameter denoted as "D") of the $NaYbF_4$:0.5%Tm core nanoparticles (left), $NaYbF_4$:0.5%Tm@$NaYF_4$ core-shell nanoplates (middle), and silica-coated $NaYbF_4$:0.5%Tm@$NaYF_4$ core-shell nanoplates (right). (**c**) Comparison of the upconversion luminescence spectra of synthesized UCNPs upon NIR light illumination at 980 nm. (**d**) Blue light emitted from the leftmost cuvette containing UCNPs (β-$NaYbF_4$:0.5%Tm@NaYF4) upon NIR illumination. The UCNP-containing cuvette (leftmost) was placed next to the indicated numbers of $H_2O$-containing plastic cuvettes (labeled as 1, 2 and 3; *top*) or a cuvette containing dark ink (bottom). The NIR light source (980 nm) was placed on the right. Pictures were taken in a dark room except for the leftmost images. (**e**) Injectable UCNPs emitted bright blue light locally at the injection site *in vivo* upon NIR light stimulation (980 nm; 250 mW/cm$^2$). Pictures were taken for the same mouse in the bright field without NIR (left) or with NIR light (middle), or in the dark field with NIR light (right).

nanoparticles. In particular, owing to the smaller ionic size of $Yb^{3+}$ compared to $Y^{3+}$, the

replacement of $Y^{3+}$ with $Yb^{3+}$ in UCNP synthesis suppressed the nucleation process and pronouncedly prolonged nanocrystal growth[113]. In this regard, the number of

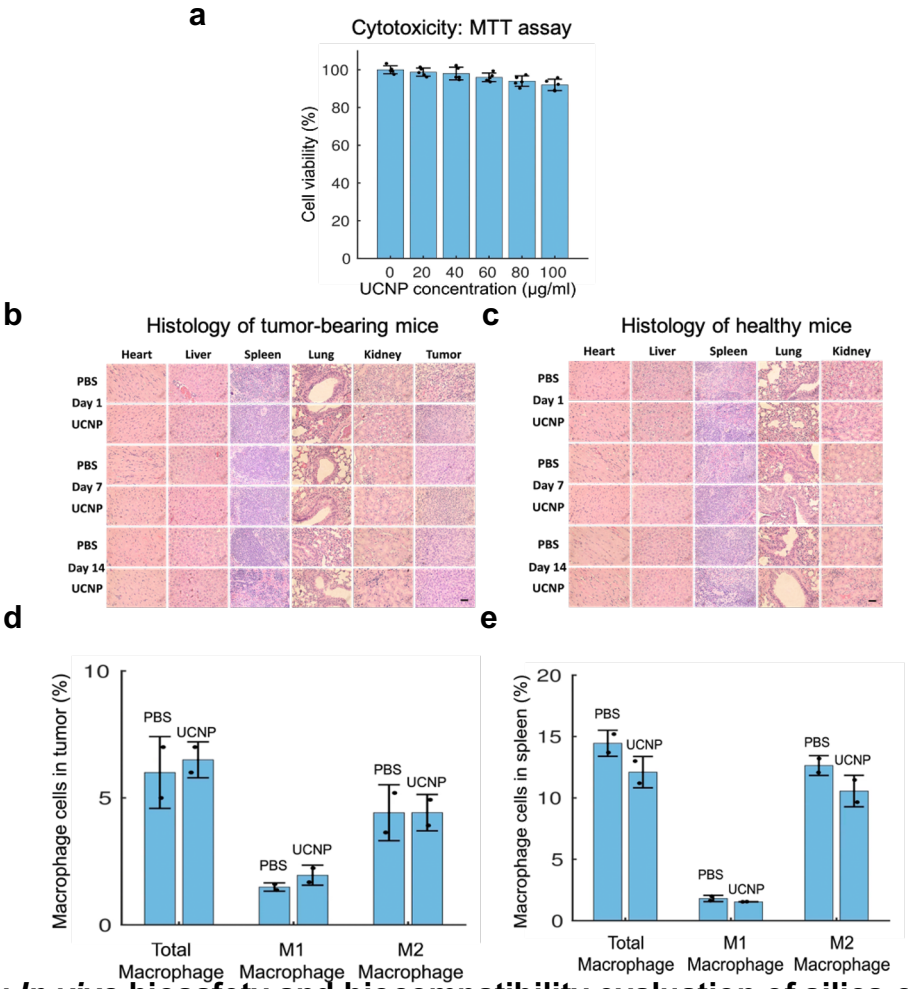


**Figure 24: *In vivo* biosafety and biocompatibility evaluation of silica-coated UCNPs**.

(**a**) MTT assay of B16-OVA-mCD19 cell viability with different concentrations of UCNPs**.** (**b-c**) H&E staining images of major organs (heart, liver, spleen, lung, kidney and tumor) of UCNPs or PBS-injected tumor-bearing mice (b) and healthy mice (c). Scale bar, 100 μm. (**d-e**) The percentage of total macrophages, M1 macrophages and M2 macrophages in the tumor (d) and spleen (e) in UCNP/PBS-injected mice.

nanoparticles in the reaction solution will be less, but their size will be enlarged when using the same amount of lanthanide precursors. As a result, the synthesized β-

$NaYbF_4$:0.5%Tm core possesses a hexagonal plate shape with an enlarged size (~155

**Table 1**. Blood biochemistry and complete blood panel analysis of mice injected with PBS or UCNPs.

| | Normal range | Tumor bearing mice | | | | | | Healthy mice | | | | | |
|---|---|---|---|---|---|---|---|---|---|---|---|---|---|
| | | Day 1 | | Day 7 | | Day 14 | | Day 1 | | Day 7 | | Day 14 | |
| | | PBS | UCNP | PBS | UCNP | PBS | UCNP | PBS | UCNP | PBS | UCNP | PBS | UCNP |
| WBC (K/μL) | 1.8-10.7 | 3.39 | 2.85 | 3.17 | 3.21 | 4.14 | 3.87 | 3.56 | 2.93 | 3.73 | 3.86 | 4.6 | 4.82 |
| LY (K/μL) | 0.9-9.3 | 2.96 | 2.32 | 2.72 | 2.78 | 3.02 | 2.48 | 3.25 | 2.24 | 3.29 | 3.28 | 4.1 | 4.21 |
| MO (K/μL) | 0.0-0.4 | 0.09 | 0.11 | 0.11 | 0.09 | 0.22 | 0.22 | 0.12 | 0.23 | 0.13 | 0.07 | 0.09 | 0.14 |
| NE (K/μL) | 0.1-2.4 | 0.34 | 0.42 | 0.34 | 0.35 | 0.9 | 1.17 | 0.2 | 0.46 | 0.31 | 0.51 | 0.41 | 0.47 |
| RBC (M/μL) | 6.36-9.42 | 10.04 | 8.13 | 8.18 | 8.41 | 10.31 | 9.38 | 9.28 | 7.95 | 9.34 | 9.56 | 8.57 | 9.41 |
| HGB (g/dL) | 11.0-15.1 | 14.3 | 11.5 | 11.7 | 12.5 | 13.6 | 12.5 | 12.4 | 10.7 | 12.7 | 13.7 | 12.1 | 13.4 |
| HCT (%) | 35.1-45.4 | 53.45 | 41.38 | 44.45 | 45.92 | 56.88 | 51.78 | 50.57 | 45.19 | 47.47 | 47.65 | 48.89 | 53.34 |
| MCV (fL) | 45.4-60.3 | 53 | 51 | 54 | 55 | 55 | 55 | 54 | 57 | 51 | 50 | 57 | 57 |
| MCH (pg) | 14.1-19.3 | 14.2 | 14.1 | 14.3 | 14.9 | 13.2 | 13.3 | 13.3 | 13.5 | 13.6 | 14.3 | 14.1 | 14.3 |
| MCHC (K/μL) | 30.2-34.2 | 26.7 | 27.8 | 26.3 | 27.3 | 23.9 | 24.1 | 24.4 | 23.8 | 26.8 | 28.7 | 24.7 | 25.2 |
| RDW (K/μL) | 12.4-27.0 | 23.5 | 24.1 | 21.2 | 21.8 | 22.2 | 22.2 | 22.6 | 22.6 | 25.9 | 22.1 | 20.5 | 20.8 |
| MPV (fL) | 5.0-20.0 | 7.7 | 5.6 | 6.3 | 6.4 | 6.8 | 6.8 | 7.9 | 6.8 | 6.2 | 6.3 | 6.7 | 7.6 |

Abbreviations: White blood cell (WBC), Neutrophils (NE), Lymphocytes (LY), Monocytes (MO), Eosinophils (EO), Basophils (BA), Red blood cell (RBC), Hemoglobin (HGB), Hematocrit (HCT), Mean corpuscular volume (MCV), mean corpuscular hemoglobin (MCH), Mean corpuscular hemoglobin concentration (MCHC), Red blood cell distribution width (RDW), Platelet Thrombocyte (PLT), Mean platelet volume (MPV).

nm in diameter and ~62 nm in height; **Fig. 23b**). The produced β-$NaYbF_4$:0.5%Tm@$NaYF_4$ core-shell nanoplate displayed a hexagonal plate shape with a size of approximately 200 nm × 85 nm (**Fig. 23b**). We observed that the resultant core/shell nanoplates via these two modifications (higher $Yb^{3+}$ doping and larger size core/shell structure) indeed had markedly boosted upconversion luminescence brightness (**Fig. 23c**). When excited at 980 nm, the synthesized UCNPs exhibited intense emission peaks in the blue light range, with an intensity increased by 4.5-fold when compared to the conventional UCNPs with the same amount of total lanthanide ions (**Fig. 23c**). To further transfer these UCNPs from the organic solvent to an aqueous solution, a layer of silica shell was coated on the surface of the core-shell UCNPs,

giving the final silica-coated core-shell nanoplate a size of ~217 nm (diameter) × ~103 nm (height) (**Fig. 23b**) or an apparent hydrodynamic radius of approximately 220 nm. When illuminated with a 980-nm laser, blue light emitting from the UCNP-containing cuvette in aqueous solutions can easily be seen by the naked eye, even after penetrating through multiple water-containing plastic cuvettes beside the UCNPs (**Fig. 23d**). When the silica-coated UCNPs were subcutaneously injected into mice, we detected bright blue light emission from the injection site following exposure to a brief pulse of NIR light illumination (**Fig. 23e**).

We next examined the potential cytotoxicity and *in vivo* biosafety of silica-coated UCNPs. In the cytotoxicity study, B16-OVA-hCD19 cells were incubated with culture media containing UCNPs at different concentrations (0 μg/mL – 100 μg/ml). Using an MTT assay, we found that the cell viability was not significantly affected by the UCNPs. With up to 100 μg/ml UCNPs in the cell culture solution, the cell viability remained at more than 90%, thus indicating no obvious cytotoxicity of the UCNPs (**Fig. 24a**). Furthermore, we investigated the *in vivo* toxicity of UCNPs through pathological study and blood analysis. In both studies, tumor-bearing mice were injected with UCNPs (1mg $mL^{-1}$, 150 μL) and sacrificed at different times (1 day, 7 days and 14 days) after UCNP-injection. PBS-injected mice were used as the control. By comparing H&E stained images of the major organs (heart, liver, spleen, lung, kidney and tumor) from UCNP-injected and PBS-injected mice, we found that neither group displayed noticeable organ damage or inflammatory lesions (**Fig. 24b**), suggesting that no obvious heart, liver, spleen, lung, or kidney dysfunction for the mice was induced by the UCNPs. In the

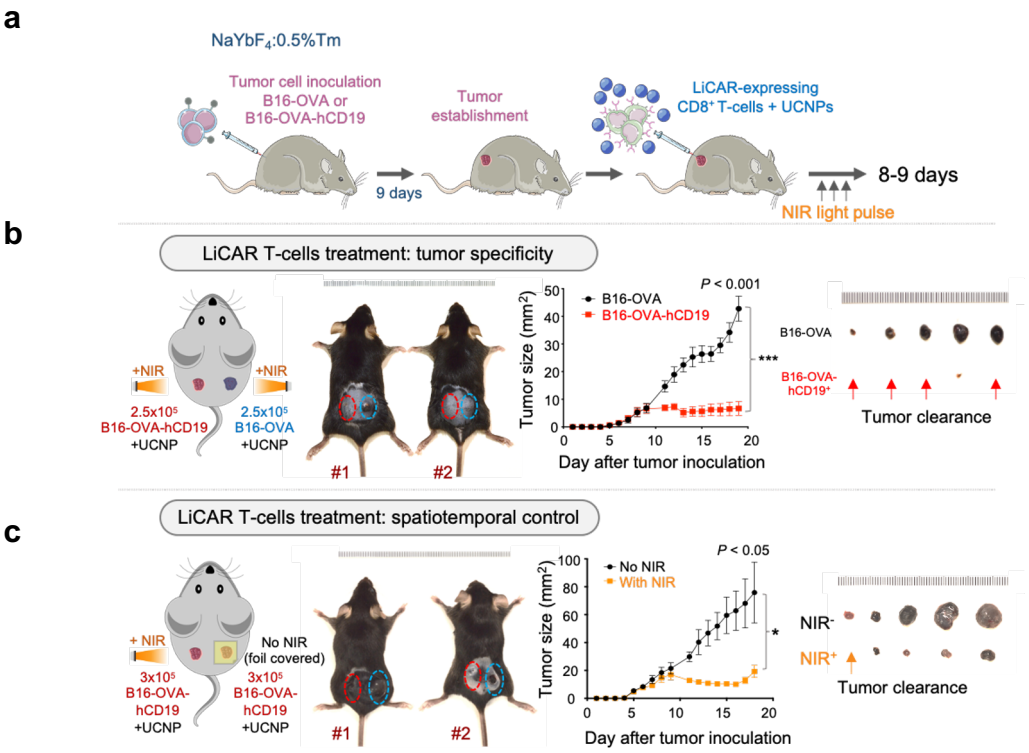


**Figure 25: A nano-optogenetic strategy for selective destruction of melanoma using LiCAR T-cells**

(**a**) Schematic of the *in vivo* experimental setup. (**b**) LiCAR CD8$^+$ T-cells selectively destroy CD19-expressing melanoma in response to NIR light illumination. *Left*, C57BL/6J mice were intradermally inoculated with 2.5x10$^5$ B16-OVA-hCD19 in the left flank (red circle) and 2.5x10$^5$ B16-OVA cells (CD19-negative tumor as control; blue circle) in the right flank. Two representative mice are shown after treatment with 2x10$^6$ LiCAR T-cells + 150 µg UCNPs and exposure to NIR pulses for 9 days. *Middle,* tumor sizes at the indicated time points were measured by a digital caliper with the tumor areas calculated in mm$^2$ (length x width). ****P* < 0.0001 when compared to the CD19-negative B16-OVA group (paired two-tailed Student's *t-test;* n = 5; mean ± s.e.m.). *Right,* isolated B16-OVA and B16-OVA-hCD19 tumors at day 19. (**c**) LiCAR T-cells permit NIR light-inducible killing of B16-OVA-hCD19 melanoma in selected regions. *Left,* C57BL/6J mice were intradermally inoculated at both flanks with 3x10$^5$ B16-OVA-hCD19 cells. After injection with 2x10$^6$ LiCAR T-cells + 150 µg UCNPs, the left flank (red circle) was exposed to NIR pulses for 8 days, while the right side (blue circle) was protected from NIR light using aluminum foil. Two representative mice are shown at day 18. *Middle*, tumor sizes were measured at the indicated time points. *Right,* isolated B16-OVA-hCD19 tumors with and without exposure to NIR light at day 18. **P* < 0.05 when compared to the non-NIR group (paired two-tailed Student's *t-test;* n = 5; mean ± s.e.m.).

blood analysis, UCNP-injected mice showed similar parameters compared to the PBS-injected mice (**Table 1**), and both of them generally fell in the normal range, which suggests that no observable unwanted inflammation was induced. In particular, the white blood cells of both groups were at the same level (**Table 1**), which indicates that no immunologic responses were induced by the UCNPs. In addition to the tumor-bearing mice, these *in vivo* biosafety studies were also performed on healthy mice, which also showed no obvious toxicity induced by the UCNPs at this dosage (**Fig. 24c**). Macrophages are capable of phagocytosing foreign bodies; to examine whether UCNPs could activate macrophages, we evaluated macrophage numbers and polarization in UCNP-injected tumor bearing mice. 14 days after UCNP injection (1mg $mL^{-1}$, 150 μL), the mice were sacrificed, and the percentage of macrophage cells in tumor and spleen were studied. PBS-injected mice were used as the control group. We found that, compared to the PBS-injected mice, the UCNP did not induce obvious differences in total macrophages, M1 macrophages, or M2 macrophages in either tumor or spleen (**Fig. 24d-e**), indicating that UCNPs did not activate macrophages. Together, these data clearly established the feasibility of using our synthesized UCNPs to enable wireless optogenetics in living animals.

Next, in order to assess the ability of anti-CD19 LiCAR-transduced T cells to eliminate antigen-specific melanoma masses, we conducted *in vivo* experiments with intradermal melanoma models, in which tumor cells bearing the non-cognate antigen (B16-OVA) and cognate antigen (B16-OVA-hCD19) were implanted into each flank of the same C57BL/6J mouse (**Fig. 25a-c**). After 9 days of tumor establishment, the tumor sites were injected with WTCAR (the positive control) or LiCAR $CD8^+$ T cells ($2 \times 10^6$)

and 150 μg of UCNPs, in the presence or the absence of pulsed NIR light stimulation for 8-9 subsequent days (980 nm at a power density of 250 mW/cm$^2$; 2 h/day; pulses of 20

**Table 2. Major chemical element distributions in the indicated tissues**

| Atomic (%) composition | Tumor/ injection site | Tumor surrounding tissues | Heart | Liver | Spleen | Lung | Kidney |
|---|---|---|---|---|---|---|---|
| Y | 4.02 | | | | | | |
| Yb | 4.07 | | | | | | |
| Si | 7.91 | | | | | | |
| F | 46.76 | | | | | | |
| Na | 6.19 | 0.20 | | | 13.11 | 0.28 | |
| O | 31.05 | 66.60 | 69.77 | 66.72 | 64.67 | 66.59 | 66.79 |
| C | | 33.09 | | 33.14 | | 32.84 | 32.65 |
| S | | | 14.29 | 0.15 | 5.15 | 0.14 | 0.19 |
| P | | | 7.30 | | 17.07 | 0.14 | 0.37 |
| Zn | | | 8.65 | | | | |
| Mo | | 0.11 | | | | | |

sec ON + 5 min OFF). As a positive control, WT CAR T-cells exhibited tumor antigen-specificity by killing tumors of B16-OVA-hCD19 cells, but they did not kill B16-OVA cells (**Fig. 26a**). As a stringent negative control, the NIR light-treated groups injected with UCNPs alone without LiCAR T-cells did not seem to affect the overall tumor growth (**Fig. 26b-c**). This result rules out the possible complications from UCNPs and NIR light *per se*. For the LiCAR T-cell treated group, NIR light stimulation was found to substantially suppress B16-OVA-hCD19 tumor growth in the left flank, while CD19-negative B16-OVA tumors on the right side remained largely unaffected (**Fig. 25b**). It is noteworthy that the injected UCNPs appeared to be confined at the injection site or within the tumor mass and thus could be surgically removed after the treatment via

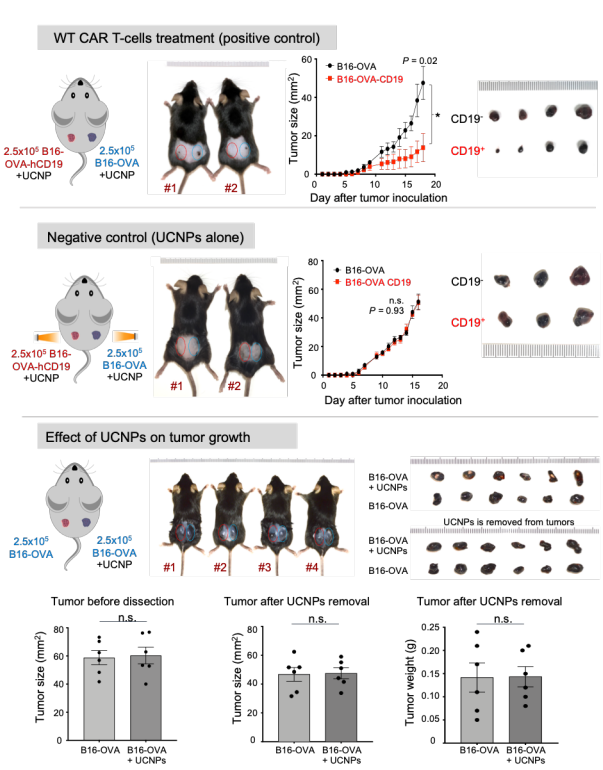


**Figure 26: Effects of WT CAR T-cells and UCNPs on tumor growth.**
(**a**) WT CAR-expressing CD8$^+$ T-cells selectively destroy CD19-positive melanoma tumors without light stimulation. *Left*, C57BL/6J mice were intradermally inoculated with 2.5x10$^5$ B16-OVA-hCD19 cells in the left flank (red circle) and 2.5x10$^5$ B16-OVA cells (blue circle) in the right flank. Two representative mice are shown after treatment with WT CAR T-cells + UCNPs for 8 days. *Middle,* Tumor sizes at the indicated time points. *$P$ < 0.05 (paired two tailed Student's *t-test;* n = 4; mean ± s.e.m.). *Right,* isolated B16-OVA and B16-OVA-hCD19 tumors at day 18. (**b**) The growth curves of B16-OVA-CD19/UCNPs and B16-OVA/UCNPs upon NIR light irradiation. *Left*, C57BL/6J mice were intradermally inoculated with 2.5x10$^5$ B16-OVA-hCD19 cells in the left flank (red circle) and 2.5x10$^5$ B16-OVA cells (blue circle) in the right flank. Two representative mice are shown after injection of UCNPs for 8 days without CAR T-cells under NIR treatment. *Middle,* Tumor sizes at the indicated time points. $P$ = 0.93 (paired two-tailed Student's *t-test;* n = 3; mean ± s.e.m.). *Right,* isolated B16-OVA and B16-OVA-hCD19 tumors at day 16. **c**, UCNPs did not affect tumor growth. C57BL/6J mice were intradermally inoculated with 2.5x10$^5$ B16-OVA cells to each flank. Four representative mice are shown after injection with UCNPs to the right flank tumor. *Top right,* isolated B16-OVA and B16-OVA-UCNPs tumors before and after UCNP removal at day 18. *Bottom left and middle,* tumor sizes before tumor surgery (measured from outside skin) and after UCNP removal, respectively at day 18. *Bottom right,* tumor weight after UCNP removal at day 18.

upconverting emission imaging guidance (**Fig. 27**). Locally injected UCNPs remained structurally intact (**Fig. 27a**) and did not seem to spread to other major organs, including the tumor-adjacent tissue, heart, liver, spleen, lungs, and kidney (**Fig. 27b**). Furthermore, these UCNPs were stable through the time window of treatment. We monitored UCNPs through TEM at different time points (day 1, day 7 and day 14) and found that UCNPs were clearly observable with no obvious morphological changes through 28 days (**Fig. 28,** top; longer-term *in vivo* study was performed in intramuscular UCNP-injected healthy mice). In addition, under 980 nm laser excitation, the UCNP emissions were clearly observable (**Fig. 28,** bottom). In contrast, there was no emission from major organs without UCNPs. Thus, UCNPs were stable both physically and optically *in vivo* for at least 28 days. These findings indicate that there is no observable nanoparticle leakage from the injected site in tumor to other organs. To more rigorously rule out the potential trace leakage of the nanoparticle to the surrounding tissue and major organs, we performed a systematic element analysis of the nanoparticle distribution in living tissues by using an energy-dispersive X-ray spectroscopy (EDS) coupled SEM system. The lanthanide elements (Y and Yb) as well as Si of the silica shell were only detectable in the UCNP-injected tumor (**Table 2**). In all the other tissues/organs, including the tumor surrounding tissues, heart, liver, spleen, lungs, and kidney, we did not detect lanthanide elements or Si derived from the injected UCNPs (**Table 2**). As summarized in **Table 2**, the composition of elements in the UCNP-injected tumor largely agreed with the composition of silica-coated $NaYbF_4$:Tm@$NaYF_4$ UCNPs. By contrast, other tissues were mainly composed of physiologically-relevant elements, such as O, C, S, and P. Together, these results firmly established that UCNPs strictly

accumulated in the tumor after injection and could be removed by imaging guided

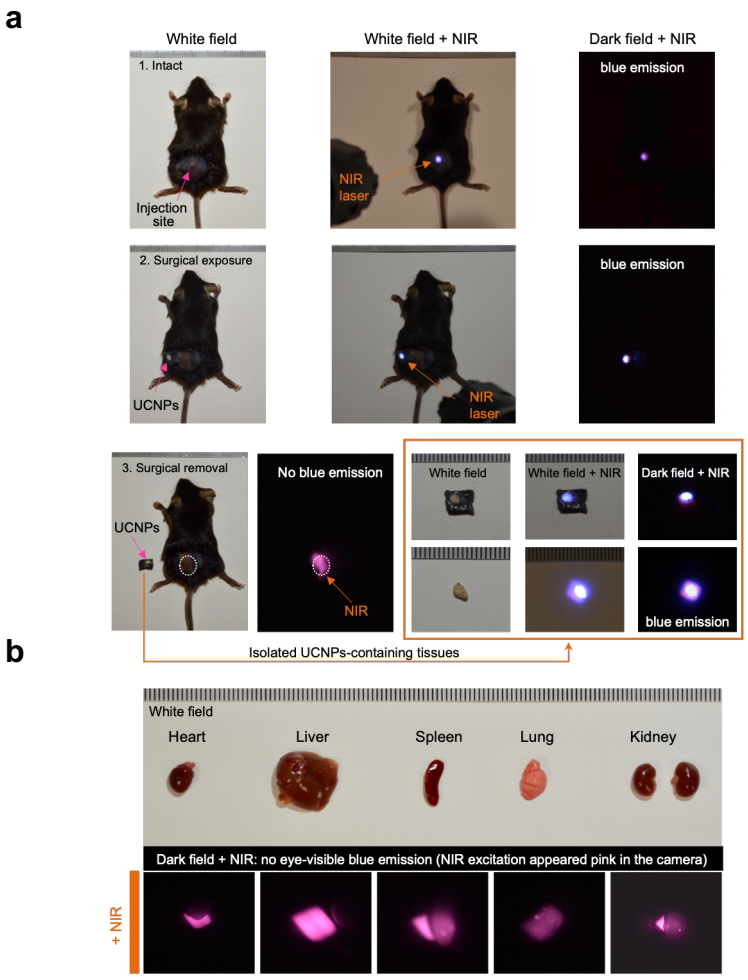


**Figure 27: UCNPs are well confined within the injection site.**
(**a**) Visualizing UCNPs after *s.c.* injection into the tumor sites under the indicated conditions. Images were acquired in the same mouse under three conditions: bright field without NIR light (left), bright field with NIR light illumination (middle) at the injection site (red arrow), or in the dark room with NIR light (right). *Top*, in situ images; *middle*, the UCNP-containing skin tissues were surgically exposed; *bottom*, after surgical removal. The NIR excitation showed a pink color in the camera if blue emission was not detected. Zoomed-in view on the right (orange box): The UCNP-containing skin/tumor tissues (top) and well-confined UCNPs isolated from the tissue (bottom). (**b**) UCNPs did not spread to other major organs within the experimental window. Major organs were isolated from the mouse shown in panel a and then subjected to NIR light illumination. Only pink color was noted without blue emission, suggesting the absence of UCNPs in these tissues.

surgery without appreciable leakage to the surrounding tissues and other major organs.

Because the engineered LiCAR T-cells expressed both GFP- and mCherry-tagged components, we further analyzed the population of surviving and/or locally expanded LiCAR T-cells within tumor masses 9 days after injection by flow cytometry (**Fig. 29**). As anticipated, a significant portion of dual-colored LiCAR T-cells was detected within the $CD19^+$ tumors, but not in those formed by CD19-negative B16-OVA cells (**Fig. 29a-b**). In addition, we did not observe a significant presence of LiCAR T-cells in the peripheral lymphoid organs (such as the spleen) or in the peripheral blood at the endpoint (**Fig. 29c**). There are two possible explanations for this finding. First, the locally-injected, NIR light-activated LiCAR T-cells could not efficiently migrate to distal tissues. Alternatively, in the absence of NIR light and cognate tumor antigens, the extra-tumorous LiCAR T cells were not activated and may be eliminated 9 days after injection.

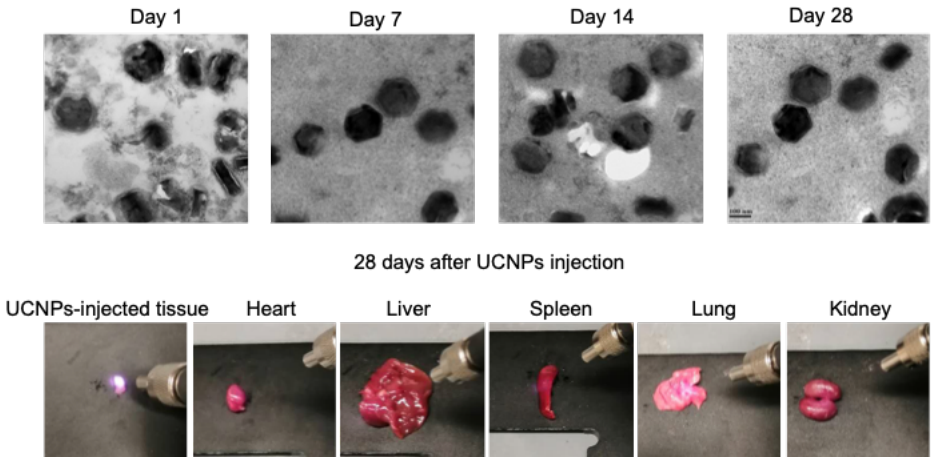


**Figure 28: Stability of UCNPs *in vivo***
Top level: TEM images showing stability of UCNPs at different time points after injection in tumor (day 1, day 7 and day 14) or leg muscle (day 28) of mice. Bottom level: UCNPs showing bright emission under 980 nm laser excitation 28 days after being injected into the leg muscle of mice; other organs without UCNPs were used as the controls.

Regardless, limited extra-tumoral distribution of LiCAR T-cells could be beneficial for the

spatial control of therapeutic activity. Taken together, we have established a robust nano-optogenetic platform to temporally control LiCAR T-cells in order to achieve tumor-specific immune responses *in vivo*.

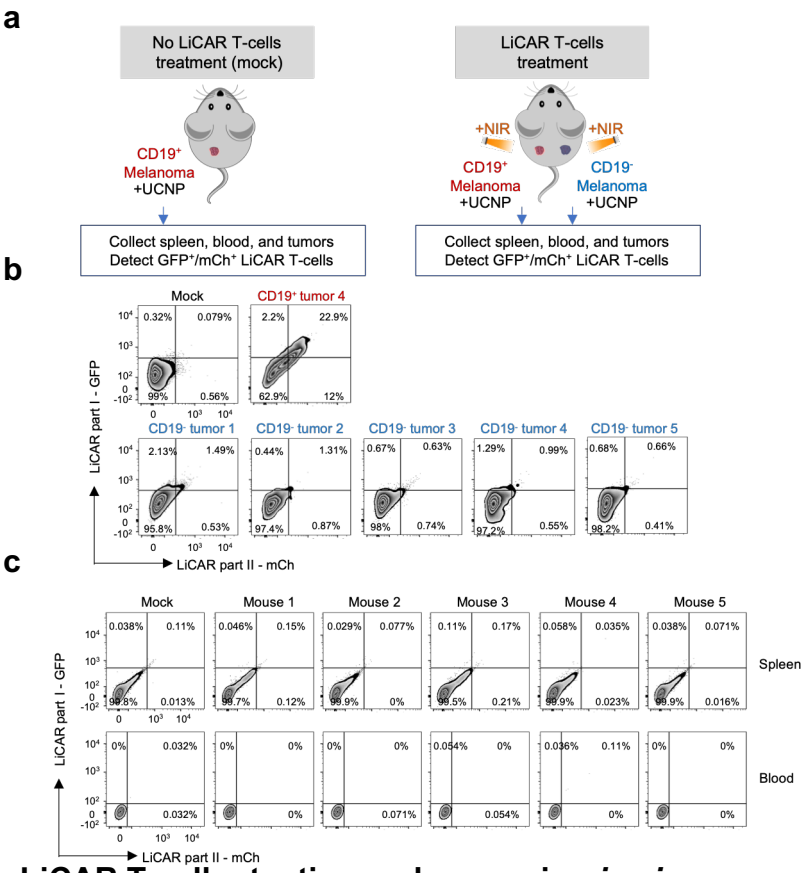


**Figure 29: LiCAR T-cell retention and expansion *in vivo*.**
(**a**) Schematic of the *in vivo* experimental setup for LiCAR T-cell isolation from mice bearing melanoma tumors. *Left*, B16-OVA-hCD19 inoculation, without LiCAR T-cells + UCNPs and NIR treatment (as mock control); *Right*, B16-OVA hCD19 (left flank) and B16-OVA inoculation (right flank), with LiCAR T-cells + UCNPs and NIR treatment. (**b**) FACS analysis of LiCAR T-cells (GFP+/mCherry+) within the isolated tumor masses at day 19 (shown in Fig. 16b). LiCAR T-cells were mostly detected in the B16-OVA-hCD19 tumor, but were not readily detectable in the mock and B16-OVA tumors (n= 5 mice). **c**, Monitoring the off-tumor distribution of LiCAR T-cells by flow cytometry. Nominal GFP+/mCherry+ signals were detected in the spleen and peripheral blood isolated from the B16-OVA-hCD19 group.

To demonstrate the spatiotemporal control of LiCAR T-cells to kill tumors *in vivo*, we implanted B16-OVA-hCD19 cells into each flank of C57BL/6J mice. After tumor

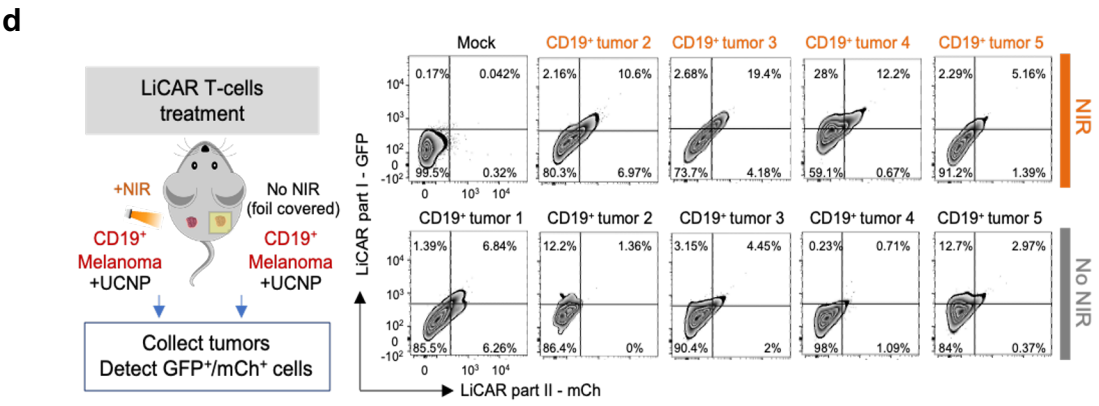


**Figure 29: | LiCAR T-cells retention and expansion *in vivo*. (continued)** (**d**) FACS analysis of LiCAR T-cells within the isolated tumor masses at day 18 (shown in **Fig. 18c**). LiCAR T-cells were more abundantly detected in the tumors exposed to NIR light (from four mice) when compared to the mock and the non-NIR treated tumors (n = five mice), indicating more robust activation/expansion of LiCAR T-cells after NIR-inducible reconstitution of functional CARs.

formation at day 9, both tumor sites were injected with a mixture of $CD8^+$ LiCAR T-cells and UCNPs, followed by exposure to pulsed NIR light on the left side or being shielded from light with aluminum foil on the right side (**Fig. 25c**). We found that tumor regression or clearance was only observed in the NIR light-treated side, but not in the site shielded from light (**Fig. 25c**). Within the tumor masses, we detected a higher amount of viable LiCAR T-cells, as reflected by a stronger intensity of the GFP/mCherry double-positive population at day 9 following NIR light stimulation (**Fig. 29d**). Together, our data firmly established the feasibility of spatiotemporal control over engineered T cell activation and selective tumor killing only at the desired tumor sites.

In parallel, we performed similar experiments under blue light illumination. We did not detect a statistically significant difference between the dark and lit groups **(Fig. 30)**. This finding is consistent with the tacit notion that blue light can penetrate no more than 1 mm in living tissues[114], thereby failing to effectively activate LiCAR T-cells within the

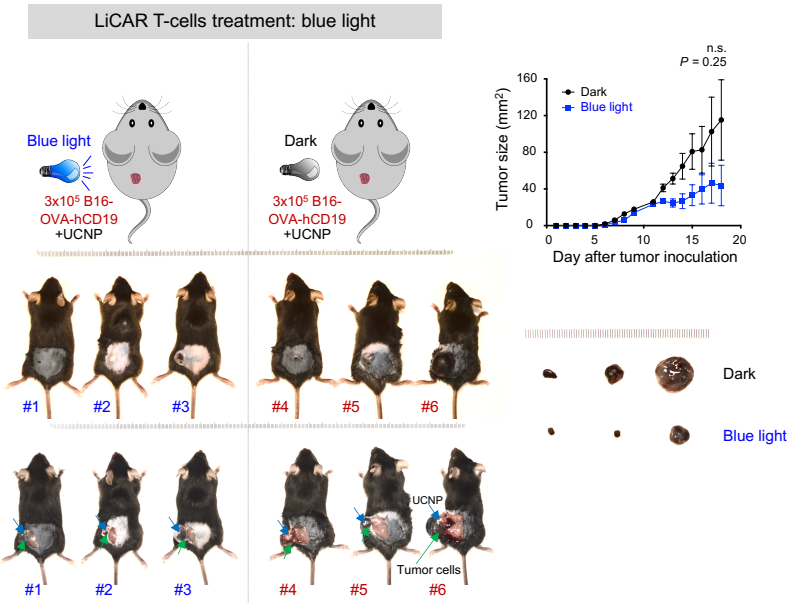


**Figure 30: Blue light did not induce statistically significant changes in tumor killing.**
*Left,* C57BL/6J mice were intradermally inoculated in the left flank with $3x10^5$ B16-OVA-hCD19 cells. After injection with the LiCAR T-cells + UCNP mixture, mice were either exposed to blue light (470 nm; 40 mW/cm$^2$, 2 hours per day) for 8 days, or kept in the dark. Three representative mice from each group with opened tumors are shown at day 18. *Green arrow*, tumor cells. *Blue arrow*, UCNPs injected to tumor sites. *Top right,* tumor sizes at the indicated time points were measured by a digital caliper with the tumor areas calculated in mm$^2$ (length x width). $P = 0.25$ when compared to the dark group at day 18 (paired two-tailed Student's *t-test*; mean ± s.e.m.). *Bottom right,* isolated B16-OVA-hCD19 tumors treated with or without blue light at day 18.

tumor sites. However, this bottleneck has been overcome by taking our nano-

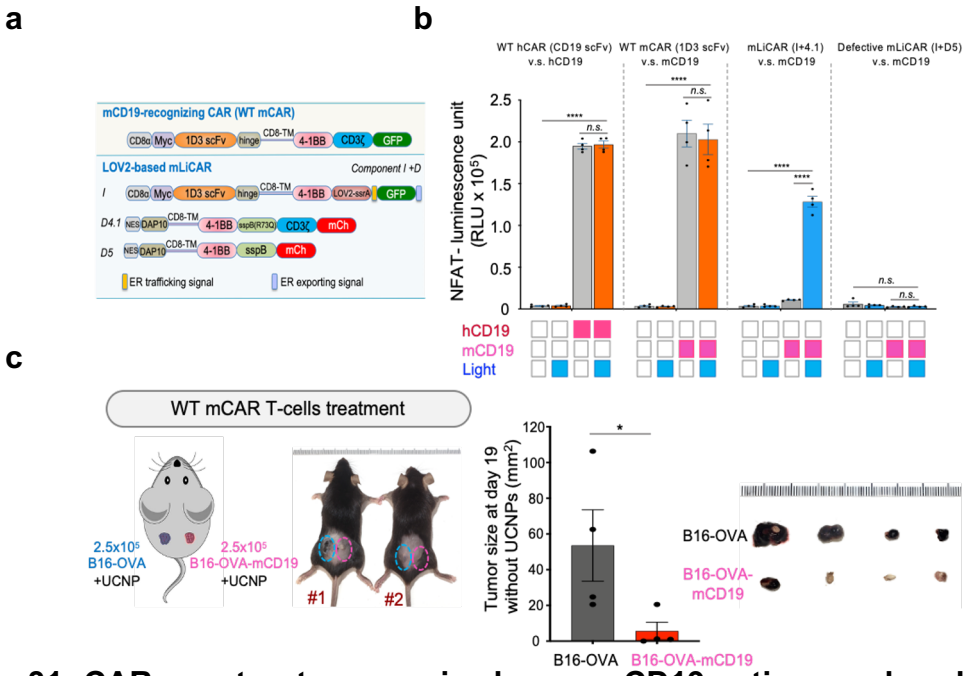


**Figure 31: CAR constructs recognized mouse CD19 antigen and evaluation of the on-target off-tumor effect of mLiCAR.**

(**a**) Conventional CAR (mWT CAR) and LiCAR (mLiCAR) constructs recognizing the mCD19 antigen via the antigen recognition domain derived from mouse mAb (1D3 scFv). (**b**) The engagement of 1D3 scFv to mCD19 antigen was quantified by NFAT-dependent luciferase (NFAT-Luc) reporter activity in Jurkat T cells. Jurkat T cells transduced with human hCD19 antigen-recognizing constructs (WT CAR) or mouse mCD19 antigen-recognizing constructs (mWT CAR, mLiCAR, or defective mLiCAR) engaged with tumor cells bearing noncognate (open box; B16-OVA cells) or cognate antigens (red box; B16-OVA-hCD19$^+$ or B16-OVA-mCD19$^+$) under dark (open box) or lit conditions (blue box). Defective LiCAR lacking the CD3ζ-ITAM domain was used as a negative control. n = 4 (mean ± s.e.m.). ****$P$ < 0.0001 compared to dark group; n.s., not significant (two-tailed Student's $t$-test). (**c**) mWT CAR-expressing CD8$^+$ T-cells selectively destroyed CD19-positive melanoma tumors without light stimulation. *Left*, C57BL/6J mice were intradermally inoculated with 2.5x10$^5$ B16-OVA in the left flank (blue circle) and 2.5x10$^5$ B16-OVA-mCD19 cells (red circle) in the right flank. Two representative mice are shown after treatment with mWT CAR T-cells + 150 μg UCNPs for 10 days. *Middle,* Tumor sizes at the endpoint after UCNP removal were measured by a digital caliper with the tumor areas calculated in mm$^2$ (length x width). *$P$ < 0.05 when compared to the CD19-negative B16-OVA group at day 19 (paired two-tailed Student's *t-test;* n = 4; mean ± s.e.m.). *Right,* isolated B16-OVA and B16-OVA-mCD19 tumors with UCNPs at day 19.

optogenetic immunomodulation approach using the injectable and removable enhanced NIR-to-blue emission UCNP method.

***LiCAR T-cells mitigate side effects associated with immunotherapy.***

We have demonstrated that our LiCAR system can perform with both specificity and spatiotemporal control in targeting tumors *in vivo*. Therefore, we anticipated that the LiCAR system could mitigate the side-effects caused by constitutively activated CAR T cells such as “on-target, off-tumor”cytotoxicity and cytokine release syndrome (CRS). We used a new mouse model to evaluate the “on-target, off-tumor” side effects of LiCAR compared to conventional CAR. We designed a new set of mouse LiCARs (mLiCARs), in which scFv recognizing mouse CD19 antigen (mCD19Ag) was derived from a mouse mAb (1D3 ScFv). 1D3 ScFv was exchanged for the hCD19 ScFv in conventional CAR or LiCAR (C+D4.1) constructs (**Fig. 31**). In order to examine whether 1D3 ScFv can recognize mouse CD19 antigen as well as to assess the degree of T cell activation, we again used the NFAT-dependent luciferase (NFAT-Luc) reporter assay (**Fig. 31b**). NFAT-Luc Jurkat T cells expressing engineered receptors (mWT CAR or mLiCAR) were engaged with CD19-negative B16-OVA melanoma cells or CD19-positive B16-OVA-mCD19 cells. mWT CAR-T cells only required mCD19Ag to be activated and its bioluminescence level was as high as hWT CAR (CD19scFv)/ B16-OVA-hCD19 suggesting that mCAR constructs can recognize mCD19Ag (**Fig. 31b**). For mLiCAR, in the dual presence of cognate tumor antigen (B16-OVA-mCD19 cells) and light stimulation, we detected an increase in bioluminescence, indicating the antigen/light-dependent activation of engineered mLiCAR T cells (**I + D4.1; Fig. 31b**).

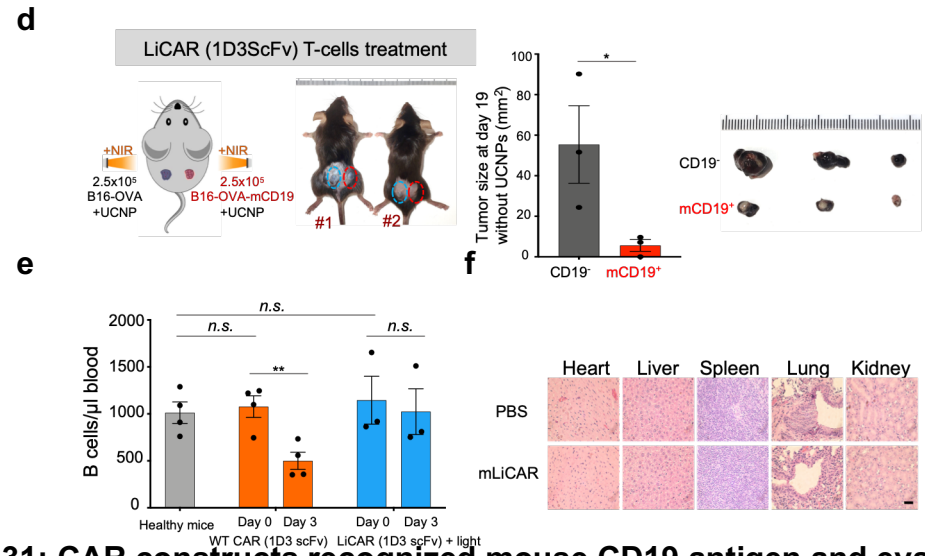


**Figure 31: CAR constructs recognized mouse CD19 antigen and evaluation of the on-target off-tumor effect of mLiCAR. (Continued).** (**d**) mLiCAR CD8$^+$ T-cells selectively destroy CD19-expressing melanoma in response to NIR light illumination. *Left*, C57BL/6J mice were intradermally inoculated with 2.5x10$^5$ B16-OVA cells in the left flank (blue circle) and 2.5x10$^5$ B16-OVA-mCD19 cells (blue circle) in the right flank. Two representative mice are shown after treatment with 2x10$^6$ mLiCAR T-cells + 150 µg UCNPs and exposure to NIR pulses for 10 days. *Middle,* Tumor sizes at the endpoint after UCNP removal were measured by a digital caliper with the tumor areas calculated in mm$^2$ (length x width). *$P$ < 0.05 when compared to the CD19-negative B16-OVA group at day 19 (paired two-tailed Student's *t-test;* n = 3; mean ± s.e.m.). *Right,* isolated B16-OVA and B16-OVA-mCD19 tumors with UCNPs at day 19. (**e**) On-target off-tumor effect of mWT CAR and mLiCAR was evaluated by the B cell aplasia level. Peripheral blood B cells from mWT CAR T-cells/UCNPs (Fig. 4c) or mLiCAR T-cells/UCNPs/NIR pulse (Fig. 4d)-treated mice bearing B16-OVA/B16-OVA-mCD19 tumors were counted and compared on day 0 and day 3. B cells from peripheral blood of healthy mice were used as a control. **$P$ < 0.01 when compared to day 0 group (paired two-tailed Student's *t-test;* n = 4; mean ± s.e.m.). (**f**) H&E staining images of major organs (heart, liver, spleen, lung, and kidney) of mLiCAR T-cells/UCNP treated mice bearing B16-OVA/B16-OVA-mCD19 tumors (lower panel) or PBS-injected healthy mice (upper panel). Scale bar, 100 µm.

As a tight control, defective mLiCAR T-cells did not show detectable antigen/light-dependent changes (**I + D5; Fig. 31b**).

Next, similar to the human LiCAR system, we again assessed the ability of anti-mCD19 WT CAR or LiCAR-transduced T cells to eradicate antigen-specific melanoma tumor masses. We performed *in vivo* experiments with intradermal melanoma models, in which tumor cells bearing the non-cognate antigen (B16-OVA) or the cognate antigen (B16-OVA-mCD19) were inoculated into each flank of the same C57BL/6J mouse (**Fig. 31c-d**). After 9 days of tumor establishment, the tumor sites were injected with either mWT CAR T-cells /UCNPs (**Fig. 31c**) or mLiCAR CD8+ T cells/UCNPs (2 x $10^6$ and 150

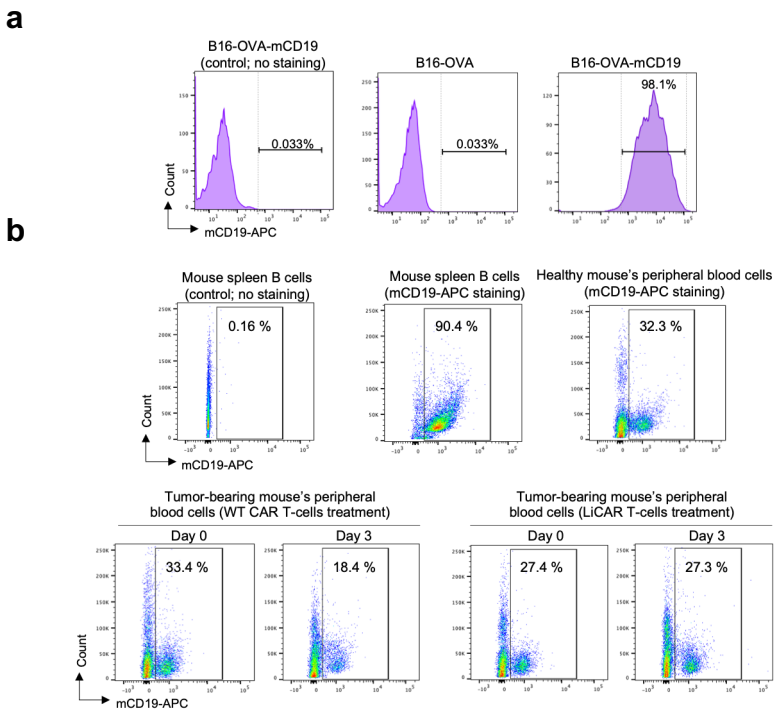


**Figure 32: Melanoma cells expressed mouse CD19 antigen and B cells quantification.**
(**a**) Quantification of mCD19 expression in melanoma cells (B16-OVA) and melanoma cells exogenously expressing mouse CD19 (B16-OVA-mCD19). (**b**) Representative peripheral blood B cell populations from mWT CAR T cells/UCNPs (Fig. 21c) or mLiCAR Tcells/UCNPs/NIR pulses (Fig. 21d)-treated mice bearing B16-OVA/B16-OVA-mCD19 tumors on day 0 and day 3. B cells from peripheral blood of healthy mice were used as a control for normal B cell level. B cells isolated from spleens were stained with anti-CD19-APC (positive control) and non-stained B cells (negative control) were used to aid in gating the cell populations.

μg of UCNPs) (**Fig. 31d**). Pulsed NIR light stimulation for 10 days (980 nm at a power density of 250 mW/cm$^2$; 2 h/day; pulses of 20 sec ON + 5 min OFF) was applied to the mLiCAR/UCNP group only. Both WT CAR and mLiCAR T-cells exhibited tumor antigen-specificity by suppressing tumors composed of B16-OVA-mCD19, but not B16-OVA cells (**Fig. 31c-d**) indicated by the inhibition of B16-OVA-mCD19 tumor growth in the right flank, while mCD19-negative B16-OVA tumors on the left flank remained unaffected.

B cell aplasia (low number or absence of B cells) is one of the life-threatening acute toxicities in CD19-specific CAR T cell therapy due to the nonspecific expression of CD19 on both B cell malignant clones and nonpathogenic B cells. This “on-target/off-tumor” side-effect results in B-cell aplasia, which may require a combination treatment with empiric immunoglobulin replacement[115]. In order to evaluate the B cell aplasia level, we compared the number of B cells from peripheral blood between the mWT CAR T cells/UCNPs (mice from **Fig. 31c**) and the mLiCAR T cells/UCNPs/NIR (mice from **Fig. 31d**) treatment groups both the day before T cell implantation (day 0) and after 3 days (**Fig. 31e**). The results showed that mWT CAR T-cell treatment triggered B cell aplasia after 3 days by reducing both B cell number and B cell percentage in the peripheral cell population (**Fig. 31e and Fig. 32b**), suggesting that the controllable LiCAR system can attenuate undesired “on-target, off-tumor” toxicity. Additionally, we also collected the major organs including heart, liver, and kidney, and performed H & E staining to evaluate the changes in histology. The result suggested that mLiCAR T-cells did not attack other organs (**Fig. 31f**).

Another prevalent adverse effect following CAR T cell treatment is the activation of a cytokine storm associated with large-scale immune responses, known as CRS,

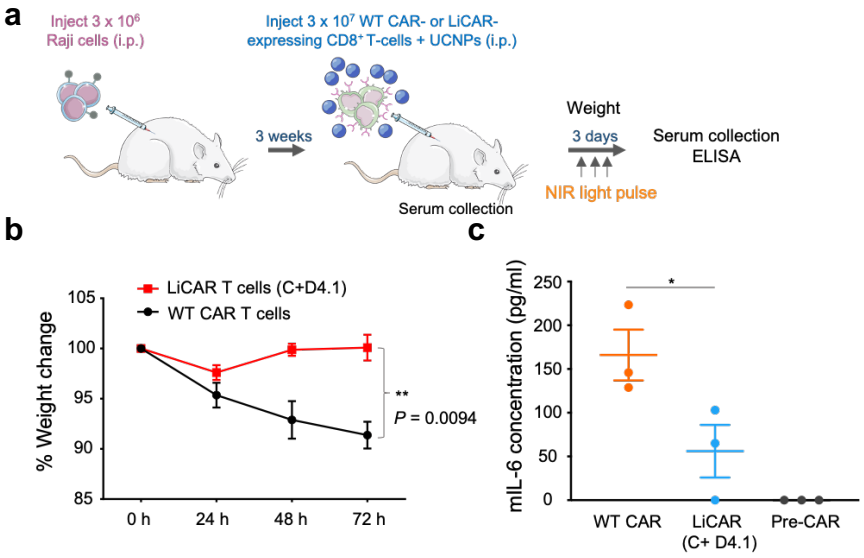


**Figure 33: CAR T-cells and cytokine release syndrome (CRS).**
(**a**) Schematic of the CRS experimental setup. Raji tumor cells ($3x10^6$) were injected (i.p.) into SCID-beige mice. After tumor growth for 3 weeks, WT CAR T-cells/UCNPs or LiCAR T-cells/UCNPs cells were subsequently implanted to the tumor cell-injected sites. LiCAR-treated mice were subjected to pulsed NIR light stimulation for 3 days (980 nm at a power density of 250 mW/cm2; pulses of 20 sec ON, 5 minutes OFF; 2 h/day). Weight change was monitored every day. On day 0 (pre-CAR) and day 3, blood/serum was collected from the retro-orbital sinus by glass capillary from anesthetized mice. (**b**) Weight change of WT CAR T-cells/UCNPs or LiCAR T-cells/UCNPs/NIR-treated mice bearing Raji tumors. Weight of each mouse was normalized to the starting point before CAR T-cell implantation. $^{**}P < 0.01$ when compared to WT CAR T-cells group at 72 h (paired two-tailed Student's *t-test;* n = 3; mean ± s.e.m.). (**c**) Serum levels of mIL-6 at 72h after WT CAR T-cells/UCNPs or LiCAR T-cells/UCNPs/NIR treatment or before CAR T cell injection (Pre-CAR) were quantified by ELISA. $^{*}P < 0.05$ when compared to WT CAR T-cells group (paired two-tailed Student's *t-test;* n = 3; mean ± s.e.m.)

which is characterized by severe clinical syndromes including fever, hypotension, neurological changes, multi-organ failure, and potentially leading to death[116]. A dramatic elevation of IL-6 cytokine is one of the critical hallmarks of CRS, alongside elevated

granulocyte macrophage colony-stimulating factor (GMCSF), IFN-γ and IL-10[117,118]. To evaluate the extent of CRS in our system, we adapted the model of CAR T-cell-induced CRS in SCID-Beige mice from Giavridis, et al. [119] We injected (i.p.) large numbers of Raji tumor cells ($3x10^6$) and allowed tumor growth for 3 weeks. After that, a large number of hWT CAR T cells or hLiCAR T/UCNPs cells ($3x10^7$ cells) were subsequently implanted into the tumor site (**Fig. 33a**). LiCAR-treated mice were subjected to pulsed NIR light stimulation for 3 days (980 nm at a power density of 250 $mW/cm^2$; pulse of 20 sec ON, 5 minutes OFF; 2 h/day). Besides weight monitoring for 3 days, serum was collected on day 0 and day 3 and subjected to serum cytokine analysis (mIL-6). The results showed that after 3 days, the mice treated with WT CAR T cells experienced significant weight loss (**Fig. 33b**). Furthermore, the level of mIL6 was higher in the tumor-bearing mice injected with WT CAR T-cells compared to those injected with LiCAR T cells/UCNPs under NIR pulsed light (**Fig. 33c**), suggesting that the LiCAR approach can mitigate cytokine release syndrome.

**Conclusion and Discussion**

To sum up, we have demonstrated the successful design of photoswitchable CARs to deliver a dual input (antigen + photon)-gated immune response using engineered therapeutic T cells. LiCAR enables light control over the therapeutic activity of CAR T-cells by simply varying the duration of light illumination *in vitro*. Depending on the readouts and LiCAR system choices (among C + D4, C + D4.1, or C + D4.3), we observed some undesired leakage in the dark with LiCAR (C + D4). Conversely, variants lacking detectable leakage sacrifice a certain level of maximal T cell activity

under light stimulation. For maximizing cancer killing, C + D4 shows the best light and antigen synergy with the highest activity upon illumination. Even though there is background NFAT activity (due to the hypersensitivity of this synthetic reporter) and expression of the early response marker CD69 in C + D4, the background activity is not strong enough to trigger T cell cytokine secretion or cytotoxic responses. For purposes requiring tighter control, either C + D4.1 or C + D4.3 can be used. With three options, including strong and weaker versions, we believe LiCAR provides a more dynamic system adaptable to the purposes of different studies. Furthermore, in conjunction with injectable and imaging-guided post-treatment removable upconversion nanoplates, LiCAR permits time- and location-specific CAR T cell-mediated antitumor activity via deep tissue penetrable NIR light *in vivo*. Because this strategy allows for precise spatiotemporal regulation of the T cell-mediated immune response as well as mitigating the side effects associated with immunotherapy such as “on-target, off-tumor” cytotoxicity and CRS toxicity, we anticipate that it can ultimately lead to the development of new generations of personalized optogenetic immunotherapy, where the timing, location, and dosage of T cell-mediated therapeutic activity can be tailored to the patients’ needs.

# CHAPTER IV
# CHEMOGENETIC CONTROL OF T LYMPHOCYTES BY DESIGNER RECEPTORS EXCLUSIVELY ACTIVATED BY DESIGNER DRUGS (DREADDS)

## Introduction

G-protein coupled receptors (GPCRs) are major clinical drug targets and can be used as chemogenetic tools. As many GPCRs share common structures and are extremely diverse, ligands acting on one GPCR may also have “off-target” effects on other molecular targets[53]. Therefore, designer GPCR receptors exclusively activated by designer drugs (DREADD) becomes a powerful approach to investigate various biological questions and disease mechanisms as well as remote and transient manipulation of cellular activity. One of the first attempts at engineering GPCRs was mutating Asp113 in the $\beta_2$-adrenergic receptor to enable binding of a synthetic ligand, but it needed a high dose of synthetic ligands to be activated ($EC_{50} \geq 40$ μM), which limits this design in further *in vivo* studies. Several RASSLs have been generated based on the Serotonin 5-$HT_{2A}$ receptor[120], the melanocortin-4 receptor (MC4R)[121], the H1-histamine receptor[122], and others. However, the synthetic compounds used for these RASSLs also exhibit discernable affinities for the corresponding native receptors[53]. A new generation of RASSLs, DREADDs are a family of mutated GPCRs such as the muscarinic, k-opioid, and the FFA2 fatty acid GPCRs. Typically, the most routinely used chemogenetic tools in neuronal studies is muscarinic acetylcholine receptors (mAChR), which is designed to be activated by clozapine-N-oxide (CNO) and is unresponsive to acetylcholine. Several DREADDs were created by random mutagenesis (Y3.33C/A5.46G) of human mAChR including hM1Dq, hM2Di, hM3Dq, hM4Di, and

hM5Dq[54,123]. The $G\alpha_q$-coupled DREADD (hM3Dq) is most frequently used to enhance neuronal activity[124] as a result of PLC activation and intracellular calcium rise, while hM2Di and hM4Di couple to $G_{\alpha i}$ proteins and inhibit neuronal activity[123] via inhibition of synaptic neurotransmitter release. Besides neuronal activation, hM3Dq also triggers effects on beta-cell functions when expressed in pancreatic beta-cells[125]. hM1Dq and hM5Dq couple to $G_{\alpha}$.

As key secondary messengers, $Ca^{2+}$ and cAMP play essential roles in signal transduction pathways by controlling the function of immune cells, muscle cells, and neurons. Precise control over intracellular calcium and cAMP signals, therefore, is essential for maintaining proper physiological processes. Here, we aim use DREADDs to understand the role of specific GPCR signaling in regulating calcium and cAMP signaling in T lymphocytes. We analyzed the effect of different DREADD ligands on cell response and evaluated the activity of DREADDs in Jurkat T cells. As we demonstrate in this study, upon exposure to these ligands, Gq-linked DREADD was most effective in eliciting calcium mobilization and the nuclear entry of NFAT in mammalian cells, while Gs DREADD triggered cAMP production leading to expression of T cell negatively regulatory genes. In summary, DREADD technology can be harnessed to probe different signaling pathways and thereby modulate the activity of T lymphocytes. Follow-on studies will provide insights into the translational potential of DREADDs-engineered immune cells as immunomodulatory agents to benefit intelligent cell-based therapies against cancer and autoimmune disorders.

## Materials and Methods

### *Molecular Cloning and Plasmid Construction*

To construct plasmids encoding DREADDs-Gi-mCh, Gq-mCh, and Gs-mCh, we amplified Gi (#45548; Addgene), Gq (#345547; Addgene), or Gs (#45549; Addgene) via standard PCR with KOD Hot Start DNA polymerase (EMD Millipore, Burlington, Massachusetts, USA), and then inserted them between HindIII-BamHI or NheI-BamHI restriction sites upstream of mCherry in the pmCherry2-N1 vector (#54517; Addgene). For viral transduction, the lentiblast lentiviral vector (#61425; Addgene) was used as the backbone into which Gi-mCh, Gq-mCh, and Gs-mCh were inserted between two modified restriction enzyme sites, HpaI and PacI. The helper plasmids including the PsPax2 viral packaging vector (#12260; Addgene), an envelope vector pMD2.G (#12259; Addgene) were all acquired from Addgene.

### *Mammalian Cell Culture, Transfection and Fluorescence Microscopy*

HeLa cells from ATCC (#CCL-2) were maintained in Dulbecco's Modified Eagle Medium (DMEM) (#MT10013CV, Thermo Fisher Scientific) supplemented with 10% FBS, 100 units/ml penicillin and 100 µg/mL streptomycin (Gibco) at 37 °C in a humidified atmosphere under 5% $CO_2$. For confocal imaging and measurement of $Ca^{2+}$ influx, $10^5$ cultured cells were seeded on 35 mm glass-bottom dishes. After 24 h, DREADD construct DNA (500 ng) and Gcamp6 (600 ng) were co-transfected into HeLa cells using Lipofectamine 3000 (Life Technologies; Carlsbad, California, USA) according to the manufacturer’s instructions. Confocal imaging was performed at 24 h post-transfection by using an inverted Nikon Eclipse Ti-E microscope customized with

Nikon A1R+ confocal laser sources (405/488/561/640 nm). A 488-nm laser was used to excite GFP and a 561-nm laser was used to excite mCherry fluorescence at intervals of 1−5 s. mCherry-positive cells were selected to calculate the cytosolic fluorescence intensity at selected areas before and after adding drugs or compounds ($\Delta F/F_0$).
In order to evaluate the nuclear translocation of NFAT-GFP, we generated Hela stable cell lines with co-expression of the DREADD-mCh construct and NFAT-GFP construct. The cells were then time-lapse recorded for more than 30 min at intervals of 2 min under a confocal microscope (Nikon Eclipse Ti-E). Both GPF and mCherry-positive cells were selected to calculate the ratio of fluorescence signal between nuclei and the total fluorescence (nuclei plus cytosolic intensities) before and after adding drugs or compounds.

An NFAT-dependent luciferase reporter (NFAT-Luc) Jurkat cell line was used to examine NFAT-dependent gene transcription as previously described[15]. Human cancer cell lines (K562 myelogenous leukemia cells (#CCL-243), Daudi (#CCL-213) and Raji cell lymphoblasts (#CCL-86)) were purchased from the American Type Culture Collection (ATCC, Manassas, Virginia, USA), and cultured in Roswell Park Memorial Institute (RPMI 1640) medium with L-glutamine (#MT10040CV, Thermo Fisher Scientific, Waltham, Massachusetts, USA) supplemented with 10% FBS, 100 units/ml penicillin and 100 µg/mL streptomycin (Gibco, Big Cabin, Oklahoma, USA).

### *Viral Transduction of HeLa, HEK293T, and Jurkat T cells*

Lentiviruses encoding DREADDs-mCh were packaged in HEK293T cells (#CRL-3216; ATCC) transfected with the corresponding lentiviral vector Lentiblast, PsPax2

viral packaging vector (#12260; Addgene) and an envelope vector pMD2.G (#12259; Addgene) using the iMFectin DNA Transfection Reagent (#I7200-101; Gendepot, Katy, Texas, USA). The supernatant containing packaged viruses was collected twice at 48 hours and 72 hours after transfection.

Cultured Hela or Jurkat T cells at a concentration of $10^5$ cells/ml were co-incubated with 2 ml of the 0.45 µM filtered virus supernatant and 10 µg/ml of polybrene per well in a 12-well plate format. Plates containing cultured cells were centrifuged at 2000 x g for 2 hours at 32 °C and incubated 2 more hours at 37°C. The viral supernatant was removed and replaced with fresh DMEM medium (for Hela cells) or RPMI medium (for Jurkat cells) supplemented with 10% FBS, 100 units/ml penicillin and 100 µg/mL streptomycin. Cells were repeatedly transduced four times to yield a higher transduction efficiency.

***In Vitro Quantification of NFAT-Luciferase (NFAT-Luc) Reporter Activity of Jurkat-Luc T cells***

Jurkat-Luc T cells expressing DREADD constructs ($10^5$ cells/well) were treated with drugs/compounds at indicated concentrations or Jurkat-Luc T cells co-expressing DREADD constructs and WT CAR constructs were engaged with cognate CD19-positive Raji cells or non-cognate CD19-negative K562 cells at the ratio of 1:3 in a 96-well flat-bottom microplate (#E17073EF; Greiner Bio-one, Monroe, North Carolina, USA). Plates with cells were incubated at 37 °C in a humidified atmosphere under 5% $CO_2$ and treated with drugs/ compounds for up to 8 hours. Cell pellets were then harvested, and luciferase activity was assayed by using the Dual Luciferase Reporter

Assay System (Promega, Fitchburg, Wisconsin, USA) on the Cytation 5 luminescence microplate reader (BioTek, Winooski, Vermont, USA). Data plots were generated by using Prism version 8.0.0 software (GraphPad, San Diego, California, USA).

## Results

### *Using DREADDs to modulate calcium signaling in T cells*

Clozapine N-oxide (CNO) has been long used as an exclusively synthetic ligand of DREADD. We, therefore, set out to express DREADDs in HeLa cells to probe the role of different G protein subunits in regulating calcium signaling. In order to do that, we co-expressed Gi-mch/Gq-mch/Gs-mch with GCaMP6s in Hela cells and identified the best performing construct based on two criteria: absence of background activity (before CNO

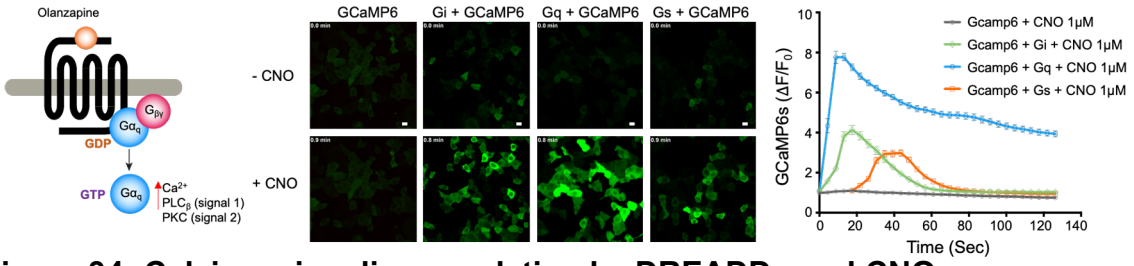


**Figure 34: Calcium signaling regulation by DREADDs and CNO.** **(a)** Schematic illustrating the mechanism of the $G\alpha_q$ activity. (**b**) CNO-induced changes in the GCaMP6s fluorescence intensity in HeLa cells expressing the indicated DREADD constructs. (c) Time course showing quantification of GCaMP6s signals. Data were showed as mean ± s.e.m (n > 30). Scale bar: 5 μm.

treatment) and enhanced dynamic range of calcium signal changes in response to CNO. The results showed that at the same dose of 1 μM CNO, all DREADD constructs (Gi, Gq, and Gs) induced a $Ca^{2+}$ influx, of which Gq was the most potent (**Fig. 34**). As mentioned in chapter II, NFAT is a direct downstream transcription factor of $Ca^{2+}$

signaling. We next examined the NFAT translocation induced by different DREADD constructs in the presence of CNO by using stable cell lines co-expressing NFAT-GFP and either Gi-mCh, Gq-mCh or Gs-mch (**Fig. 35**). Only cells expressing NFAT-GFP and Gq-mCh underwent rapid NFAT translocation from the cytosol to nuclei in response to

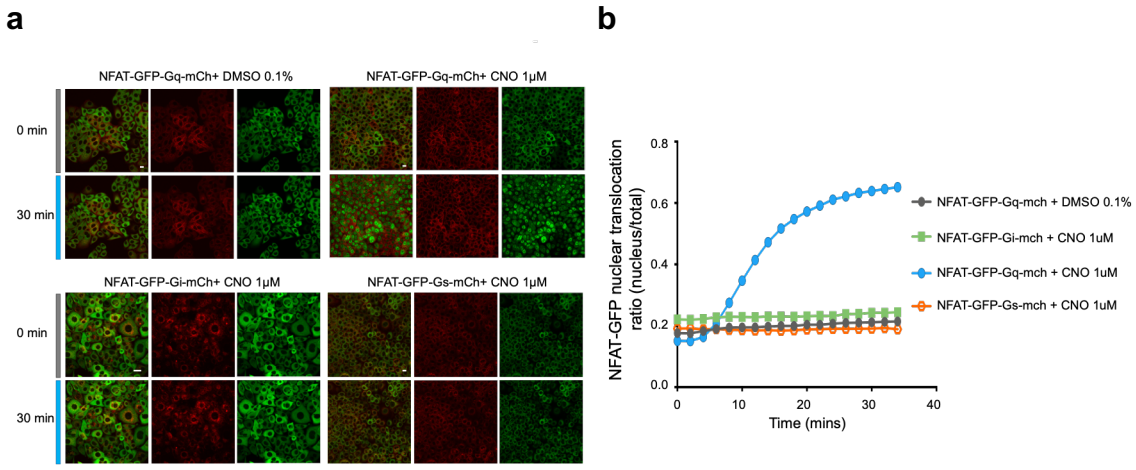


**Figure 35: NFAT translocation induced by different DREADD constructs and CNO.**
(**a**) Monitoring CNO induced translocation of $NFAT_{1-460}$-GFP from cytosol to nuclei in the same field of cells expressing the indicated constructs by confocal imaging. (**b**) Quantification of signals before and after adding drug for 35 min. Data were showed as mean ± s.e.m (n > 66). Scale bar: 5 μm

CNO, while in Gi and Gs cells, NFAT remained exclusively in the cytosol suggesting that the calcium influx induced by CNO in Gi and Gs (**Fig. 34**) was not strong enough to drive nuclear entry of NFAT. This is reasonable since $G\alpha_q$ family G proteins bind to and activate phospholipase C (PLC) to ultimately trigger calcium efflux from the endoplasmic reticulum and subsequently induce $Ca^{2+}$ influx via SOCE process, while $G\alpha_s$ and $G\alpha_i$ are involved in cAMP regulation.

***The function of DREADDs and CNO analogs in regulating NFAT translocation***CNO has been widely used as most popular ligand for many DREADDs studies in neuroscience as it was assumed to be inert to the endogenous acetylcholine (ACh)

**a**

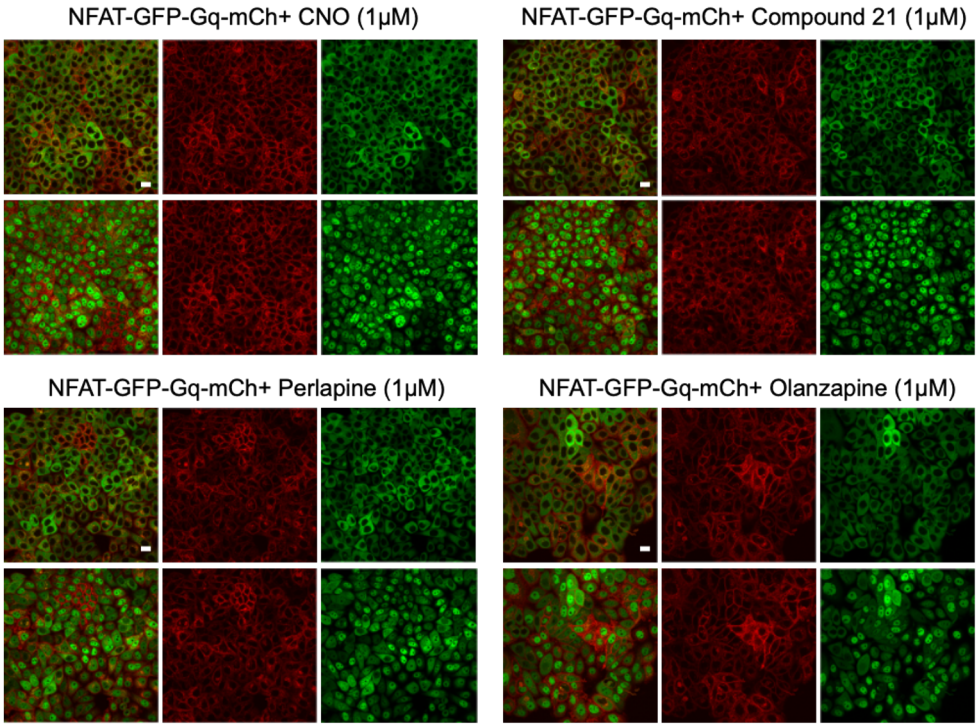


**Figure 36: DREADDs and CNO analogs regulate NFAT translocation**
(**a**) Monitoring DREADD ligand-induced translocation of $NFAT_{1-460}$-GFP from cytosol to nuclei in the same field of cells expressing Gq-mCh by confocal imaging. Scale bar: 5 μm.

receptor and to non-DREADDs receptors[123,126]. However, recently there have been many concerns raised by the use of CNO due to the report that CNO can be back metabolized to its parent compound clozapine, an antipsychotic medicine, in different species[126-130]. This drug can cross the blood-brain barrier[131] and is highly efficient in treatment-resistant schizophrenia[132], but also causes several physiological and behavioral effects such as headache, vertigo, tremo, leukopenia, hypotension,

**b**

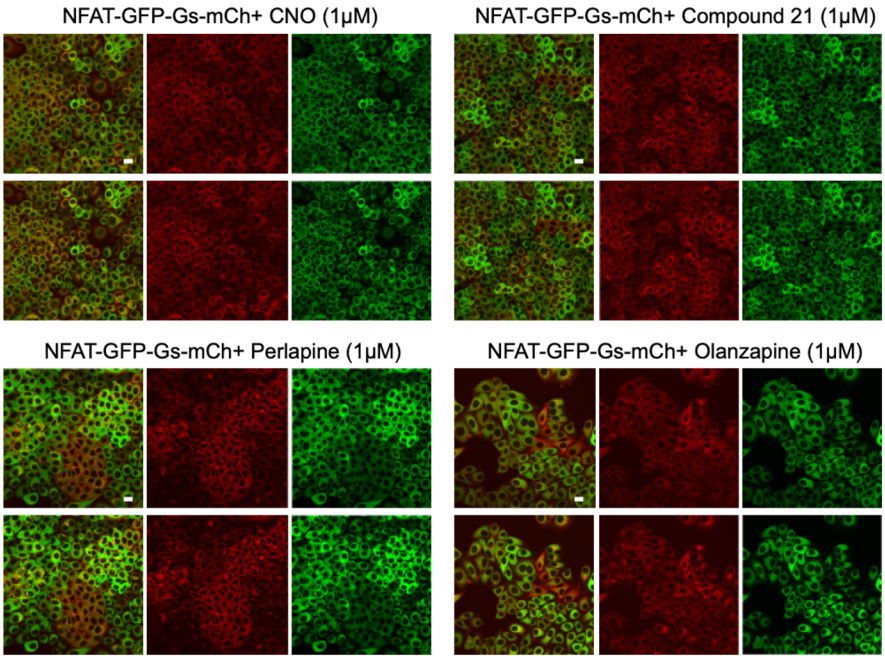


**c**

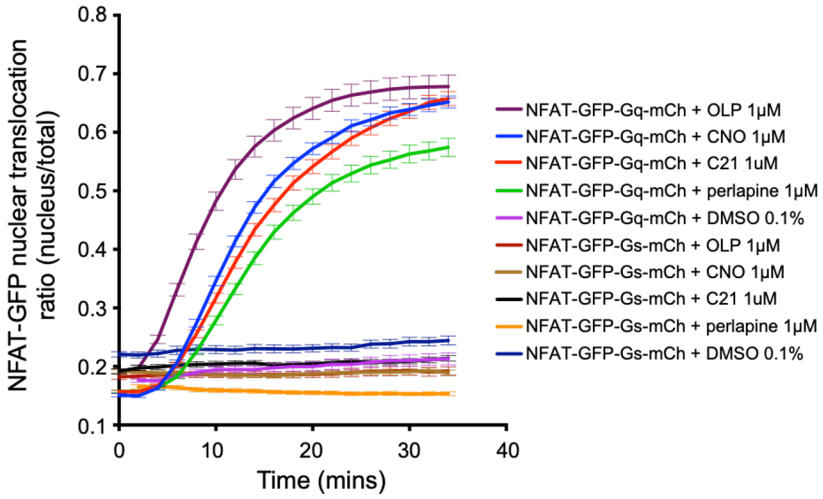


**Figure 36 (continued)**: (**b**) Monitoring DREADDs ligands induced translocation of $NFAT_{1\text{-}460}$-GFP from cytosol to nuclei in the same field of cells expressing Gs-mCh by confocal imaging. (**c**) Quantification of signals before and after adding drugs for 35 min. Data were showed as mean ± s.e.m (n > 70). Scale bar: 5 μm

nausea[133] or even fatal side effects[134]. Furthermore, the back conversion of CNO triggers difficulties in designing *in vivo* studies as the administration dose varies among

the species, strain or sex. CNO has not been approved for clinical use thus far. We, therefore, explored the use of alternative chemical actuators of muscarinic-based DREADDs including DREADD agonist 21 (C21) (11-(1-piperazinyl)-5*H*-dibenzo[*b*,*e*][1,4]diazepine)[135,136], Perlapine, or Olanzapine (**Fig. 36**). C21 can activate both hM4Di inhibitory (Gi) and hM3Dq (Gq) excitatory DREADDs in Chinese hamster

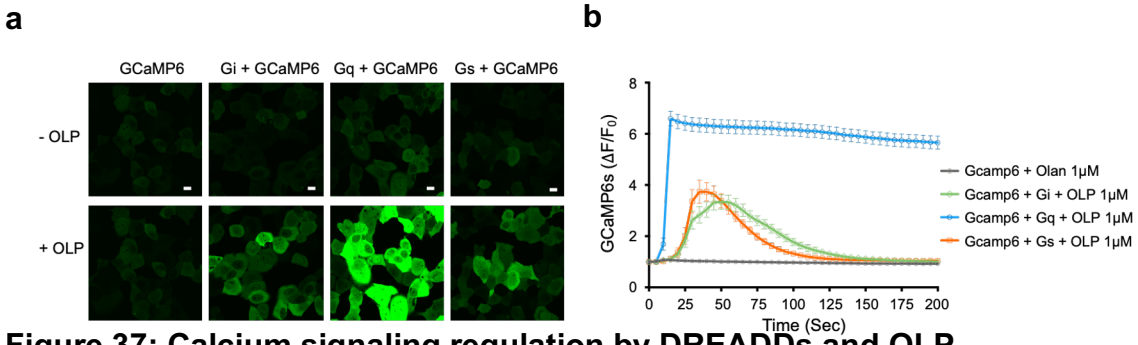


**Figure 37: Calcium signaling regulation by DREADDs and OLP.** (**a**) OLP-induced change in the GCaMP6s fluorescence intensity in HeLa cells expressing the indicated DREADDs constructs. (b) Time course showing quantification of GCaMP6s signals. Data are shown as mean ± s.e.m (n > 32). Scale bar: 5 μm.

ovary (CHO) cells and has a weak binding affinity to wildtype hM1 ($pK_i$ = 5.97 ± 0.05, *n* = 7) and hM4 receptors ($pK_i$ = 5.44 ± 0.11, n = 3)[135]. By using a near genome-wide screen that tested 318 nonolfactory GPCRs, C21 was reported to have a minimal off-target effects which only activated the M4-, D2-, and H4-histamine receptors. C21 has favorable pharmacokinetic properties with 95.1% plasma protein binding (4.7% unbound) and 95% brain protein bounding (4.9% unbound) and does not undergo back-metabolization to clozapine[135]. However, C21 displayed excellent brain penetration, which is not beneficial to our immune cell study.  Perlapine is a drug approved in Japan

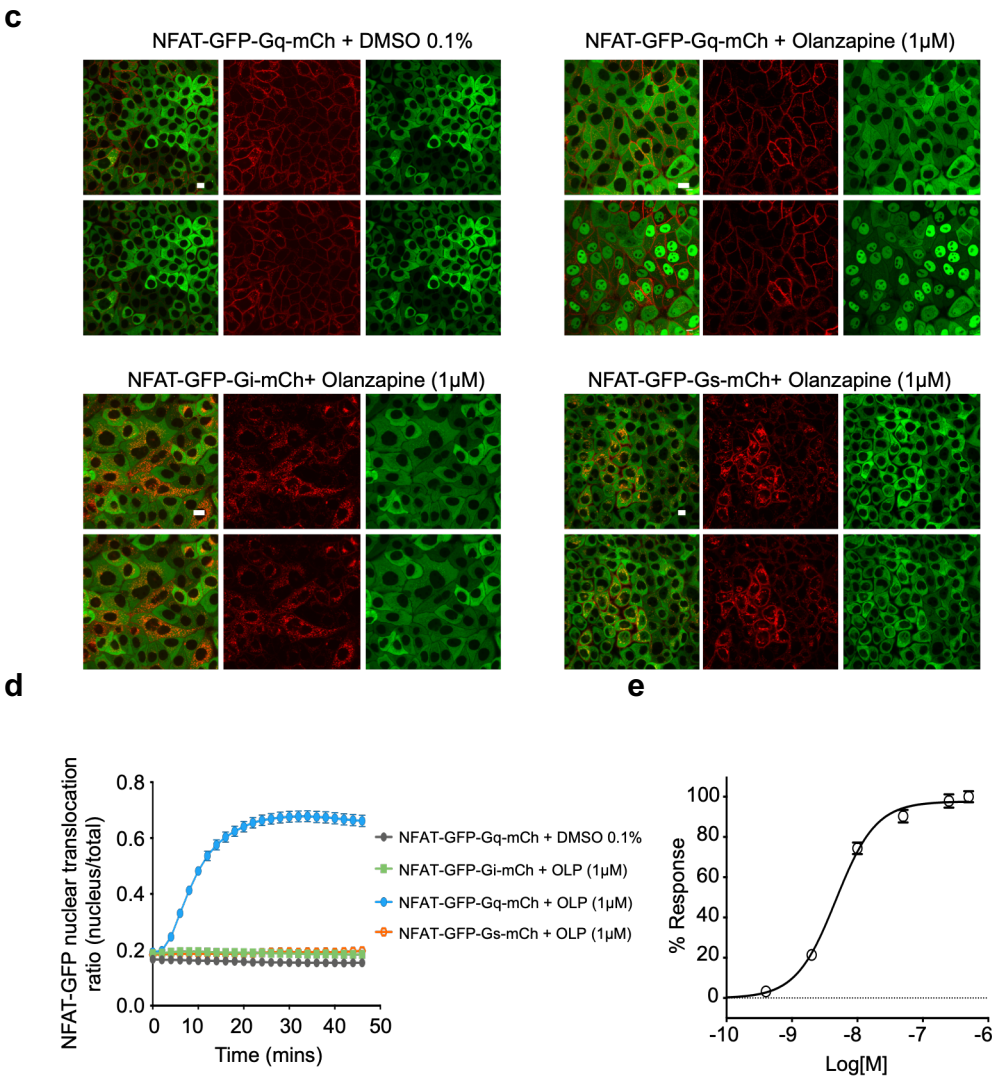


**Figure 37 (Continued)**: (**c**) OLP induced translocation of NFAT$_{1\text{-}460}$-GFP from cytosol to nuclei in the same field of cells expressing indicated DREADD constructs by confocal imaging. (**d**) Quantification of signals before and after adding drugs for 45 min. Data are shown as mean ± s.e.m (n > 43). Scale bar: 5 μm. (**e**) $EC_{50}$ determination of OLP.

as a soporific in humans[137]. Perlapine is strongly selective for activating hM3Dq (EC50 = 2.8 nM) compared to wild type muscarinic receptors (EC50 > 30.000 nM)[136]. Both C21 and Perlapine showed at least 10-fold lower affinity for the majority of GPCRs tested than that seen for the muscarinic DREADDs[135]. Even though Perlapine showed some moderate affinity for a few biogenic amine receptors such as 5-HT2A, 5-HT6, 5-

HT7, and D4, it has a long history of safety in humans[137]. The off-target actions of perlapine *in vivo* still need to be investigated, and not yet being approved by the FDA or European Medicines Agency[138] and hence may restrict its clinical translation potential. Olanzapine (OLP) is an FDA-approved atypical antipsychotic, which is used to treat schizophrenia, bipolar disorder, depression, or hallucinations. Effects of Olanzapine are mediated by antagonism of central serotonin type 2 (5-$HT_{2A}$) and dopamine type 2 ($D_2$) receptors[139]. A recent study describes the use of OLP as a potent activator of hM4D(Gi)-dependent inward-rectifying potassium channels Kir3.1 and Kir3.2 in HEK cells[138]. At the doses used for schizophrenia, OLP also displays some side effects such as weight gain, postural hypotension, or akathisia[138,140]. However, the side effect profile of each activator needs to be further investigated for individual clinical application of DREADDs in this study. OLP is highly lipophilic in nature[139] and its brain penetration is limited by the transmembrane energy-dependent efflux transporter P-glycoprotein (P-gp),[141] making it favorable activator candidate for our DREADDs study in immune cells.

To evaluate the activation of different DREADD ligands including C21, Perlapine, and Olanzapine in controlling calcium signaling of Gq, we again measured the NFAT nuclear translocation in Gq cells, while Gs cells were used as negative control. We used CNO as a positive control ligand to determine the maximal activation of Gq (**Fig. 36a**) and confirmed that OLP, C21, and PLP are all efficacious agonists (maximal activation of NFAT translocation in comparison to CNO: OLP/CNO = 1.04 ± 0.02, *n* = 56; PLP/CNO = 0.8 ± 0.01, *n* = 90; C21/CNO = 1 ± 0.01, *n* = 113). As expected, none of these drugs activate $Ca^{2+}$ signaling in Gs cells (**Fig. 36b-c**). We again confirmed the effect of OLP on calcium influx (**Fig. 37a-b)** and NFAT translocation of different

DREADD construct-expressing cells (**Fig. 37c-d**). Similar to CNO treatment, only Gq could be activated with OLP ($EC_{50}$ = 4.7 nM) (**Fig. 37e**).

***Evaluation of DREADDs-Gq activity via Gq-mCh-cpEGFP sensor***

Besides the evaluation of Gq activity via $Ca^{2+}$ signaling, we explored another tool to directly measure Gq activation. We adapted a well-established genetically encoded G-protein-coupled receptor activation-based sensor for the muscarinic acetylcholine receptors (Ach)[142]. Based on the design of this tool, we inserted a circular permutated

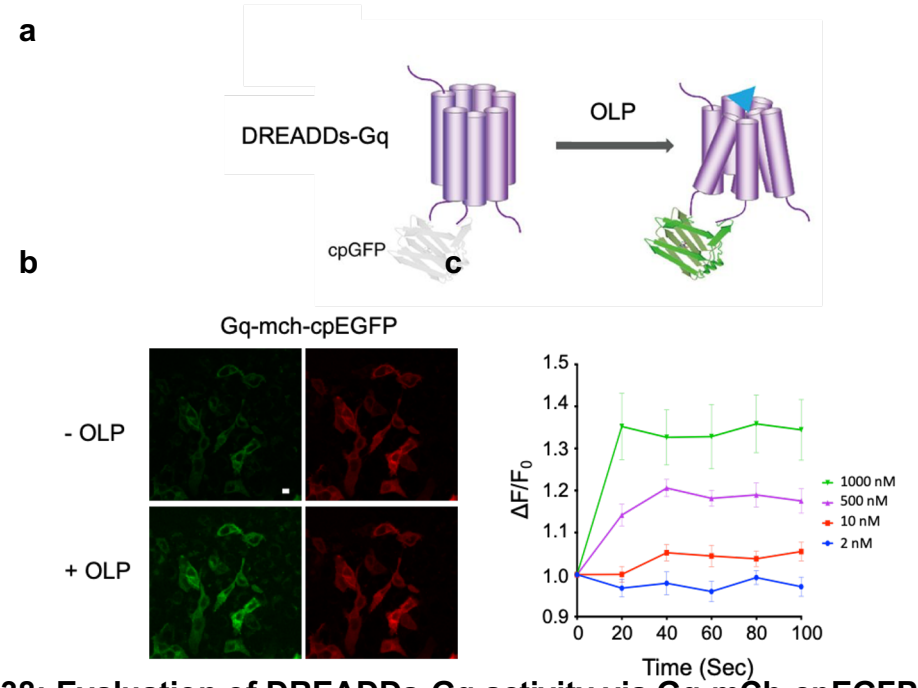


**Figure 38: Evaluation of DREADDs-Gq activity via Gq-mCh-cpEGFP sensor.**
(**a**) Schematic drawing shows the principle of the Gq-mCh-cpEGFP sensor. (**b**) Membrane expression of Gq-mCh-cpEGFP sensor in Hela cells. Scale bar: 5 µm. (**c**) $\Delta F/F_0$ of the Gq-mCh-cpEGFP sensor -expressing cells to different doses of OLP. Data are shown as mean ± s.e.m (n > 14).

green fluorescent protein (cpGFP) into the third intracellular loop ($ICL_3$) of the DREADDs-Gq receptor (**Fig. 38a**). The rationale behind choosing $ICL_3$ was that,

because it connects the transmembrane helices 5 and 6 of muscarinic acetylcholine receptor, it undergoes a conformation change upon ligand binding. The $ICL_3$ from muscarinic acetylcholine receptor was also replaced with a shorter version derived from the $\beta_2$ adrenergic receptor ($\beta_2$AR) to avoid a bulky cpGFP-containing $ICL_3$, which may reduce protein expression and trafficking. After inserting cpEGFP, the Gq-cpEGFP chimera still retained membrane expression in Hela cells (**Fig. 38b**). Upon application of OLP, the fluorescence response increased by up to 36% depending on the dose of OLP, which exhibited drug-tunable activation of Gq activity (**Fig. 38c**). This result

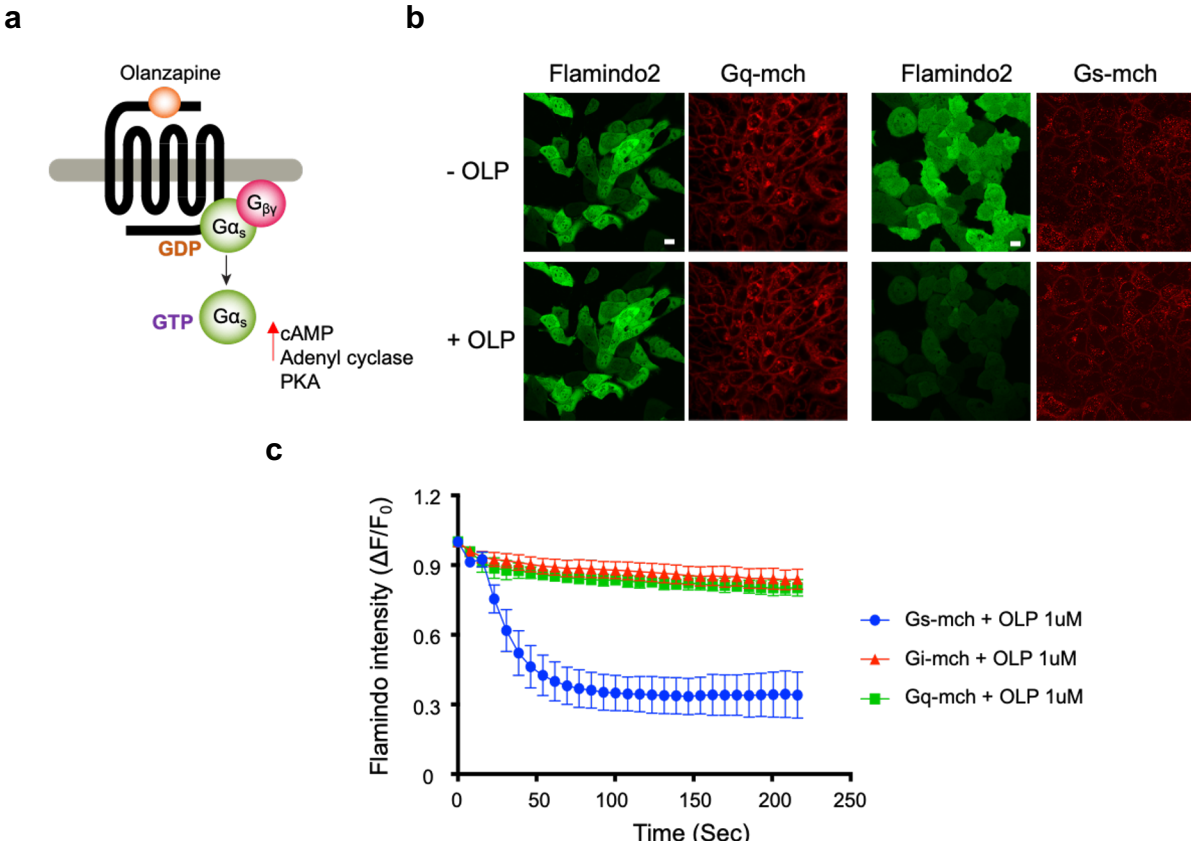


**Figure 39: DREADDs-Gs and Olanzapine in regulating cAMP.**
(**a**) Schematic depiction of the mechanism of the $G\alpha_s$ activity. (**b**) Representative images showing changes in fluorescence intensity by 1 μM OLP application in Flamindo2-Gq-mCh or Flamindo2-Gs-mCh expressing Hela cells. (**c**) Time course of a normalized decrease in Flamindo2 intensity induced by OLP, which increase intracellular cAMP levels. Data were showed as mean ± s.e.m (n > 9). Scale bar: 5 μm.

suggested that we can use this genetically-encoded fluorescence probe to monitor the Gq activity based on the $\Delta F/F_0$ response upon ligand application.

***DREADDs-Gs and Olanzapine in regulating cAMP***

While Gq participates directly in controlling $Ca^{2+}$ signaling in response to ligand engagement, Gs on the other hand regulates the cAMP-dependent signaling pathway. We, therefore, set out to evaluate cAMP production by using the yellow fluorescent indicator for cAMP, Flamindo2[143] (**Fig. 39**). This indicator was constructed based on fluorescence protein-mediated intensiometry, which measures the dynamics of cAMP by changing fluorescence intensity at a single wavelength. In particularly, it consists of Citrine, a yellow fluorescent protein variant and mouse Epac1, a cAMP binding domain inserted in the vicinity of Citrine's chromophore[143]. Upon cAMP binding, Flamindo2 undergoes a conformational change, which in turn induces the alteration of its fluorescence intensity from higher to lower. Our result showed that in the presence of OLP, the Gs stable cell line had a 70% decrease in the Flamindo2 fluorescence signal, while the signal also decreased 20% in Gq cells, which could be caused by fluorescence quenching. This is also one of the drawbacks of using the Flamindo2 indicator.

***The function of DREADDs-Gq and DREADDs-Gs in T cells***

cAMP is known to be a negative regulator of T cell function, which suppresses antigen-induced proliferation and cytokine production via the cAMP/protein kinase A (PKA) signaling pathway[144]. This inhibitory pathway serves to prevent inappropriate

immunoregulation and also maintains homeostasis in T cell. Besides focusing on Gq as a T cell activator, our study also explored the opposing functions of Gs-mediated inhibitory pathways to understand the mechanism of “fine-tuning” immune responses to avoid excessive immune responses. We used Jurkat cells in a NFAT-dependent luciferase (NFAT-Luc) reporter assay to assess the degree of T cell activation[1514]. In human Jurkat-Luc T cells transduced with lentiviruses encoding Gq-mCh and Gs-mCh, we were able to achieve a transduction efficiency of over 99% for both DREADD constructs (**Fig. 40a**). In the presence of OLP, we detected a pronounced titratable response in NFAT-driven reporter bioluminescence in Jurkat-Gq-mCh cells, indicating the activation of engineered T cells. As anticipated, this result is consistent with $Ca^{2+}$ influx and NFAT nuclear translocation of Gq/OLP cells (**Fig. 40b**). In contrast, we did not detect an activation of Gs-mCh cells, which maintained a bioluminescence level equivalent to Jurkat cells (negative control). Collectively, these data indicated the feasibility of using OLP to titrate the activity level of T cells. The NFAT-dependent luciferase assay only showed the inactivation aspect of Gs cells, but did not indicate its inhibition function in T cells. Hence, we moved on to test a few key genes that play crucial roles in both positive (IL-2, CD69, CD25, and c-Fos) and negative regulation (PD-1, CTLA-4, TIM3, and NR4A1) of T-cell activation (**Fig. 40c**). We observed OLP-

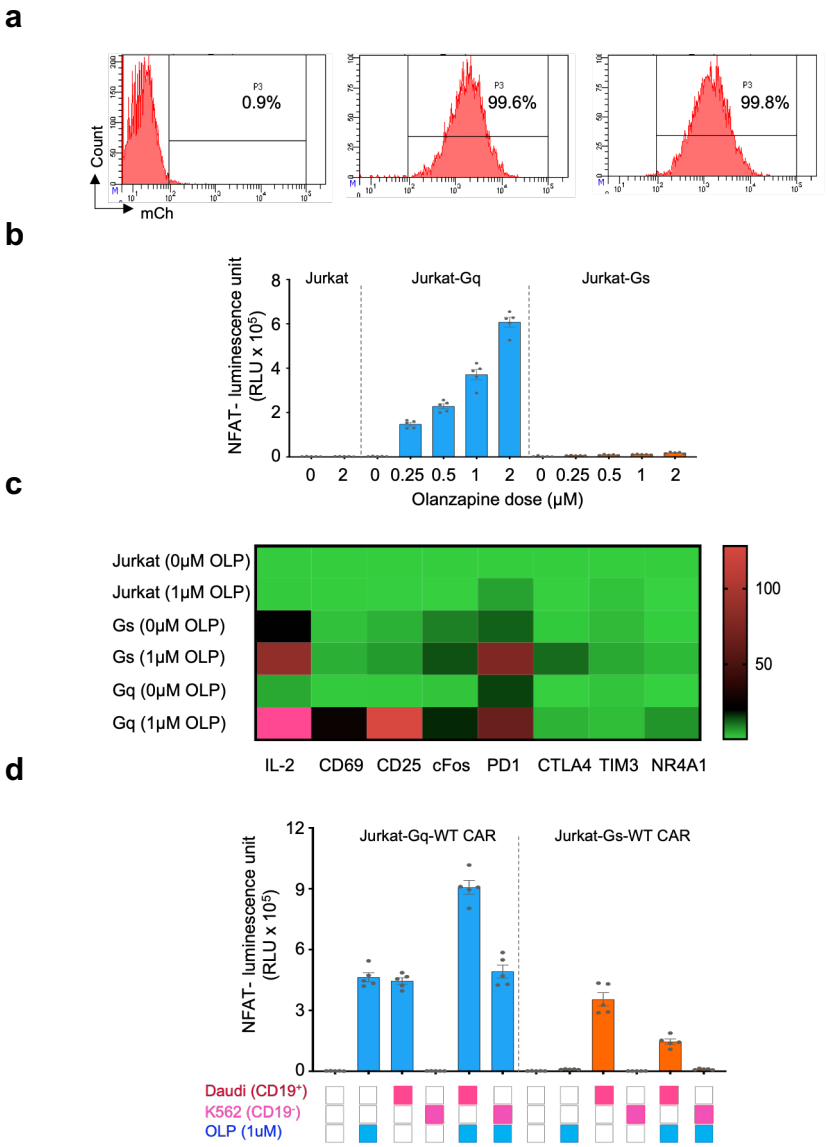


**Figure 40: The function of DREADDs-Gq and DREADDs-Gs in T cells**
(**a**) Quantification of transduction efficiency in Jurkat T cells. Jurkat cells were lentivirally transduced with the Gs-mCh or Gq-mCh. The expression mCherry was determined by flow cytometry. (**b**) NFAT-Luc activity of Gs or Gq expressing Jurkat cells when treated with different doses of OLP. n = 5 (mean ± s.e.m.). (**c**) Gene expression in Jurkat, Gs, or Gq-expressing cells in the absence or presence of 1 μM OLP. (**d**) NFAT-Luc activity of conventional CAR T and indicated DREADDs expressing-cells when co-cultured with either hCD19$^-$ K562 cells or hCD19$^+$ Daudi cells (red box) in the absence (open box) or presence of OLP (blue box). n = 5 (mean ± s.e.m.).

dependent expression of all tested positive regulators including IL-2, CD69, CD25, and c-Fos together with the negative regulators PD-1 and NR4A1 in T cells expressing Gq.

PD-1 was known to mediate inhibitory signals in T cell exhaustion in chronic infections and cancers, but interestingly, it is also transiently expressed during the early phase differentiation of naive CD8 T cells into effector cells[145,146]. Overexpression of NR4A1 inhibits effector T cell differentiation[147]. Nonetheless, several studies have shown that NR4A1 is also rapidly upregulated in peripheral T cells[148-150] and thymocytes[151] following T cell receptor (TCR) signaling, which can explain the phenomenon we observed in Gq-dependent T cell activation. Jurkat cells expressing Gs showed upregulation of all tested negative regulators and two T cell activation molecules including IL-2 and c-Fos even though the degree of expression of these two molecules was not comparable to that observed with Gq cells.

To use the activation and inhibition feature of Gq and Gs in T cells, we further combined these two DREADDs constructs with a conventional CAR (**Fig. 40d**) to either enhance conventional CAR T cell activity for antigen clearance or tune down the strength and viability of T cells to reduce undesired side effects. NFAT-Luc Jurkat T cells co-transduced with lentiviruses encoding WT CAR and either Gq-mCh or Gs-mCh receptors were engaged with human CD19 (hCD19)-negative K562 leukemia cells or hCD19-positive Daudi lymphoma cells. In the dual presence of cognate tumor antigen ($hCD19^+$ Daudi lymphoma cells) and OLP, we detected a two-fold increase in NFAT-driven reporter bioluminescence in Gq-WT CAR T-cells compared to the same cells receiving either antigen or OLP alone. In contrast, Gs-WT CAR T-cells activity is suppressed by a half upon application of both tumor antigen and OLP compared to cells with antigen alone. As an extremely tight control, the engagement of noncognate antigen to Gq/Gs-WT CAR T-cells did not show discernible T cell activation, which is

similar to the group without K562, Daudi, or OLP. This result suggests that depending on the DREADD construct used, the incorporation of DREADDs to T cells would either boost or suppress the strength and viability of these lymphocytes, thereby providing a flexible tool to achieve a specific purpose and avoid side-effects of immune system overreaction.

**Conclusion and Discussion**

To sum up, DREADDs have been popularly used in the neuroscience to understand the cellular signals or circuitry that regulates the behavior, motor functions, and perceptions in difference species[137], and now for the first time being extended to apply in immune cell. We have shown that Gq-linked DREADD was most effective in eliciting calcium mobilization and the nuclear entry of NFAT in mammalian cells in the presence of different DREADD ligands, while DREADD-Gs triggered cAMP production and lead to biased upregulation of negative regulatory genes in T cells. The incorporation of DREADDs to T cells can be used for fine-tuning the immune response in both T cells and CAR T-cells, which will likely pave the way for translational applications of DREADDs in immunotherapies.

# CHAPTER V
# CONCLUSION AND FUTURE DIRECTIONS

In summary, we have generated different optogenetic and chemogenetic tools to enable remote control of transcriptional reprogramming, tumor targeting with high precision as well as regulation of T lymphocyte activity.

In the first part of this study, we developed a chemical or light-inducible transcriptional reprogramming device that combines photoswitchable genetically encoded calcium actuators with dCas9 to control gene expression. By fusing an engineered $Ca^{2+}$-responsive NFAT fragment with dCas9 and transcriptional coactivators, we harnessed the power of light to achieve photoinducible transcriptional reprogramming in mammalian cells. This synthetic system (designated CaRROT) can also be used to document calcium-dependent activity in mammals after exposure to ligands or chemicals that would elicit a calcium response inside cells. The catalytically inactive CRISPR/Cas9 (dCas9), when fused with repressive or activating effectors, functions as a versatile platform to reprogram gene transcription at targeted genomic loci. However, without temporal control, the application of these reprogramming tools will likely cause off-target effects and lack strict reversibility; CaRROT was designed to overcome this limitation.

In the second part of this study, we generated LiCAR T-cells that enable photo-tunable activation of therapeutic T cells to induce tumor cell killing both *in vitro* and *in vivo*. When coupled with imaging-guided, surgically removable upconversion nanoplates that have enhanced near infrared (NIR)-to-blue upconversion luminescence as miniature deep tissue transducers, LiCAR T-cells enable precise spatiotemporal control

over T cell-mediated anti-tumor therapeutic activity with greatly mitigated side effects. This remotely controllable nano-optogenetic device sets the stage for the exploration of smart immunotherapy to deliver personalized anti-cancer therapy. Photo-tunable CAR offers a new exciting opportunity to achieve precise control of T cell activation with a major advantage. Our system is one of the first light-dependent CAR T cell activation systems. Uncontrolled cytokine storm is the main issue for using CAR T cells since their autonomous function inside a patient's circulation constrains the ability to control them. A growing number of strategies have emerged to modulate the proliferation of T cells, their response strength as well as the duration of their activity. Approaches employed by synthetic biologists include using suicide switches, chemically induced-CAR T-cell activation, or a combination of two or more antigens to trigger CAR activity. Nevertheless, among these, the use of chemicals faces undesirable effects on living systems such as cytotoxicity and cellular perturbation due to possible off-target effects. Optogenetics provides a potential new solution by circumventing the limitations of chemical-based methods. Optogenetic approaches show many advantages in terms of spatial and temporal control, tunability, and reversibility. LiCARs will provide the means to control the behavior of specific cells in circulation with respect to amplitude and duration of activation and the tissue site of activation.

In the final part of this study, we used chemogenetic tools that have been widely used by neuroscientists. But for the first time, we repurposed them to modulate lymphocyte cell fate by either boosting T cell activation or suppressing their activity. This study has so far been conducted *in vitro*, but it will open up the opportunity to explore its potential for tumor killing with mitigated side effects *in vivo*.

The preliminary success of each tool opens up new avenues to extend the engineering of photo-inducible transcription device to regulate CAR expression. In order to do that, the CAR would be constructed with several repeats of a guide RNA target sequence located upstream of a minimal promoter. Light/chemical-induced nuclear entry of CaRROT will be directed by small guide RNAs (sgRNAs) to the target sequences in the CAR construct to turn on its transcription.

Sustained illumination is needed to maintain stable heterodimerization of both components in LiCAR T-cells to yield a productive immune response. To avoid potential side effects due to prolonged exposure to blue light, it is most desirable to have a relatively long-lasting deactivation process when returning from light to the dark state. To circumvent this drawback, we will introduce long-lived photocycle mutations into LOV2 (Q513L, N414L/Q513A where $t_{1/2,\ off}$ is 20-30 min vs. 30 sec for WT)[152] or CRY2 (L348F, with $t_{1/2,\ off}$ of about 24 min compared to 5 min for WT)[47,153], to maintain the light state after light withdrawal. These long-lived mutants will reduce the frequency and dose of photo-excitation.

## REFERENCES


1 Pollizzi, K. N. & Powell, J. D. Integrating canonical and metabolic signalling programmes in the regulation of T cell responses. *Nat Rev Immunol* **14**, 435-446, doi:10.1038/nri3701 (2014).

2 Nguyen, N. Z., Y. in *Encyclopedia of Biological Chemistry 3rd Edition* (Elsevier, 2020).

3 Nguyen, N. T. M., G.; Zhou, Y & Jing, J. Optogenetic approaches to control Ca2+-modulated physiological processes. *Current Opinion in Physiology* **17**, 187-196 (2020).

4 Nguyen, N. T., He, L., Martinez-Moczygemba, M., Huang, Y. & Zhou, Y. Rewiring calcium signaling for precise transcriptional reprogramming. *ACS Synth Biol*, doi:10.1021/acssynbio.7b00467 (2018).

5 Clapham, D. E. Calcium signaling. *Cell* **131**, 1047-1058, doi:10.1016/j.cell.2007.11.028 (2007).

6 Hogan, P. G., Lewis, R. S. & Rao, A. Molecular basis of calcium signaling in lymphocytes: STIM and ORAI. *Annu Rev Immunol* **28**, 491-533, doi:10.1146/annurev.immunol.021908.132550 (2010).

7 Berridge, M. J., Bootman, M. D. & Roderick, H. L. Calcium signalling: dynamics, homeostasis and remodelling. *Nat Rev Mol Cell Biol* **4**, 517-529, doi:10.1038/nrm1155 (2003).

8 Ma, G. *et al.* Optogenetic toolkit for precise control of calcium signaling. *Cell Calcium* **64**, 36-46, doi:10.1016/j.ceca.2017.01.004 (2017).

9 Nguyen, N. T. *et al.* CRAC channel-based optogenetics. *Cell Calcium* **75**, 79-88, doi:10.1016/j.ceca.2018.08.007 (2018).

10 Prakriya, M. & Lewis, R. S. Store-Operated Calcium Channels. *Physiol Rev* **95**, 1383-1436, doi:10.1152/physrev.00020.2014 (2015).

11 Soboloff, J., Rothberg, B. S., Madesh, M. & Gill, D. L. STIM proteins: dynamic calcium signal transducers. *Nat Rev Mol Cell Biol* **13**, 549-565, doi:10.1038/nrm3414 (2012).

12 Harper, S. M., Neil, L. C. & Gardner, K. H. Structural basis of a phototropin light switch. *Science* **301**, 1541-1544, doi:10.1126/science.1086810 (2003).

13 Wu, Y. I. *et al.* A genetically encoded photoactivatable Rac controls the motility of living cells. *Nature* **461**, 104-108, doi:10.1038/nature08241 (2009).

14 Ma, G. *et al.* Optogenetic engineering to probe the molecular choreography of STIM1-mediated cell signaling. *Nat Commun* **11**, 1039, doi:10.1038/s41467-020-14841-9 (2020).

15 He, L. *et al.* Near-infrared photoactivatable control of Ca(2+) signaling and optogenetic immunomodulation. *Elife* **4**, doi:10.7554/eLife.10024 (2015).

16 Ishii, T. *et al.* Light generation of intracellular Ca(2+) signals by a genetically encoded protein BACCS. *Nat Commun* **6**, 8021, doi:10.1038/ncomms9021 (2015).

17 Pham, E., Mills, E. & Truong, K. A synthetic photoactivated protein to generate local or global Ca(2+) signals. *Chem Biol* **18**, 880-890, doi:10.1016/j.chembiol.2011.04.014 (2011).

18 Nash, A. I., Ko, W. H., Harper, S. M. & Gardner, K. H. A conserved glutamine plays a central role in LOV domain signal transmission and its duration. *Biochemistry* **47**, 13842-13849, doi:10.1021/bi801430e (2008).
19 Hogan, P. G., Chen, L., Nardone, J. & Rao, A. Transcriptional regulation by calcium, calcineurin, and NFAT. *Genes Dev* **17**, 2205-2232, doi:10.1101/gad.1102703 (2003).
20 Anderson, M. E. & Siahaan, T. J. Targeting ICAM-1/LFA-1 interaction for controlling autoimmune diseases: designing peptide and small molecule inhibitors. *Peptides* **24**, 487-501, doi:10.1016/s0196-9781(03)00083-4 (2003).
21 Garg, A. D. *et al.* Immunogenic cell death, DAMPs and anticancer therapeutics: an emerging amalgamation. *Biochim Biophys Acta* **1805**, 53-71, doi:10.1016/j.bbcan.2009.08.003 (2010).
22 Vesely, M. D., Kershaw, M. H., Schreiber, R. D. & Smyth, M. J. Natural innate and adaptive immunity to cancer. *Annu Rev Immunol* **29**, 235-271, doi:10.1146/annurev-immunol-031210-101324 (2011).
23 Riha, P. & Rudd, C. E. CD28 co-signaling in the adaptive immune response. *Self Nonself* **1**, 231-240, doi:10.4161/self.1.3.12968 (2010).
24 Tai, Y., Wang, Q., Korner, H., Zhang, L. & Wei, W. Molecular Mechanisms of T Cells Activation by Dendritic Cells in Autoimmune Diseases. *Front Pharmacol* **9**, 642, doi:10.3389/fphar.2018.00642 (2018).
25 Smith-Garvin, J. E., Koretzky, G. A. & Jordan, M. S. T cell activation. *Annu Rev Immunol* **27**, 591-619, doi:10.1146/annurev.immunol.021908.132706 (2009).
26 Li, M. O. & Rudensky, A. Y. T cell receptor signalling in the control of regulatory T cell differentiation and function. *Nat Rev Immunol* **16**, 220-233, doi:10.1038/nri.2016.26 (2016).
27 Macian, F., Lopez-Rodriguez, C. & Rao, A. Partners in transcription: NFAT and AP-1. *Oncogene* **20**, 2476-2489, doi:10.1038/sj.onc.1204386 (2001).
28 Brezar, V., Tu, W. J. & Seddiki, N. PKC-Theta in Regulatory and Effector T-cell Functions. *Front Immunol* **6**, 530, doi:10.3389/fimmu.2015.00530 (2015).
29 Chen, L. & Flies, D. B. Molecular mechanisms of T cell co-stimulation and co-inhibition. *Nat Rev Immunol* **13**, 227-242, doi:10.1038/nri3405 (2013).
30 Chmielewski, M., Hombach, A. A. & Abken, H. Antigen-Specific T-Cell Activation Independently of the MHC: Chimeric Antigen Receptor-Redirected T Cells. *Front Immunol* **4**, 371, doi:10.3389/fimmu.2013.00371 (2013).
31 Levine, B. L., Miskin, J., Wonnacott, K. & Keir, C. Global Manufacturing of CAR T Cell Therapy. *Mol Ther Methods Clin Dev* **4**, 92-101, doi:10.1016/j.omtm.2016.12.006 (2017).
32 Gross, G., Waks, T. & Eshhar, Z. Expression of immunoglobulin-T-cell receptor chimeric molecules as functional receptors with antibody-type specificity. *Proc Natl Acad Sci U S A* **86**, 10024-10028 (1989).
33 Kuwana, Y. *et al.* Expression of chimeric receptor composed of immunoglobulin-derived V regions and T-cell receptor-derived C regions. *Biochem Biophys Res Commun* **149**, 960-968 (1987).
34 Sadelain, M., Brentjens, R. & Riviere, I. The basic principles of chimeric antigen receptor design. *Cancer Discov* **3**, 388-398, doi:10.1158/2159-8290.CD-12-0548 (2013).

35 Tan, J. T., Whitmire, J. K., Ahmed, R., Pearson, T. C. & Larsen, C. P. 4-1BB ligand, a member of the TNF family, is important for the generation of antiviral CD8 T cell responses. *J Immunol* **163**, 4859-4868 (1999).
36 Acuto, O. & Michel, F. CD28-mediated co-stimulation: a quantitative support for TCR signalling. *Nat Rev Immunol* **3**, 939-951, doi:10.1038/nri1248 (2003).
37 Chmielewski, M., Kopecky, C., Hombach, A. A. & Abken, H. IL-12 release by engineered T cells expressing chimeric antigen receptors can effectively Muster an antigen-independent macrophage response on tumor cells that have shut down tumor antigen expression. *Cancer Res* **71**, 5697-5706, doi:10.1158/0008-5472.CAN-11-0103 (2011).
38 Grupp, S. A. *et al.* Chimeric antigen receptor-modified T cells for acute lymphoid leukemia. *N Engl J Med* **368**, 1509-1518, doi:10.1056/NEJMoa1215134 (2013).
39 Brudno, J. N. & Kochenderfer, J. N. Toxicities of chimeric antigen receptor T cells: recognition and management. *Blood* **127**, 3321-3330, doi:10.1182/blood-2016-04-703751 (2016).
40 Neelapu, S. S. *et al.* Chimeric antigen receptor T-cell therapy - assessment and management of toxicities. *Nat Rev Clin Oncol* **15**, 47-62, doi:10.1038/nrclinonc.2017.148 (2018).
41 Kochenderfer, J. N. *et al.* B-cell depletion and remissions of malignancy along with cytokine-associated toxicity in a clinical trial of anti-CD19 chimeric-antigen-receptor-transduced T cells. *Blood* **119**, 2709-2720, doi:10.1182/blood-2011-10-384388 (2012).
42 Di Stasi, A. *et al.* Inducible apoptosis as a safety switch for adoptive cell therapy. *N Engl J Med* **365**, 1673-1683, doi:10.1056/NEJMoa1106152 (2011).
43 Wang, X. *et al.* A transgene-encoded cell surface polypeptide for selection, in vivo tracking, and ablation of engineered cells. *Blood* **118**, 1255-1263, doi:10.1182/blood-2011-02-337360 (2011).
44 Fedorov, V. D., Themeli, M. & Sadelain, M. PD-1- and CTLA-4-based inhibitory chimeric antigen receptors (iCARs) divert off-target immunotherapy responses. *Sci Transl Med* **5**, 215ra172, doi:10.1126/scitranslmed.3006597 (2013).
45 Grada, Z. *et al.* TanCAR: A Novel Bispecific Chimeric Antigen Receptor for Cancer Immunotherapy. *Mol Ther Nucleic Acids* **2**, e105, doi:10.1038/mtna.2013.32 (2013).
46 Guntas, G. *et al.* Engineering an improved light-induced dimer (iLID) for controlling the localization and activity of signaling proteins. *Proc Natl Acad Sci U S A* **112**, 112-117, doi:10.1073/pnas.1417910112 (2015).
47 Kennedy, M. J. *et al.* Rapid blue-light-mediated induction of protein interactions in living cells. *Nat Methods* **7**, 973-975, doi:10.1038/nmeth.1524 (2010).
48 Dorsam, R. T. & Gutkind, J. S. G-protein-coupled receptors and cancer. *Nat Rev Cancer* **7**, 79-94, doi:10.1038/nrc2069 (2007).
49 Borges, A., Torrinha, F., Lufkin, R. B. & Abemayor, E. Laryngeal involvement in multiple symmetric lipomatosis: the role of computed tomography in diagnosis. *Am J Otolaryngol* **18**, 127-130, doi:10.1016/s0196-0709(97)90101-0 (1997).
50 Siehler, S. Regulation of RhoGEF proteins by G12/13-coupled receptors. *Br J Pharmacol* **158**, 41-49, doi:10.1111/j.1476-5381.2009.00121.x (2009).

51 Mahoney, J. P. & Sunahara, R. K. Mechanistic insights into GPCR-G protein interactions. *Curr Opin Struct Biol* **41**, 247-254, doi:10.1016/j.sbi.2016.11.005 (2016).
52 Hanlon, C. D. & Andrew, D. J. Outside-in signaling--a brief review of GPCR signaling with a focus on the Drosophila GPCR family. *J Cell Sci* **128**, 3533-3542, doi:10.1242/jcs.175158 (2015).
53 Pei, Y., Rogan, S. C., Yan, F. & Roth, B. L. Engineered GPCRs as tools to modulate signal transduction. *Physiology (Bethesda)* **23**, 313-321, doi:10.1152/physiol.00025.2008 (2008).
54 Roth, B. L. How structure informs and transforms chemogenetics. *Curr Opin Struct Biol* **57**, 9-16, doi:10.1016/j.sbi.2019.01.016 (2019).
55 Dominguez, A. A., Lim, W. A. & Qi, L. S. Beyond editing: repurposing CRISPR-Cas9 for precision genome regulation and interrogation. *Nat Rev Mol Cell Biol* **17**, 5-15, doi:10.1038/nrm.2015.2 (2016).
56 Nihongaki, Y., Yamamoto, S., Kawano, F., Suzuki, H. & Sato, M. CRISPR-Cas9-based photoactivatable transcription system. *Chem Biol* **22**, 169-174, doi:10.1016/j.chembiol.2014.12.011 (2015).
57 Gilbert, L. A. *et al.* CRISPR-mediated modular RNA-guided regulation of transcription in eukaryotes. *Cell* **154**, 442-451, doi:10.1016/j.cell.2013.06.044 (2013).
58 Zhang, F., Wen, Y. & Guo, X. CRISPR/Cas9 for genome editing: progress, implications and challenges. *Hum Mol Genet* **23**, R40-46, doi:10.1093/hmg/ddu125 (2014).
59 Ran, F. A. *et al.* Genome engineering using the CRISPR-Cas9 system. *Nat Protoc* **8**, 27, doi:10.1038/nprot.2013.143 (2013).
60 Hsu, P. D., Lander, E. S. & Zhang, F. Development and Applications of CRISPR-Cas9 for Genome Engineering. *Cell* **157**, 78 (2014).
61 Jinek, M. *et al.* A programmable dual-RNA-guided DNA endonuclease in adaptive bacterial immunity. *Science* **337**, 21 (2012).
62 Perez-Pinera, P. *et al.* RNA-guided gene activation by CRISPR-Cas9-based transcription factors. *Nat Methods* **10**, 973-976, doi:10.1038/nmeth.2600 (2013).
63 Maeder, M. L. *et al.* CRISPR RNA-guided activation of endogenous human genes. *Nat Methods* **10**, 977-979, doi:10.1038/nmeth.2598 (2013).
64 Qi, L. S. *et al.* Repurposing CRISPR as an RNA-guided platform for sequence-specific control of gene expression. *Cell* **152**, 1173-1183, doi:10.1016/j.cell.2013.02.022 (2013).
65 Rost, B. R., Schneider-Warme, F., Schmitz, D. & Hegemann, P. Optogenetic Tools for Subcellular Applications in Neuroscience. *Neuron* **96**, 31, doi:10.1016/j.neuron.2017.09.047 (2017).
66 Cheng, A. W. *et al.* Multiplexed activation of endogenous genes by CRISPR-on, an RNA-guided transcriptional activator system. *Cell Res* **23**, 71, doi:10.1038/cr.2013.122 (2013).
67 Lowder, L. G. *et al.* A CRISPR/Cas9 Toolbox for Multiplexed Plant Genome Editing and Transcriptional Regulation. *Plant Physiol.* **169**, 14, doi:10.1104/pp.15.00636 (2015).

68 Lei, Y. *et al.* argeted DNA methylation in vivo using an engineered dCas9-MQ1 fusion protein. *Nat Commun* **8**, doi:10.1038/ncomms16026 (2017).
69 Larson, M. H. *et al.* CRISPR interference (CRISPRi) for sequence-specific control of gene expression. *Nat Protoc* **8**, 2180-2196, doi:10.1038/nprot.2013.132 (2013).
70 Ji, H. *et al.* Specific Reactivation of Latent HIV-1 by dCas9-SunTag-VP64-mediated Guide RNA Targeting the HIV-1 Promoter. *Mol Ther.* **24**, 13 (2016).
71 Ma, G. *et al.* Optogenetic toolkit for precise control of calcium signaling. *Cell Calcium* **64**, 10, doi:10.1016/j.ceca.2017.01.004 (2017).
72 Ma, G., Wen, S., Huang, Y. & Zhou, Y. The STIM-Orai Pathway: Light-Operated Ca2+ Entry Through Engineered CRAC Channels. *Adv Exp Med Biol* **993**, 21 (2017).
73 Tan, P., He, L., Han, G. & Zhou, Y. Optogenetic Immunomodulation: Shedding Light on Antitumor Immunity. *Trends Biotechnol* **35**, 11, doi:10.1016/j.tibtech.2016.09.002 (2017).
74 Maman, S. *et al.* High rates and positive outcomes of HIV-serostatus disclosure to sexual partners: reasons for cautious optimism from a voluntary counseling and testing clinic in Dar es Salaam, Tanzania. *AIDS Behav* **7**, 373-382 (2003).
75 Niopek, D. *et al.* Engineering light-inducible nuclear localization signals for precise spatiotemporal control of protein dynamics in living cells. *Nat Commun* **5**, 4404, doi:10.1038/ncomms5404 (2014).
76 Wu, Y. I. *et al.* A genetically encoded photoactivatable Rac controls the motility of living cells. *Nature* **461**, 8 (2009).
77 Ma, G. *et al.* Inside-out Ca(2+) signalling prompted by STIM1 conformational switch. *Nat Commun.* **6**, doi:doi: 10.1038/ncomms8826. (2015).
78 Gudlur, A., Zhou, Y. & Hogan, P. G. STIM-ORAI interactions that control the CRAC channel. *Curr Top Membr* **71**, 25, doi:10.1016/B978-0-12-407870-3.00002-0. (2013).
79 Soboloff, J., Rothberg, B. S., Madesh, M. & Gill, D. L. STIM proteins: dynamic calcium signal transducers. *Nat Rev Mol Cell Biol* **13**, 26, doi:10.1038/nrm3414. (2012).
80 Prakriya, M. & Lewis, R. S. Store-Operated Calcium Channels. *Physiol Rev* **95**, 53, doi:10.1152/physrev.00020.2014. (2015).
81 Wang, H. *et al.* LOVTRAP: an optogenetic system for photoinduced protein dissociation. *Nat Methods* **13**, 755-758, doi:10.1038/nmeth.3926 (2016).
82 Sagara, Y. & Inesi, G. Inhibition of the sarcoplasmic reticulum Ca2+ transport ATPase by thapsigargin at subnanomolar concentrations. *J Biol Chem* **266**, 6 (1991).
83 Beerli, R. R., Segal, D. J., Dreier, B. & Barbas, C. F. r. Toward controlling gene expression at will: Specific regulation of

the erbB-2yHER-2 promoter by using polydactyl zinc finger

proteins constructed from modular building blocks. *Proc Natl Acad Sci U S A.* **95**, 33 (1998).
84 Perez-Pinera, P. *et al.* Synergistic and tunable human gene activation by combinations of synthetic transcription factors. *Nat Methods* **10**, 239-242, doi:10.1038/nmeth.2361 (2013).

85 Polstein, L. R. & Gersbach, C. A. A light-inducible CRISPR-Cas9 system for control of endogenous gene activation. *Nat Chem Biol* **11**, 198-200, doi:10.1038/nchembio.1753 (2015).
86 Raposo, A. A. *et al.* Ascl1 Coordinately Regulates Gene Expression and the Chromatin Landscape during Neurogenesis. *Cell Rep* **15**, pii: S2211-1247, doi:10.1016/j.celrep.2015.02.025. (2015).
87 Weintraub, H. *et al.* Activation of muscle-specific genes in pigment, nerve, fat, liver, and fibroblast cell lines by forced expression of MyoD. *Proc Natl Acad Sci U S A* **86**, 5434-5438 (1989).
88 Tedesco, F. S., Dellavalle, A., Diaz-Manera, J., Messina, G. & Cossu, G. Repairing skeletal muscle: regenerative potential of skeletal muscle stem cells. *J Clin Invest* **120**, 11-19, doi:10.1172/JCI40373 (2010).
89 Chanda, S. *et al.* Generation of induced neuronal cells by the single reprogramming factor ASCL1. *Stem Cell Reports* **3**, 282-296, doi:10.1016/j.stemcr.2014.05.020 (2014).
90 June, C. H., O'Connor, R. S., Kawalekar, O. U., Ghassemi, S. & Milone, M. C. CAR T cell immunotherapy for human cancer. *Science* **359**, 1361-1365, doi:10.1126/science.aar6711 (2018).
91 Maude, S. L. *et al.* Tisagenlecleucel in Children and Young Adults with B-Cell Lymphoblastic Leukemia. *N Engl J Med* **378**, 439-448, doi:10.1056/NEJMoa1709866 (2018).
92 Neelapu, S. S. *et al.* Axicabtagene Ciloleucel CAR T-Cell Therapy in Refractory Large B-Cell Lymphoma. *N Engl J Med* **377**, 2531-2544, doi:10.1056/NEJMoa1707447 (2017).
93 Magee, M. S. & Snook, A. E. Challenges to chimeric antigen receptor (CAR)-T cell therapy for cancer. *Discov Med* **18**, 265-271 (2014).
94 Thistlethwaite, F. C. *et al.* The clinical efficacy of first-generation carcinoembryonic antigen (CEACAM5)-specific CAR T cells is limited by poor persistence and transient pre-conditioning-dependent respiratory toxicity. *Cancer Immunol Immunother* **66**, 1425-1436, doi:10.1007/s00262-017-2034-7 (2017).
95 Han, J. *et al.* CAR-Engineered NK Cells Targeting Wild-Type EGFR and EGFRvIII Enhance Killing of Glioblastoma and Patient-Derived Glioblastoma Stem Cells. *Sci Rep* **5**, 11483, doi:10.1038/srep11483 (2015).
96 Prapa, M. *et al.* A novel anti-GD2/4-1BB chimeric antigen receptor triggers neuroblastoma cell killing. *Oncotarget* **6**, 24884-24894, doi:10.18632/oncotarget.4670 (2015).
97 Scarfo, I. & Maus, M. V. Current approaches to increase CAR T cell potency in solid tumors: targeting the tumor microenvironment. *J Immunother Cancer* **5**, 28, doi:10.1186/s40425-017-0230-9 (2017).
98 Pule, M. A. *et al.* Virus-specific T cells engineered to coexpress tumor-specific receptors: persistence and antitumor activity in individuals with neuroblastoma. *Nat Med* **14**, 1264-1270, doi:10.1038/nm.1882 (2008).
99 D'Aloia, M. M., Zizzari, I. G., Sacchetti, B., Pierelli, L. & Alimandi, M. CAR-T cells: the long and winding road to solid tumors. *Cell Death Dis* **9**, 282, doi:10.1038/s41419-018-0278-6 (2018).

100 Craddock, J. A. *et al.* Enhanced tumor trafficking of GD2 chimeric antigen receptor T cells by expression of the chemokine receptor CCR2b. *J Immunother* **33**, 780-788, doi:10.1097/CJI.0b013e3181ee6675 (2010).
101 Ma, D. *et al.* Role of ER export signals in controlling surface potassium channel numbers. *Science* **291**, 316-319, doi:10.1126/science.291.5502.316 (2001).
102 Gradinaru, V. *et al.* Molecular and cellular approaches for diversifying and extending optogenetics. *Cell* **141**, 154-165, doi:10.1016/j.cell.2010.02.037 (2010).
103 Wen, W., Meinkoth, J. L., Tsien, R. Y. & Taylor, S. S. Identification of a signal for rapid export of proteins from the nucleus. *Cell* **82**, 463-473 (1995).
104 Wu, J. *et al.* An activating immunoreceptor complex formed by NKG2D and DAP10. *Science* **285**, 730-732 (1999).
105 Wu, C. Y., Roybal, K. T., Puchner, E. M., Onuffer, J. & Lim, W. A. Remote control of therapeutic T cells through a small molecule-gated chimeric receptor. *Science* **350**, aab4077, doi:10.1126/science.aab4077 (2015).
106 Irving, B. A., Chan, A. C. & Weiss, A. Functional characterization of a signal transducing motif present in the T cell antigen receptor zeta chain. *J Exp Med* **177**, 1093-1103 (1993).
107 Zimmerman, S. P. *et al.* Tuning the Binding Affinities and Reversion Kinetics of a Light Inducible Dimer Allows Control of Transmembrane Protein Localization. *Biochemistry* **55**, 5264-5271, doi:10.1021/acs.biochem.6b00529 (2016).
108 Testi, R., Phillips, J. H. & Lanier, L. L. T cell activation via Leu-23 (CD69). *J Immunol* **143**, 1123-1128 (1989).
109 Chen, J. *et al.* NR4A transcription factors limit CAR T cell function in solid tumours. *Nature* **567**, 530-534, doi:10.1038/s41586-019-0985-x (2019).
110 Maraskovsky, E., Chen, W. F. & Shortman, K. IL-2 and IFN-gamma are two necessary lymphokines in the development of cytolytic T cells. *J Immunol* **143**, 1210-1214 (1989).
111 Yu, N. *et al.* Near-Infrared-Light Activatable Nanoparticles for Deep-Tissue-Penetrating Wireless Optogenetics. *Adv Healthc Mater* **8**, e1801132, doi:10.1002/adhm.201801132 (2019).
112 Tan, P., He, L., Han, G. & Zhou, Y. Optogenetic Immunomodulation: Shedding Light on Antitumor Immunity. *Trends Biotechnol* **35**, 215-226, doi:10.1016/j.tibtech.2016.09.002 (2017).
113 Huang, K., Jayakumar, M. K. G. & Zhang, Y. Lutetium doping for making big core and core–shell upconversion nanoparticles. *J. Mater. Chem. C*, doi:doi:10.1039/c5tc00817d (2015).
114 Barolet, D. Light-emitting diodes (LEDs) in dermatology. *Semin Cutan Med Surg* **27**, 227-238, doi:10.1016/j.sder.2008.08.003 (2008).
115 Kansagra, A. J. *et al.* Clinical Utilization of Chimeric Antigen Receptor T Cells in B Cell Acute Lymphoblastic Leukemia: An Expert Opinion from the European Society for Blood and Marrow Transplantation and the American Society for Blood and Marrow Transplantation. *Biol Blood Marrow Transplant* **25**, e76-e85, doi:10.1016/j.bbmt.2018.12.068 (2019).
116 Dai, H., Wang, Y., Lu, X. & Han, W. Chimeric Antigen Receptors Modified T-Cells for Cancer Therapy. *J Natl Cancer Inst* **108**, doi:10.1093/jnci/djv439 (2016).

117 Lee, D. W. *et al.* T cells expressing CD19 chimeric antigen receptors for acute lymphoblastic leukaemia in children and young adults: a phase 1 dose-escalation trial. *Lancet* **385**, 517-528, doi:10.1016/S0140-6736(14)61403-3 (2015).
118 Maude, S. L. *et al.* Chimeric antigen receptor T cells for sustained remissions in leukemia. *N Engl J Med* **371**, 1507-1517, doi:10.1056/NEJMoa1407222 (2014).
119 Giavridis, T. *et al.* CAR T cell-induced cytokine release syndrome is mediated by macrophages and abated by IL-1 blockade. *Nat Med* **24**, 731-738, doi:10.1038/s41591-018-0041-7 (2018).
120 Kristiansen, K. *et al.* A highly conserved aspartic acid (Asp-155) anchors the terminal amine moiety of tryptamines and is involved in membrane targeting of the 5-HT(2A) serotonin receptor but does not participate in activation via a "salt-bridge disruption" mechanism. *J Pharmacol Exp Ther* **293**, 735-746 (2000).
121 Srinivasan, S., Vaisse, C. & Conklin, B. R. Engineering the melanocortin-4 receptor to control G(s) signaling in vivo. *Ann N Y Acad Sci* **994**, 225-232, doi:10.1111/j.1749-6632.2003.tb03184.x (2003).
122 Bruysters, M., Jongejan, A., Akdemir, A., Bakker, R. A. & Leurs, R. A G(q/11)-coupled mutant histamine H(1) receptor F435A activated solely by synthetic ligands (RASSL). *J Biol Chem* **280**, 34741-34746, doi:10.1074/jbc.M504165200 (2005).
123 Armbruster, B. N., Li, X., Pausch, M. H., Herlitze, S. & Roth, B. L. Evolving the lock to fit the key to create a family of G protein-coupled receptors potently activated by an inert ligand. *Proc Natl Acad Sci U S A* **104**, 5163-5168, doi:10.1073/pnas.0700293104 (2007).
124 Alexander, G. M. *et al.* Remote control of neuronal activity in transgenic mice expressing evolved G protein-coupled receptors. *Neuron* **63**, 27-39, doi:10.1016/j.neuron.2009.06.014 (2009).
125 Balcazar Morales, N. & Aguilar de Plata, C. Role of AKT/mTORC1 pathway in pancreatic beta-cell proliferation. *Colomb Med (Cali)* **43**, 235-243 (2012).
126 Manvich, D. F. *et al.* The DREADD agonist clozapine N-oxide (CNO) is reverse-metabolized to clozapine and produces clozapine-like interoceptive stimulus effects in rats and mice. *Sci Rep* **8**, 3840, doi:10.1038/s41598-018-22116-z (2018).
127 Chang, W. H. *et al.* Reversible metabolism of clozapine and clozapine N-oxide in schizophrenic patients. *Prog Neuropsychopharmacol Biol Psychiatry* **22**, 723-739, doi:10.1016/s0278-5846(98)00035-9 (1998).
128 Jann, M. W., Lam, Y. W. & Chang, W. H. Rapid formation of clozapine in guinea-pigs and man following clozapine-N-oxide administration. *Arch Int Pharmacodyn Ther* **328**, 243-250 (1994).
129 Raper, J. *et al.* Metabolism and Distribution of Clozapine-N-oxide: Implications for Nonhuman Primate Chemogenetics. *ACS Chem Neurosci* **8**, 1570-1576, doi:10.1021/acschemneuro.7b00079 (2017).
130 MacLaren, D. A. *et al.* Clozapine N-Oxide Administration Produces Behavioral Effects in Long-Evans Rats: Implications for Designing DREADD Experiments. *eNeuro* **3**, doi:10.1523/ENEURO.0219-16.2016 (2016).
131 Cremers, T. I., Flik, G., Hofland, C. & Stratford, R. E., Jr. Microdialysis evaluation of clozapine and N-desmethylclozapine pharmacokinetics in rat brain. *Drug Metab Dispos* **40**, 1909-1916, doi:10.1124/dmd.112.045682 (2012).

132 Li, C. H. *et al.* Prediction of brain clozapine and norclozapine concentrations in humans from a scaled pharmacokinetic model for rat brain and plasma pharmacokinetics. *J Transl Med* **12**, 203, doi:10.1186/1479-5876-12-203 (2014).
133 De Fazio, P. *et al.* Rare and very rare adverse effects of clozapine. *Neuropsychiatr Dis Treat* **11**, 1995-2003, doi:10.2147/NDT.S83989 (2015).
134 Krupp, P. & Barnes, P. Clozapine-associated agranulocytosis: risk and aetiology. *Br J Psychiatry Suppl*, 38-40 (1992).
135 Thompson, K. J. *et al.* DREADD Agonist 21 Is an Effective Agonist for Muscarinic-Based DREADDs in Vitro and in Vivo. *ACS Pharmacol Transl Sci* **1**, 61-72, doi:10.1021/acsptsci.8b00012 (2018).
136 Chen, X. *et al.* The first structure-activity relationship studies for designer receptors exclusively activated by designer drugs. *ACS Chem Neurosci* **6**, 476-484, doi:10.1021/cn500325v (2015).
137 Roth, B. L. DREADDs for Neuroscientists. *Neuron* **89**, 683-694, doi:10.1016/j.neuron.2016.01.040 (2016).
138 Weston, M. *et al.* Olanzapine: A potent agonist at the hM4D(Gi) DREADD amenable to clinical translation of chemogenetics. *Sci Adv* **5**, eaaw1567, doi:10.1126/sciadv.aaw1567 (2019).
139 Natarajan, J., Baskaran, M., Humtsoe, L. C., Vadivelan, R. & Justin, A. Enhanced brain targeting efficacy of Olanzapine through solid lipid nanoparticles. *Artif Cells Nanomed Biotechnol* **45**, 364-371, doi:10.3109/21691401.2016.1160402 (2017).
140 Huang, M. *et al.* A randomized, 13-week study assessing the efficacy and metabolic effects of paliperidone palmitate injection and olanzapine in first-episode schizophrenia patients. *Prog Neuropsychopharmacol Biol Psychiatry* **81**, 122-130, doi:10.1016/j.pnpbp.2017.10.021 (2018).
141 Wang, J. S. *et al.* Olanzapine penetration into brain is greater in transgenic Abcb1a P-glycoprotein-deficient mice than FVB1 (wild-type) animals. *Neuropsychopharmacology* **29**, 551-557, doi:10.1038/sj.npp.1300372 (2004).
142 Jing, M. *et al.* A genetically encoded fluorescent acetylcholine indicator for in vitro and in vivo studies. *Nat Biotechnol* **36**, 726-737, doi:10.1038/nbt.4184 (2018).
143 Odaka, H., Arai, S., Inoue, T. & Kitaguchi, T. Genetically-encoded yellow fluorescent cAMP indicator with an expanded dynamic range for dual-color imaging. *PLoS One* **9**, e100252, doi:10.1371/journal.pone.0100252 (2014).
144 Brudvik, K. W. & Tasken, K. Modulation of T cell immune functions by the prostaglandin E(2) - cAMP pathway in chronic inflammatory states. *Br J Pharmacol* **166**, 411-419, doi:10.1111/j.1476-5381.2011.01800.x (2012).
145 Ahn, E. *et al.* Role of PD-1 during effector CD8 T cell differentiation. *Proc Natl Acad Sci U S A* **115**, 4749-4754, doi:10.1073/pnas.1718217115 (2018).
146 Simon, S. & Labarriere, N. PD-1 expression on tumor-specific T cells: Friend or foe for immunotherapy? *Oncoimmunology* **7**, e1364828, doi:10.1080/2162402X.2017.1364828 (2017).
147 Liu, X. *et al.* Genome-wide analysis identifies NR4A1 as a key mediator of T cell dysfunction. *Nature* **567**, 525-529, doi:10.1038/s41586-019-0979-8 (2019).
148 Ashouri, J. F. & Weiss, A. Endogenous Nur77 Is a Specific Indicator of Antigen Receptor Signaling in Human T and B Cells. *J Immunol* **198**, 657-668, doi:10.4049/jimmunol.1601301 (2017).

149 Moran, A. E. *et al.* T cell receptor signal strength in Treg and iNKT cell development demonstrated by a novel fluorescent reporter mouse. *J Exp Med* **208**, 1279-1289, doi:10.1084/jem.20110308 (2011).
150 Zikherman, J., Parameswaran, R. & Weiss, A. Endogenous antigen tunes the responsiveness of naive B cells but not T cells. *Nature* **489**, 160-164, doi:10.1038/nature11311 (2012).
151 Cheng, C., Huang, Y. L. & Yang, S. T. A novel feeding strategy for enhanced plasmid stability and protein production in recombinant yeast fedbatch fermentation. *Biotechnol Bioeng* **56**, 23-31, doi:10.1002/(SICI)1097-0290(19971005)56:1<23::AID-BIT3>3.0.CO;2-X (1997).
152 Zayner, J. P. & Sosnick, T. R. Factors that control the chemistry of the LOV domain photocycle. *PLoS One* **9**, e87074, doi:10.1371/journal.pone.0087074 (2014).
153 Taslimi, A. *et al.* Optimized second-generation CRY2-CIB dimerizers and photoactivatable Cre recombinase. *Nat Chem Biol* **12**, 425-430, doi:10.1038/nchembio.2063 (2016).